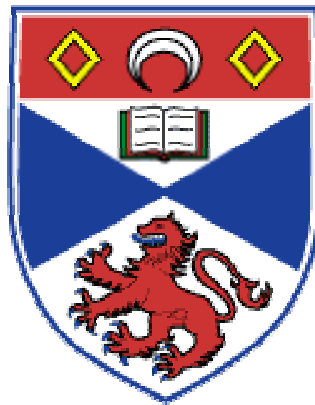


The Fabrication and Lithography of Conjugated Polymer Distributed Feedback Lasers and Development of their Applications.



Scott Richardson.

July 2007

A thesis submitted to the School of Physics and Astronomy at the University of St.
Andrews, for the degree of Doctor of Philosophy

Abstract

This thesis presents a study of lasing properties and optical amplification in semiconducting conjugated polymers and dendrimers. Configured as surface-emitting distributed feedback lasers, the effect of incorporating wavelength-scale microstructure on the output of the devices is examined along with the ability to create such structures using simplified fabrication processes such as soft lithography.

Conjugated materials have received a great deal of interest due to their broad spectral absorption, emission, ability to exhibit gain and ease of processing from solution. As a result, they show great potential for a variety of applications such as photovoltaics, displays, amplifiers and lasers. To date however, there has only been one demonstration of a polymer optical amplifier. A broadband, solution based polymer amplifier is presented where the gain overlaps with the transmission window of polymer optical fibres. The effect of transitions that reduce the availability of gain in conjugated polymers is also examined by studying saturation of absorption in thin films.

Producing wavelength scale microstructure is traditionally a slow, expensive technique. Here, solvent assisted micromoulding is used to pattern polymer films in less than two minutes. The effect of the variations in the pattern transfer on the laser characteristics is examined. The micromoulding technique is then applied to fabricating novel device types such as circular gratings and flexible plastic lasers. Encapsulation of the micromoulded laser is then shown to improve the lifetime of the device by over three orders of magnitude. The degradation effects witnessed during this extended operation are characterised quantitatively, an area of study where little data exists in the literature.

A novel class of branched dendrimer materials whose properties can be independently tuned due to their modular architecture are configured as blue-emitting distributed feedback lasers. The ability to tune the emission wavelength by varying the film thickness is demonstrated. By changing the chemical groups contained within the molecule, further tuning of the emission can be obtained along with the demonstration of a highly efficient blue-emitting dendrimer laser. Chemosensing using dendrimer lasers is presented by demonstrating the incredibly sensitive response of the laser device to trace vapours of nitro-benzene compounds. The future application of which could be highly beneficial in the detection of explosives.

Declarations.

I, Scott Richardson, hereby certify that this thesis, which is approximately 37000 words in length, has been written by me, that it is the record of work carried out by me and that it has not been submitted in any previous application for a higher degree.

Scott Richardson

31/7/07

I was admitted as a research student in September 2003 and as a candidate for the degree of Doctor of Philosophy in September 2003; the higher study for which this is a record was carried out in the University of St. Andrews between 2003 and 2006.

Scott Richardson

31/7/07

I hereby certify that the candidate has fulfilled the conditions of the Resolution and Regulations appropriate for the degree of Doctor of Philosophy in the University of St. Andrews and that the candidate is qualified to submit this thesis in application for that degree.

Prof. Ifor D. W. Samuel

31/7/07

Dr. Graham A. Turnbull

31/7/07

Copyright Declaration

In submitting this thesis to the University of St. Andrews, I understand that I am giving permission for it to be made available for use in accordance with the regulations of the University Library for the time being in force, subject to any copyright vested in the work not being affect thereby. I also understand that the title and abstract will be published, and that a copy of the work may be made and supplied to any bona fide library for a research worker, that my thesis will be electronically accessible for personal or research use, and that the library has the right to migrate my thesis into new electronic forms as required to ensure continued access to the thesis. I have obtained any third-party copyright permissions that may be required to allow such access and migration.

Scott Richardson

31/7/07

Acknowledgements

There are a great many people who deserve recognition for the support and help provided throughout my time as a research student. While during the many occasions the frontiers of research hit unforeseen hiccups, brick walls and in some cases, the lab floor, it was those around me who I could turn to for guidance and advice. Without this input, the work contained in the thesis you now read would have been far less pleasurable to conduct.

For my introduction to soft lithography and the fabrication / characterising of polymer lasers when starting out, my thanks to Dr. Justin Lawrence and Dr. Alison Carleton. A great deal of thanks go to the gallic charm of Dr. Olivier Gaudin for his invaluable help and discussions over the workings of ellipsometry and also to Dr. Jean-Charles Ribierre for his knowledge of dendrimer materials. I would also like to thank Dr. Andrew McNeil for my crash course in encapsulated diodes which (eventually) led to the fabrication of successful laser devices.

For supplying the silica grating structures vital to much of this work, my thanks to Prof. Bill Barnes and all those at the University of Exeter who performed the fabrication and also to Dr. Paul Burn, Dr. Homar Barcena and the rest of the Oxford group who synthesised the dendrimer materials.

In no particular order, Stuart, Paul S, Liz, Sarah, Georgis, Andreas, Arvydas, Dimi from our group, who shared their wisdom with me at some point whether I wanted it or not and also to Mr. Motivator, Paul M, who made it his daily habit of asking “Is it finished yet?” This particular list would not be complete without acknowledging the friendship of Andy, Goose, Neil and Spurr, ever on hand for discussions about home-boys and Jack Bauer and for helping achieve the once-thought impossible task of winning 5 in a row at the Cellar music pub quiz.

There are two final sets of acknowledgements, which need to be made. It is a pleasure to offer my thanks and gratitude to my supervisors, Ifor and Graham, whose constant input helped make this thesis possible. Last, but in no ways least, my thanks to my family who, despite my reservations about the location of my desk in recent months (and the pressing desire need to avoid falling through the attic ceiling) have supported every step I have taken in this journey and for that, I offer my love and my thanks.

CHAPTER 1: INTRODUCTION	4
1.1 References	9
CHAPTER 2: THEORETICAL BACKGROUND	12
2.1 Photophysics of Conjugated Polymers	12
2.1.1 Conjugation and origins of semiconductivity in polymers	12
2.1.2 Electronic configuration	16
2.1.3 Absorption and Emission	18
2.1.4 Gain in conjugated polymer systems	22
2.2 Polymer Lasers	27
2.2.1 Waveguiding	27
2.2.2 Feedback Structures	31
2.2.3 Distributed Feedback Lasers	34
2.3 Summary	37
2.4 References	38
CHAPTER 3: EXPERIMENTAL METHODS	42
3.1 Introduction	42
3.2 Material Preparation	42
3.2.1 Soluble polymers and dendrimers	43
3.2.2 Small molecular compounds	44
3.3 Photophysical Characterisation	45
3.3.1 Absorption measurements	45
3.3.2 Fluorescence measurements	46
3.3.3 Photoluminescence quantum yield	46
3.4 Device Preparation	47
3.4.1 Substrate preparation	48
3.4.2 Active layer preparation	48
3.4.3 Preparation of pattern transfer elements	49
3.5 Device Characterisation	51
3.5.1 Atomic Force Microscopy	51
3.5.2 Ellipsometry measurements	54
3.5.3 Laser characterisation	56
3.6 References	59

CHAPTER 4: SOFT LITHOGRAPHY FOR POLYMER LASERS	61
4.1 Introduction	61
4.2 Review of lithographic techniques	62
4.2.1 Conventional Lithography	62
4.2.2 Soft Lithography	65
4.2.3 Solvent Assisted Micromoulding	70
4.3 Effect of grating depth on threshold for polymer lasers	72
4.3.1 Experimental	72
4.3.2 Results	73
4.4 Application of soft lithography for novel device fabrication	84
4.4.1 Circular Distributed Feedback Lasers	84
4.4.2 Flexible Polymer Lasers	90
4.5 Summary	97
4.6 References	99
 CHAPTER 5: ENCAPSULATED POLYMER LASERS	 103
5.1 Introduction	103
5.2 Encapsulation of organic devices	104
5.2.1 Encapsulated organic light emitting diodes	104
5.2.2 Encapsulated lasers	105
5.2.3 Experimental	108
5.2.4 Results	110
5.3 Photodegradation effects in encapsulated lasers	120
5.3.1 Experimental	121
5.3.2 Results	122
5.4 Towards improved device performance	129
5.5 Summary	132
5.6 References	134
 CHAPTER 6: GAIN AND ABSORPTION SATURATION IN CONJUGATED POLYMERS.	 137
6.1 Introduction	137
6.2 Solution based optical amplifier	139
6.2.1 Experimental	139

6.2.2.	Results	142
6.3	Saturated absorption in thin films of MEH-PPV	147
6.3.1	Experimental	147
6.3.2	Results	148
6.4	Summary	156
6.5	References	158
CHAPTER 7:	DENDRIMER LASERS	160
7.1	Introduction	160
7.2	The dendrimer concept	162
7.3	Materials for dendrimer lasers	164
7.3.1	Experimental	166
7.3.2	Results	168
7.4	Explosives detection through dendrimer lasers	177
7.4.1	Experimental	178
7.4.2	Results	179
7.5	Soft lithography of dendrimer materials	188
7.5.1	Experimental	188
7.5.2	Results	189
7.6	Summary	195
7.7	References	197
CHAPTER 8:	CONCLUSIONS	202
APPENDIX A:	PUBLICATIONS ARISING FROM THIS THESIS	206

Chapter 1: Introduction

Given all the natural resources that are available for humanity to exploit, it is a group of man-made materials that has created one of the most profound impacts to our existence. From clothing fibres to car components and the buttons of the keyboard used to type these words, plastics pervade our everyday lifestyle to the point that it is hard to imagine how different or difficult everyday tasks would be without them. They are synthesised consumables that provide us with a range of properties, styles and colours to suit our every need.

Never content to rest on his laurels, man's curiosity and desire to understand the world around him has led to other revolutionary breakthroughs. The advent of inorganic semiconductors such as silicon and germanium gives us the building blocks to fabricate the transistors and diodes that are responsible for the digital age and provides us with items essential to our modern lifestyle such as computers. For a time, these inorganic materials were the sole providers of semiconducting properties until a fascinating class of organic molecules were synthesised by Shirakawa *et al.* [1]. The discovery of these polymers and their semiconducting properties was of such importance, that the Nobel Prize for Chemistry was awarded for this work in 2000. What made the polymers special was the arrangement of its chemical bonds or conjugation, the same property that grants biological systems the power to generate light in the deepest oceans or to harvest solar energy for fuel.

Over the thirty years that have followed, the light-emitting ability of conjugated polymers [2-3] has enabled them to find roles in widespread applications. Organic

transistors [4] and light-emitting diodes [3,5] have been developed, following in the footsteps of their inorganic counterparts. Short-haul telecommunications are increasingly making use of polymer optical fibres [6]. A recent breakthrough is the exploitation of the sensory abilities of polymer materials, such as the capability to detect explosives [7].

In addition to the diverse range of applications mentioned above, one continually vibrant topic of conjugated polymer research concerns the amplification of light to form a laser. The operation of the first laser (using ruby as a gain medium) was demonstrated by Maiman in 1960 [8]. Five decades later, we find lasers in our compact-disc players and supermarket checkouts, taking for granted a phenomenon that opened new insights within the confines of physics and chemistry.

Organic materials were quickly exploited as laser materials shortly after this initial report. One example was the solid-state laser using anthracene crystals in 1974 [9]. Conjugated polymers had to wait a little longer to receive the same treatment. Daniel Moses reported stimulated emission from a polymer solution in 1992 [10]. Solid-state versions arrived a few years later [11-13] and have been a hot topic ever since, featuring in a number of review articles [14-16]. It is the further development of laser devices using this fascinating family of conjugated materials that forms the basis of this work.

The thesis begins with an examination of the origins of semiconductor behaviour in conjugated polymers. The absorption and emission processes that result from the electronic configuration and are responsible for the broad gain throughout the visible spectrum [17-20] are explained.

Wavelength scale microstructure can have a dramatic effect on the output of a device, allowing manipulation and control over the light emission. Examples of this include increasing the efficiency of an organic light-emitting diode [21] and providing the feedback mechanism for polymer lasers [22]. Chapter 3 outlines the experimental procedures used to fabricate devices with this technology in addition to the major techniques required to characterise both the physical and optical properties of the samples.

The theme of nanometer scale structure continues with the experimental work, which begins in chapter 4. Creating such small patterns is often an expensive, complicated procedure requiring dedicated equipment such as photolithography or electron beam lithography. A key attribute of conjugated polymers, which makes them attractive materials to work with, is the ease of which they can be processed from solution. Thus, a simple mechanism for applying a pattern or grating is highly desirable and is precisely what a range of techniques collectively termed ‘soft lithography’ [23] provides. Chapter 4 begins with a review of soft lithographic methods. It continues with a demonstration of how one can vary the threshold value by controlling the grating depth, including a low threshold device equivalent to conjugated polymer lasers formed using conventional lithography [24]. To conclude the section, some applications of using soft lithography to directly pattern the polymer surface with novel circular gratings and the fabrication of flexible lasers are presented.

The drive towards electrical pumping (which has currently not been demonstrated, devices being excited optically) has seen a great deal of research into the lowering of the threshold for polymer lasers and has enabled breakthroughs such as diode pumping of conjugated polymers [25-27]. The laser threshold of microstructured

polymer films is the primary focus of chapter 4. While a great deal of information regarding the power characteristics has been reported, there is comparatively little quantitative data on the operational lifetime of such devices. A limitation of conjugated polymer materials is that they undergo degradation as a result of being illuminated in combination with contact to oxygen and water, constraining their potential for operation in ambient conditions. Chapter 5 deals with encapsulating microstructured polymer lasers similar to those introduced in chapter 4, with suitable materials to protect them from the outside elements and demonstrates a dramatic improvement in performance. The latter half of the chapter outlines an explanation for photodegradation effects in the polymer material caused when an excitation source is incident on its surface for an extended period.

While intense optical pumping gives rise to degradation in encapsulated lasers, chapter 6 examines alternative outcomes of focussing an excitation beam onto a conjugated polymer. The initial section of the chapter reports on the fabrication and testing of a solution based polymer amplifier. While plastic fibres have many advantages over those based on silica such as durability and flexibility, their main drawback is high optical attenuation. Thus, development of compact amplifier sources is extremely important for the next generation of short-haul networks with a previous report [28] demonstrating the potential of these devices. The remainder of chapter 6 discusses the effects of saturated absorption in thin films of a conjugated polymer comparing the experimental data to a model simulation taking into account molecular interactions.

One can typically divide organic semiconductors into three main classes of material: small organic molecules, conjugated polymers and a new class of branched

materials named dendrimers. Dendrimers possess many advantages over their polymer counterparts. A central core is linked to surface molecules through connecting groups named dendrons. This modular approach to the synthesis allows the independent tuning of the optical properties (regulated by the core) and the processing properties (associated with the surface groups) [29-31]. While a great many conjugated polymers operate in the red part of the visible spectrum (such as those used throughout the earlier chapters), there are comparatively few that form devices in the blue. One such material is polyfluorene (PFO) which has successfully been used to fabricate laser devices [32]. In chapter 7, a number of novel dendrimer materials are fabricated as laser devices resulting in the demonstration of an efficient, blue-emitting device. The results from this study are further explored in the second half of the chapter where an application for dendrimer lasers is presented with the detection of explosive vapour. Electron deficient nitro groups present in the nitrobenzene family of materials bind to the electron rich surface of the dendrimer, quenching the output emission. The final part of this thesis reports on the enhanced sensitivity of the dendrimer in a lasing configuration when compared to luminescence from the device. A summary of the key points and results are presented in the conclusions in chapter 8.

1.1 References

- [1] H. Shirakawa, E.J. Louis, A.G. Macdiarmid, C.K. Chang and A.J. Heeger, *Journal of the American Chemical Society: Chemical Communications*, **16**, 578-580, (1977).
- [2] R.H. Partridge, *Polymer*, **24**, 755 (1983).
- [3] J.H. Burroughes, D.D.C. Bradley, A.R. Brown, R.N. Marks, K. Mackay, R.H. Friend, P.L. Burn and A.B. Holmes, *Nature*, **347**, 539 (1990).
- [4] A. Tsumura, H. Koezuka and T. Ando, *Applied Physics Letters*, **49**, 1210 (1986).
- [5] C.W. Tang and S.A. Vanslyke, *Applied Physics Letters*, **51**, 913 (1987).
- [6] J. Zubia and J. Arrue, *Optical Fiber Technology*, **7**, 101 (2001).
- [7] A. Rose, Z.Zhu, C.F. Madigan, T.M. Swager and V. Bulovic, *Nature*, **434**, 876 (2005).
- [8] T.H. Maiman, *Nature*, **187**, 493 (1960).
- [9] O.S. Avanesjan, V.A. Benderskii, V.K. Brikenstein, V.L. Broude, L.I. Korshunov, G.A. Lavrushko and I.I. Tartakovskii, *Molecular Crystals and Liquid Crystals*, **29**, 165 (1974).
- [10] D. Moses, *Applied Physics Letters*, **60**, 3215 (1992).
- [11] N. Tessler, G.J. Denton and R.H. Friend, *Nature*, **382**, 695 (1996).
- [12] F. Hide, M.A. Diaz-Garcia, B.J. Schwartz, M.R. Andersson, Q.B. Pei and A.J. Heeger, *Science*, **273**, 1833 (1996).
- [13] W. Holzer, A. Penzkofer, S.H. Gong, A. Bleyer and D.D.C. Bradley, *Advanced Materials*, **8**, 974 (1996).

- [14] N. Tessler, *Advanced Materials*, **11**, 363 (1999).
- [15] M.D. McGehee and A.J. Heeger, *Advanced Materials*, **12**, 1655 (2000).
- [16] I.D.W. Samuel and G.A. Turnbull, *Chemical Reviews*, **107**, 1272 (2007).
- [17] M. Yan, L.J. Rothberg, F. Papadimitrakopoulos, M.E. Galvin and T.M. Miller, *Physical Review Letters*, **72**, 1104 (1994).
- [18] B.J. Schwartz, F. Hide, M.R. Andersson and A.J. Heeger, *Chemical Physics Letters*, **265**, 327 (1997).
- [19] G.J. Denton, N. Tessler, N.T. Harrison and R.H. Friend, *Physical Review Letters*, **78**, 733 (1997).
- [20] A.K. Sheridan, G.A. Turnbull, A.N. Safanov and I.D.W. Samuel, *Physical Review B*, **62**, 929 (2000).
- [21] J.M. Lupton, B.J. Matterson, I.D.W. Samuel, M.J. Jory and W.L. Barnes, *Applied Physics Letters*, **77**, 3340 (2000).
- [22] H. Kogelnik and C.V. Shank, *Applied Physics Letters*, **18**, 152 (1971).
- [23] Y. Xia and G.M. Whitesides, *Angew. Chem. Int. Ed.*, **37**, 550 (1998).
- [24] G.A. Turnbull, P. Andrew, W.L. Barnes and I.D.W. Samuel, *Applied Physics Letters*, **82**, 313 (2003).
- [25] T. Riedl, T. Rabe, H.H. Johannes, W. Kowalsky, J. Wang, T. Weimann, P. Hinze, B. Nehls, T. Farrell and U. Scherf, *Applied Physics Letters*, **88**, (2006).
- [26] A.E. Vasdekis, G. Tsiminis, J.-C. Ribierre, L. O’Faolain, T.F. Krauss, G.A. Turnbull and I.D.W. Samuel, *Optics Express*, **14** (2006).
- [27] C. Karnutsch, V. Haug, C. Gaertner, U. Lemmer, T. Farrell, B. Nehls, U. Scherf, J. Wang, T. Weimann, G. Heliotis, C. Pflumm, J.C. deMello and D.D.C. Bradley, Conference on Lasers and Optoelectronics 2006, Long Beach, p CFJ3 (2006).

- [28] J.R. Lawrence, G.A. Turnbull and I.D.W. Samuel, *Applied Physics Letters*, **80**, 3036 (2002).
- [29] M. Halim, J.N.G. Pillow, I.D.W. Samuel and P.L. Burn, *Synthetic Metals*, **102**, 922 (1999).
- [30] M. Halim, I.D.W. Samuel, J.N.G. Pillow and P.L. Burn, *Synthetic Metals*, **102**, 1113 (1999).
- [31] M. Halim, J.N.G. Pillow, I.D.W. Samuel and P.L. Burn, *Advanced Materials*, **11**, 371 (1999).
- [32] G. Heliotis, R.D. Xia, G.A. Turnbull, P. Andrew, W.L. Barnes, I.D.W. Samuel and D.D.C. Bradley, *Advanced Functional Materials*, **14**, 91 (2004).

Chapter 2: Theoretical Background

2.1 Photophysics of Conjugated Polymers

The essential building block for organic molecules is carbon, which exists in the form of several allotropes. These include graphite, diamond, the fullerenes, carbon nanotubes and graphene. Carbon also has the ability to form long-chain molecules that consist of anywhere between several and several thousand repeat units. The study of this fascinating class of materials in particular, forms the basis of the thesis presented here.

This chapter will discuss the role bonding between carbon atoms has on the electronic and photonic properties of an organic semiconducting material. The origins of absorption and emission and the inherent amplification of light or gain that many organic polymers provide will also be presented. Finally, this section will consider waveguiding in these materials and the impact that microstructure has on a polymer film, with particular application to the formation of feedback structures and polymer lasers.

2.1.1 Conjugation and origins of semiconductivity in polymers

Ground state carbon atoms have the electronic configuration of $1s^2 2s^2 2p^2$. In a chemical system involving more than one carbon atom, the atoms may form either a single, double or triple bond with each other. It is energetically most favourable in the case where double bonds are formed, for the unpaired, outermost p electron orbitals to

mix with the 2s orbital. This creates a hybridised combination of three equivalent sp^2 orbitals that lie in a plane at 120° to each other. This is shown in figure 2.1 below.

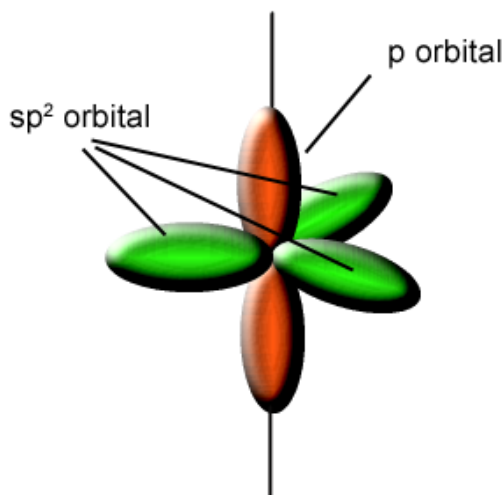


Figure 2.1: The hybridisation of s and p orbitals in carbon to form three sp^2 hybrid orbitals.

The mixing of these orbitals or Linear Combination of Atomic Orbitals (LCAO) into the sp^2 hybrid states allows overlapping of the wavefunctions when one carbon atom is brought into close proximity with a second. The sharing of the electrons between atoms is termed a covalent σ -bond and binds the carbon atoms in place. The p_z orbital, normal to the plane, remains un-hybridised. When two atoms are brought close enough to each other, this p_z orbital can also interact forming a π -bond. Whereas the σ -bonds are fairly localised to the atoms, the π -bonds are less so. This allows for some movement of the electrons, contributing to the conductivity of the molecule. As more carbon atoms are added to the chain, one witnesses the formation of alternating single and double bonds, or conjugation of the molecule.

The simplest molecule containing a double bond is ethene and is shown below in figure 2.2. The lower panel of the figure contains the structure of polyacetylene, which was the first semiconducting polymer synthesised by Shirakawa [1] almost thirty years ago. Polyacetylene has a much longer chain than ethene and demonstrates the conjugation along the polymer backbone.

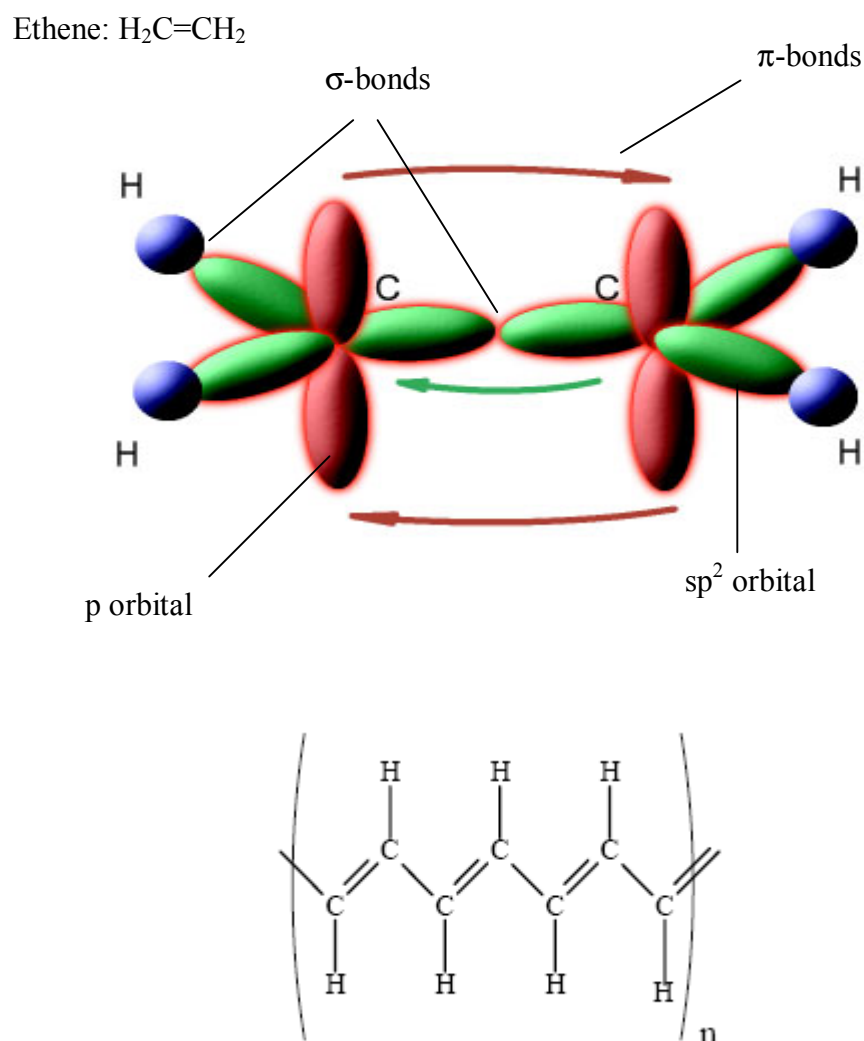


Figure 2.2: The σ and π bonding in ethene (top) and the chemical structure of polyacetylene (bottom). Structure of polyacetylene taken from [2]

The overlapping of the π -bonds gives rise to a delocalisation of the electrons along the polymer chain. There is one π -electron per carbon atom which could potentially lead to metallic behaviour (through a half filled band). Energetically however, it is preferable to form the alternating single and double bond structure. This is known as the Peierls' distortion [3] and leads to variations in the single and double bond length. The distance over which delocalisation can occur (the conjugation length), is limited by factors such as conformational issues like twists or kinks in the chain in addition to any impurities along the backbone [4-7]. This distance is much shorter than the total length of the polymer chain, which can consist of thousands of repeat units.

When many carbon atoms are present in the structure, one may liken the energy levels in conjugated polymers to their inorganic counterparts. If we take 1,3-butadiene as a simple case, the four electrons present in the π -bonds allow splitting into four energy levels. Figure 2.3 below shows how the energies of the π orbitals compare to the 2p orbital. These energies can be calculated using Hückel theory [8].

The lowest two orbitals (1π and 2π) are fully occupied in the ground state and contribute mainly to the bonding character of the system. The 2π orbital is termed the highest occupied molecular orbit (HOMO). The first unoccupied orbital ($3\pi^*$) is designated the lowest unoccupied molecular orbit (LUMO). In the case of a polymer, the number of conjugated bonds is much larger, as is the number of π orbitals. The bonding and anti-bonding states form two quasi-continuous energy levels, separated by an energy gap. This band like picture of the energy structure leads to the analogy of the HOMO being thought of as the top of the valence band while the LUMO is the bottom of the conduction band [9].

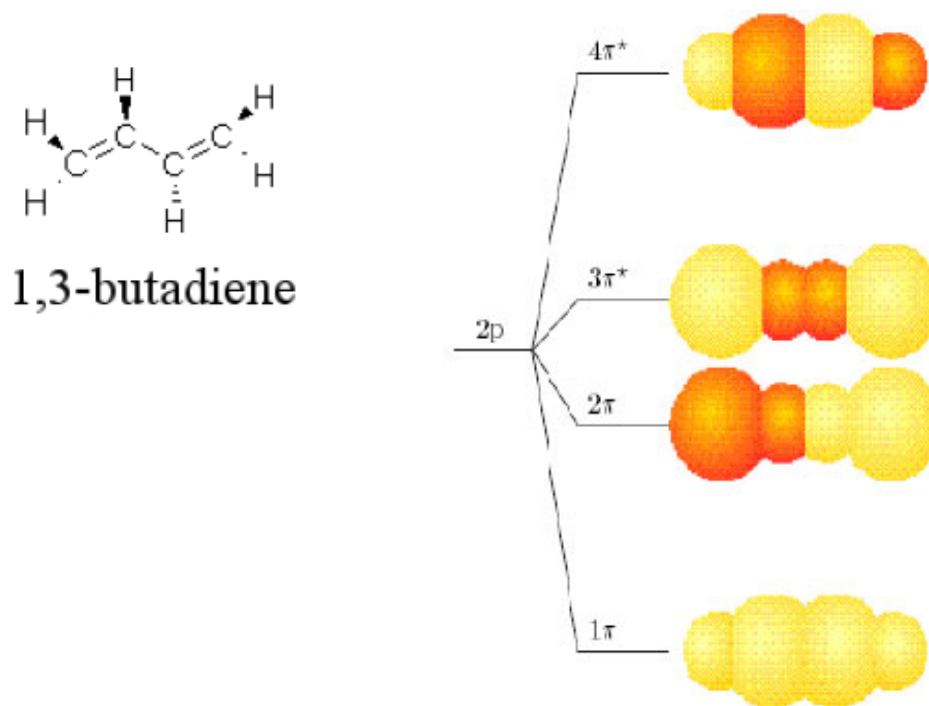


Figure 2.3: The energy levels of the π orbitals in 1,3-butadiene and their comparison to the 2p orbital (taken from [8]). The lower two orbitals are filled, each accommodating 2 of the 4 free electrons. The colour of the orbital represents the bonding and anti-bonding character for each of the states.

2.1.2 Electronic configuration

A number of models have been developed to describe the band-like structure in conjugated polymers and have met with varying degrees of success. Application of the tight binding model with the inclusion of electron-phonon interactions resulted in the Su-Schrieffer-Heeger (SSH) model [10]. The model predicts the formation of bands in ground state polymers such as *trans*-polyacetylene but does not take into account electron-electron interactions. This is usually an important effect to take into consideration due to the electrons being confined to single polymer chains. Further

improvements to the SSH model were introduced by Fesser, Bishop and Campbell [11] allowing for interstate crossing between the singlet and triplet states.

In contrast to this, an alternative approach involving excitonic interactions has been applied with a much greater degree of accomplishment. Instead of free or weakly bound electron-hole pairs being created (as in crystalline inorganic compounds), electrons and holes are bound by a mutual Colombic attraction that results in a characteristic exciton binding energy [12]. These excitons are located either on a single chain (intrachain) or shared between neighbouring chains (interchain). For the single chain case, the exciton is then further delocalised along the conjugation length of one of the segments. It is these units that perform the energy transport and are responsible for absorption and emission in the molecule. Migration of the excitons along the chain between segments is possible due to the strength of the binding (lying between tightly bound Frenkel [13] and weakly bound Wannier [14] excitons) and it is the existence of these particles that has a noticeable effect on the optical properties of the material.

When a charge is introduced to the system, a defect or polaron is created and can be thought of as the charge and its associated lattice distortion. This defect converts the stable aromatic state of the molecule to a quinoid state. To restore stability, the molecule can either break the chain at the defect or introduce a second defect of opposite charge to the original polaron. These charges attract and may jump to each other, leaving behind further charges along the chain. In this way, current may flow along the length of a conjugated polymer.

2.1.3 Absorption and Emission

When a radiation field interacts with an atom or molecule, it adds to the overall force acting on the component charges. This causes them to move creating an electric polarisation. The effect of applying an electric field (in the x direction) and the resulting time-dependent potential energy acquired by the electron can be solved by applying the time-dependent Schrödinger equation. The resulting wavefunction is a superposition of the ground state and excited state (where the ground state is modified by the addition of a fraction of the excited state oscillating at the frequency of the applied electric field) and gives the electric polarisation at any time. Values derived from the resulting energy eigenstates for the coupled system can be attributed to atomic transitions from the ground state to the excited state (absorption) or vice versa (emission).

Electronic transitions are commonly represented by way of configuration coordinate diagrams such as in figure 2.4. The plot displays molecular potential energy (y -axis) versus the molecular co-ordinate (x -axis) and depicts the ground state wavefunction along with the first excited state and their associated vibronic levels. Excitations occur from the lowest vibronic level in the ground state (S_0) with the strongest transitions occurring from the equilibrium position. A displacement along the x -axis between ground state and excited state represents a relative shift in the equilibrium position between the levels and is related to electron-phonon coupling. Transitions adhering to this form of coupling are drawn on the diagram with non-vertical lines.

Electronic transitions usually take place on timescales in the 10^{-15} s regime, much faster than typical timescales for the nuclei to respond (10^{-13} s). As a result, there

is little time for the nuclei to re-arrange themselves spatially. Thus, these transitions are shown as vertical lines according to the Franck-Condon principle [15].

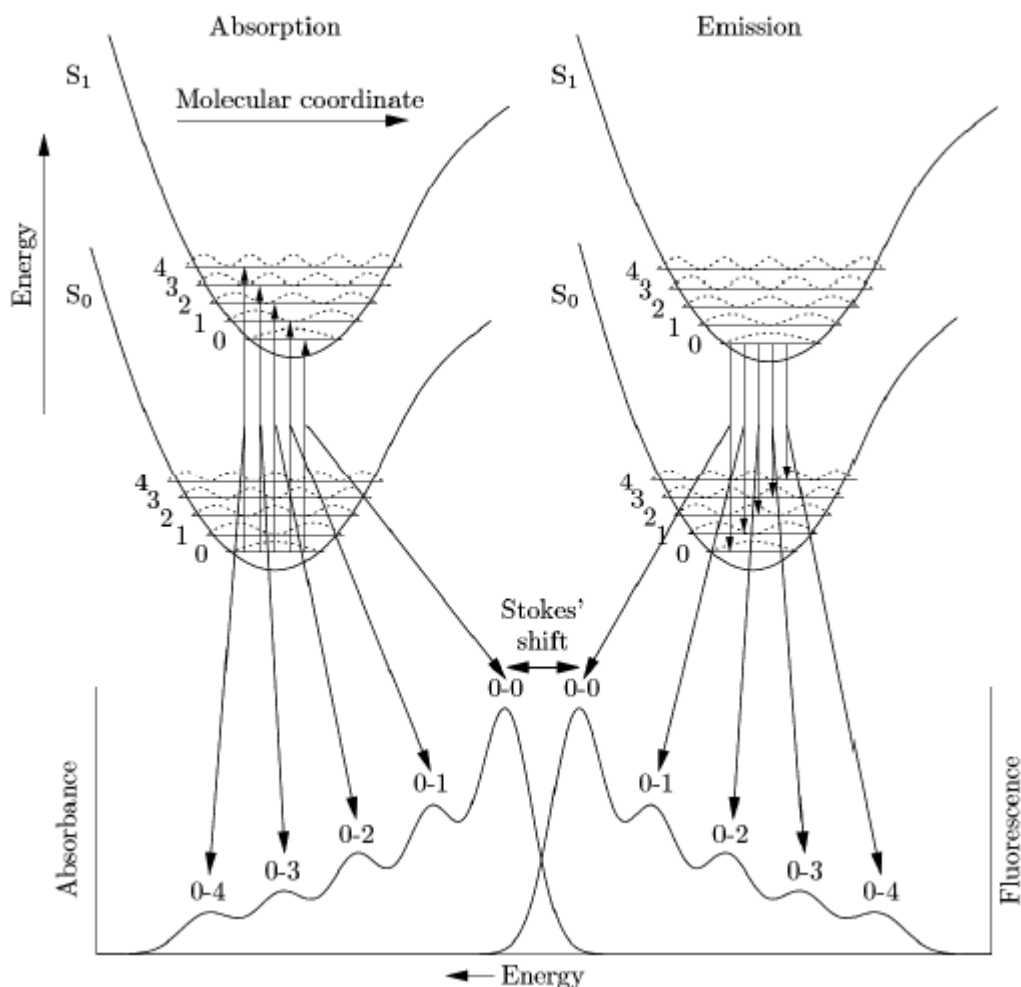


Figure 2.4: An example absorption and emission spectrum shown in the form of a Jablonski diagram. Clearly visible is the Stokes shift and also the vibronic structure, which correspond to transfers between the various energy levels. Taken from [16].

On the right hand side of figure 2.4, the energy levels involved in the emission of light are shown and follow similar principles to those of the absorption. In the basic case, the luminescence spectrum is a mirror image of the absorption spectrum. For a given material, incoming photons excite electrons from the S_0 state to the excited state S_1 .

There is then a fast, non-radiative relaxation, populating the 0th vibronic level. Finally, radiative decay processes occur from the 0th vibronic level in S₁ back to the ground state S₀. The 0-0 vibronic peak in the emission spectrum is shifted from the corresponding peak in the absorption spectrum by an amount known as the Stokes shift. The reddening of the emission is due to a geometry change in the polymer resulting in a photon being emitted with lower energy. The above description would give a mirror-image absorption and emission and this is seen in many dye molecules. However, in conjugated polymers the absorption spectrum is much broader than the emission.

For conjugated polymers, while a Stokes shift is evident in many molecules, there is general movement away from the symmetry in the absorption and emission spectra, a result of exciton migration along the chains (which is described below). For the commonly used polymer, poly(2-methoxy-5-(2'-ethylhexyloxy)-1,4-phenylene vinylene) (MEH-PPV, the chemical structure for which, can be found below in figure 2.5), one can explain this behaviour through the disordered nature of the polymer chains [12] reducing the conjugation length into short segments. Inhomogeneous broadening from these shortened segments gives rise to a broad, featureless absorption spectrum.

Emission from the polymer is not broadened in the same way due to exciton migration along the chains [17-19], which can be seen as a red-shift of fluorescence with time. As they move away from their creation site, they become trapped on long, lower energy segments. This trapping is due to surrounding, shorter chain lengths having higher energies [20,21]. When the excitons finally decay, the emission is therefore primarily from lower energy sites resulting in a narrower spectrum that displays more vibronic structure than in the absorption. This is demonstrated in MEH-PPV below, in figure 2.6.

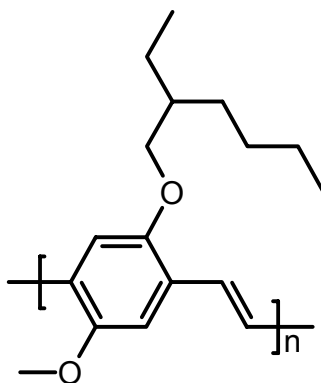


Figure 2.5: The chemical structure of MEH-PPV.

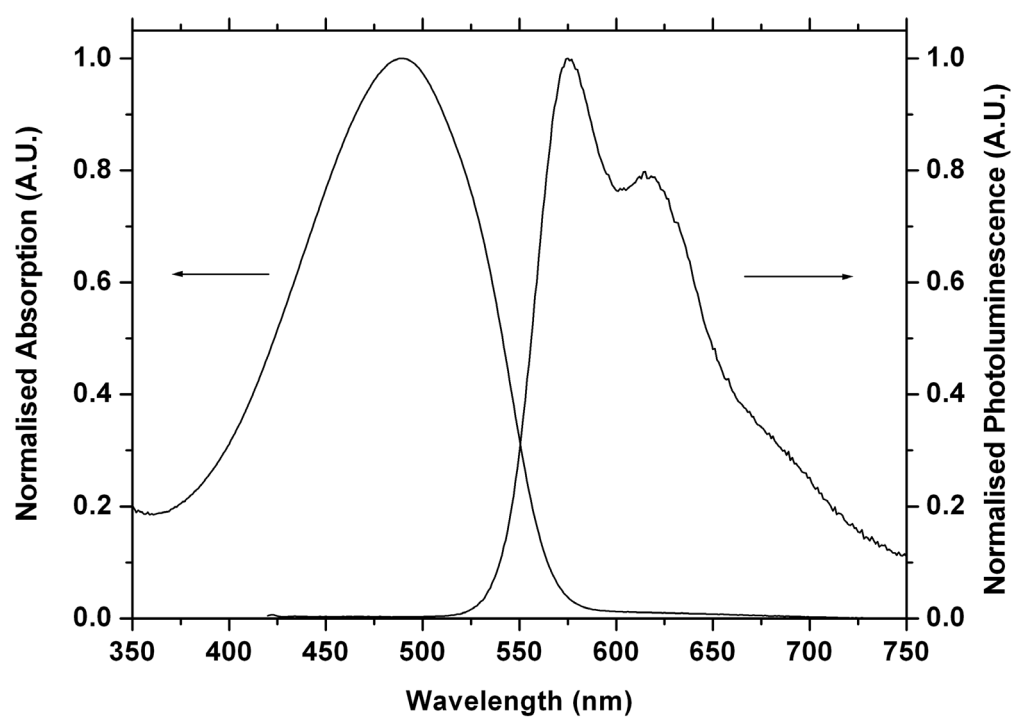


Figure 2.6: The absorption and emission spectra of the polymer MEH-PPV.

Numerous experiments have demonstrated evidence for the migration of excitons along the polymer chains, including work by Bässler *et al.* where PPV chain segments can be excited by using a sharply tuned laser [12]. Other work by Samuel *et al.* [22] studied time resolved luminescence data as a function of temperature. They found that while at room temperature the decay of luminescence is the same across the whole spectrum, there is a shift to the red as time increases at 77 K. This was attributed to the migration of excitons along the chain to longer, low energy segments.

2.1.4 Gain in conjugated polymer systems

In order to understand the processes that lead to gain and the amplification of light passing through a polymer medium, we should consider a system consisting of two energy levels E_1 and E_2 , with corresponding population densities N_1 and N_2 . A schematic of which is shown below in figure 2.7. There are three ways that light may interact with this system.

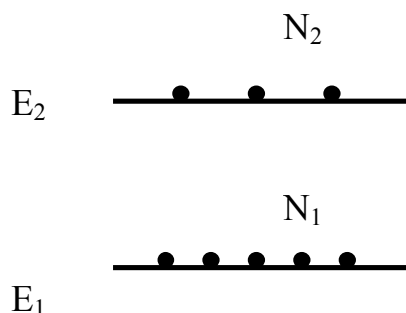


Figure 2.7: Two level system depicting ground state and 1st excited state with population densities N_1 and N_2 .

Firstly, an electron in the upper state may undergo a spontaneous relaxation back to the lower state and emit a photon in doing so. The emission will be incoherent due to the random nature of the relaxation. The average time an electron will remain in a given state is designated the lifetime τ . Hence, the spontaneous flow of electrons from state 2 to state 1 is given by:

$$-\frac{dN_2}{dt} = A_{21}N_2 \quad [2.1]$$

Where A_{21} is the Einstein A coefficient, and is the inverse of the lifetime τ_2 .

Secondly, an incoming photon may be absorbed, promoting an electron from the lower to the upper state. The flow of electrons from state 1 to state 2 can be given as:

$$\frac{dN_2}{dt} = B_{12}\rho_\nu N_1 \quad [2.2]$$

Here, ρ_ν is the photon number density at a frequency ν and B_{12} is the Einstein B coefficient for the transition $E_1 \rightarrow E_2$.

Finally, for the case of stimulated emission, an incoming photon may cause an electron in the upper state to relax, emitting an additional photon. These photons are coherent and have the same frequency and phase. The stimulated emission flow from state 2 to state 1 is given by equation 2.3:

$$-\frac{dN_2}{dt} = B_{21}\rho_\nu N_2 \quad [2.3]$$

B_{21} is the Einstein B coefficient for the transition $E_2 \rightarrow E_1$.

Stimulated emission allows the amplification of an incoming stream of photons (two photons out for one photon in). Under normal conditions however, the ratio between stimulated and spontaneous emission is very poor. Thus, to boost the amount of stimulated emission, we need to maximize the values of N_2 and ρ_ν .

If we consider the absorption of light through an amplifying medium of length x , we can relate the light intensity at a frequency ν , I_ν to an absorption coefficient α using equation 2.4:

$$\frac{dI_\nu}{dx} = -\alpha I_\nu(x) \quad [2.4]$$

We can see from this that if α is negative, then the material will amplify the incoming light. It can be shown [23] that by considering the comparative rates of stimulated emission to stimulated absorption through an amplifying media, i.e.

$$\frac{dD_\nu}{dt} = N_2 \rho_\nu B_{21} - N_1 \rho_\nu B_{12} \quad [2.5]$$

(where D_ν is the photon number density) and the degeneracy (g) of the energy levels from Boltzmann statistics (equation 2.6)

$$\frac{N_1}{N_2} = \frac{g_1}{g_2} e^{\frac{E_2 - E_1}{kT}} \quad [2.6]$$

if we can create a situation where $N_2 > \frac{g_2}{g_1} N_1$ (a population inversion), then α is always negative and the medium will amplify.

For a two level system under intense optical pumping, there is as much chance of causing stimulated absorption as there is of stimulated emission and so at best, the material will become bleached. For a conjugated polymer, the energy level system is similar to that of a four level laser [24], where rapid, radiationless transitions from the upper excited state to the upper laser level (a) and lower laser level back to the ground state (b) allow a population inversion to be maintained relatively easily. A typical four level laser system is shown below in figure 2.8.

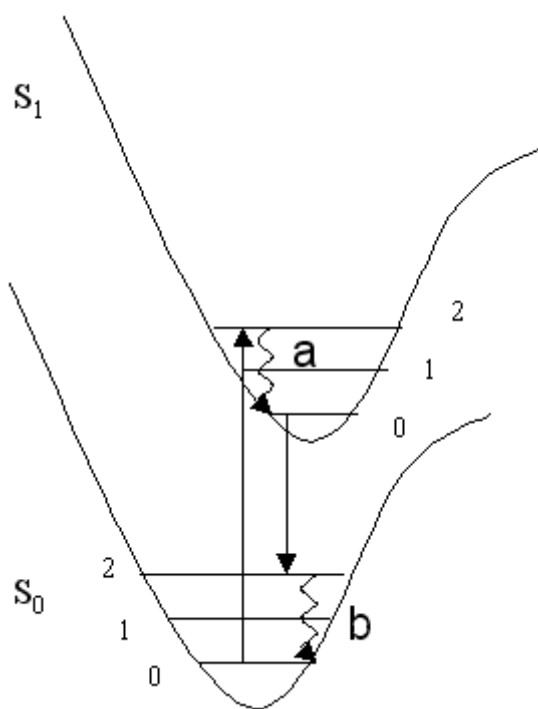


Figure 2.8: Structure of a four level laser system showing the main energy transitions.

Transitions (a) and (b) are fast, radiationless transfers that allow a population inversion to be maintained between the upper and lower laser levels.

The potential gain from a laser material can be characterised in terms of a gain coefficient (g) and a loss coefficient (α). As a beam passes through a gain medium, the change in intensity is given by equation 2.7.

$$I = I_0 e^{[(g-\alpha)L]} \quad [2.7]$$

Here, I is the emission intensity and L is the length of the gain medium. Furthermore, the gain coefficient is related to the excited state density n and the stimulated emission cross section σ by $g = n\sigma$. Conjugated polymers should therefore be able to achieve high gain due to their large stimulated emission cross-section (10^{-16} cm^2) and strong absorption (10^5 cm^{-1}), attributes clearly displayed in the work by Tessler [25] where he demonstrated lasing from a conjugated polymer film only 100 nm thick.

The maximum level of gain will however be diminished by losses in the material and these must be minimised for efficient amplification. One mechanism for such losses is self-absorption, where the absorption and emission spectra overlap. In a conjugated polymer however, the absorption and emission are usually well separated (although it still has a small effect) due to the migration of excitons along the chain and a Stokes shift, as was described earlier. Another possibility is excited state absorption, either from absorption by a radiative state lying at a higher energy or by triplet absorption. While triplet absorption is a problem in laser dyes, it normally lies at a lower energy than the emission in conjugated polymers [26]. The emission from the polymer is also subject to losses. Chemical defects such as oxygen along the chain can promote photo-oxidation of the backbone, forming carbonyl groups. These quench the luminescence of the polymer quite effectively [27].

2.2 Polymer Lasers

In this section, we move on from discussing the inherent properties of the conjugated polymers themselves to the physical principles and methods for controlling the emission. Guiding the waves within a structure allows light to propagate long distances (e.g. optical fibres) and applying wavelength scale microstructure to devices allows for the manipulation of the output. One example of this is providing feedback for the operation of polymer lasers [28-30] and another is improving the efficiency of organic light emitting diodes [31]. In spin coating a thin layer of organic semiconductor onto a suitable substrate (e.g. fused silica), the polymer can act as an optical waveguide, the mechanisms of which, are described in the following section.

2.2.1 Waveguiding

To understand the interaction of guided waves, it is important to have knowledge of how guided modes propagate. A planar slab waveguide model, for which no variations exist in one of the dimensions, (for example, y) can be used to analyse the modes. A mode of a dielectric waveguide is a solution of the Helmholtz equation, given below.

$$\nabla^2 E(r) + k_0^2 n^2(r) E(r) = 0 \quad [2.8]$$

Where we have the free space propagation constant, $k_0 = (2\pi/\lambda)$ and n is the index of refraction. Solutions are subject to the continuity of the tangential components of \mathbf{E} and \mathbf{H} at the dielectric interfaces and take the form

$$E(r, t) = E(x, y) e^{i(\alpha x - \beta z)} \quad [2.9]$$

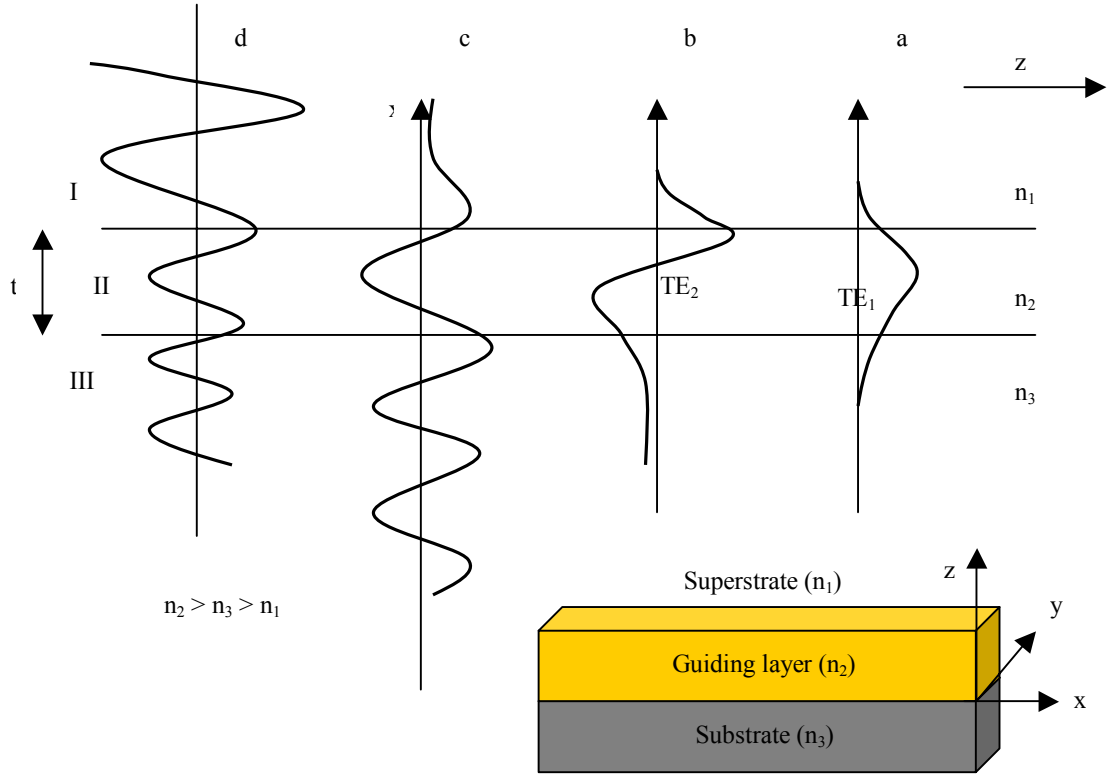


Figure 2.9: Possible solutions to the Helmholtz equation. The inset shows the structure of a three-layer waveguide.

Selected solutions for equation 2.8 as a function of the propagation constant β at a fixed frequency ω are plotted in figure 2.9. For $\beta > k_0 n_2$ (not shown), $E(x)$ is exponential in all three layers (I, II and III) of the waveguide. The field increases without bound away from the waveguide and so is not physically realizable. In solutions a and b, we have the case $k_0 n_3 < \beta < k_0 n_2$. Here, the field decays exponentially in the substrate and superstrate but is sinusoidal in the guiding layer, where it is confined. Consequently, these solutions are designated confined or guided modes and is only possible when $n_2 > n_1, n_3$.

When $k_0 n_1 < \beta < k_0 n_3$ (regime c), the field only decays exponentially in the superstrate with regions II and III having sinusoidal behaviour. This is a substrate radiation mode. The final case (d) where $0 < \beta < k_0 n_1$, the field is sinusoidal in all layers and is designated a radiation mode.

In the propagation regime $k_0 n_3 < \beta < k_0 n_2$, the allowed values of β are discrete and hence the number of confined modes depends on the thickness t , the frequency and the index of refraction. For a given wavelength the number of confined modes increases from 0 as you increase the thickness t allowing higher order modes to be confined within the waveguide.

For an asymmetric waveguide, one should limit the derivation to guided modes that have propagation constants in the region of $k_0 n_3 < \beta < k_0 n_2$, where $n_3 > n_1$. Acceptable solutions should be continuous at both $x = 0$ and $x = -t$ [23]. By imposing this requirement we get

$$\tan(ht) = \frac{p + q}{h(1 - pq/h^2)} \quad [2.10]$$

Where

$$h = (n_2^2 k_0^2 - \beta^2)^{0.5} \quad [2.11]$$

$$q = (\beta^2 - n_1^2 k_0^2)^{0.5} \quad [2.12]$$

$$p = (\beta^2 - n_3^2 k_0^2)^{0.5} \quad [2.13]$$

Thus, we can calculate a field profile for a given layer thickness t at a wavelength λ if we know the refractive indices for the waveguide layers. In figure 2.10 below, the field profile for a 150 nm thick layer of the polymer MEH-PPV is presented. The substrate here is silica ($n_1 = 1.47$) and the superstrate layer has $n_3 = 1.56$ (corresponding to that of a commercial optical adhesive used in some of the later work presented in this thesis). The polymer refractive index, n_2 is 1.88 (at a wavelength of 630 nm) as measured through ellipsometry. The mode profile was calculated using the Mathematica package [32].

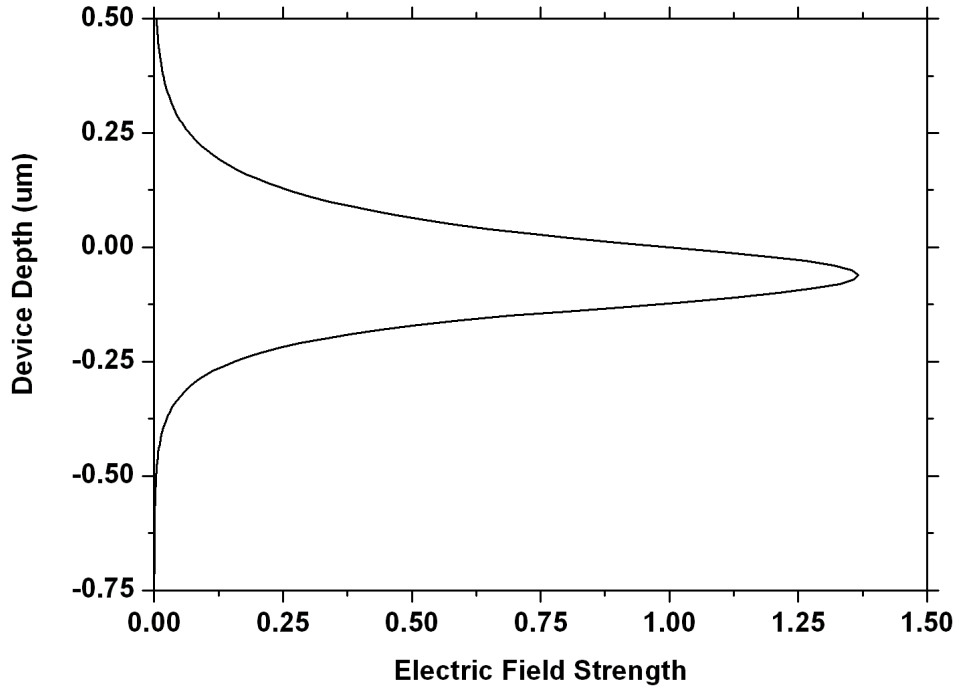


Figure 2.10: Electric field (TE_0) profile at $\lambda = 630$ nm for a 150 nm thick film of MEH-PPV clad between layers of refractive index 1.47 (substrate) and 1.56 (superstrate).

Film position is from 0 to $-0.15 \mu\text{m}$.

2.2.2 Feedback Structures

In addition to having a gain medium, to fabricate a successful laser system, one must also provide a suitable feedback mechanism to amplify the oscillations. Usually, this takes the form of a pair of mirrors for conventional laser systems, with the reflectivity of one mirror below 100% to allow an output. This was the approach used in fabricating the first solution based polymer laser [33].

After the observation of stimulated emission from a conjugated polymer by photopumping a solution of MEH-PPV, work by Tessler *et al.* [25] and Hide *et al.* [34] demonstrated lasing from a thin film of conjugated polymer using different geometries to provide the feedback. In the remainder of this section, a number of different geometries are reviewed, with the focus being placed upon the mechanism primarily used throughout this thesis.

Cleaved Facets

Cleaving the edge of a waveguide structure can allow the device to operate as a resonator. Typically employed in inorganic crystalline semiconductors, the facets can partially reflect light back along the waveguide where it is totally internally reflected. For conventional semiconductors, the difference in refractive index between the crystal and the surroundings can be large, allowing reflectivity of $\sim 30\%$. The refractive index of conjugated polymers is much lower however reducing this value to 10% or less. In addition, most organic materials are amorphous and are difficult to cleave successfully.

Microcavities & Distributed Bragg Reflectors (DBR)

When a gain medium is placed within a Fabry-Perot oscillator of length corresponding to the emission wavelength, a microcavity is formed. Emitted light is coupled to the cavity modes resulting in narrowing and a degree of control over the emission [35,36]. An advantage of the microcavity design is the ease of fabrication, being similar in structure to that of an OLED. Emission is perpendicular to the substrate.

A Distributed Bragg Reflector (DBR) is a type of microcavity consisting of the gain medium surrounded by alternating layers of low and high refractive index, causing a periodic perturbation. The resulting in plane structure gives rise to a high reflectivity. Laser action reported in a polymer/small molecule blend by Berggren *et al.* was fabricated using a DBR geometry [37].

Bragg Scattering

Periodic scattering centres within a waveguide can modify the propagation of light through it. The process of light being diffracted from the centres is known as Bragg scattering. Most simply, this is the diffraction from multiple slits such as atoms within a crystal or rulings on a grating. In a microstructured waveguide, a periodic modulation of the waveguide thickness can lead to the same effect causing the guided waves to be either reflected back along or scattered out of the medium.

The Bragg condition is given by equation 2.14

$$\frac{2\pi}{\lambda} \sin(\theta) = \pm \frac{2\pi n_{eff}}{\lambda} \pm m \frac{2\pi}{\Lambda} \quad [2.14]$$

Where Λ is the period of the grating structure and n_{eff} is the effective index of the waveguide. The angle θ refers to the angle between the incident ray and the scattering planes. The two processes described above result from either first order ($m = 1$) or second order scattering, giving rise to output coupling or feedback respectively. A schematic of first and second order Bragg scattering is given in figure 2.11, below.

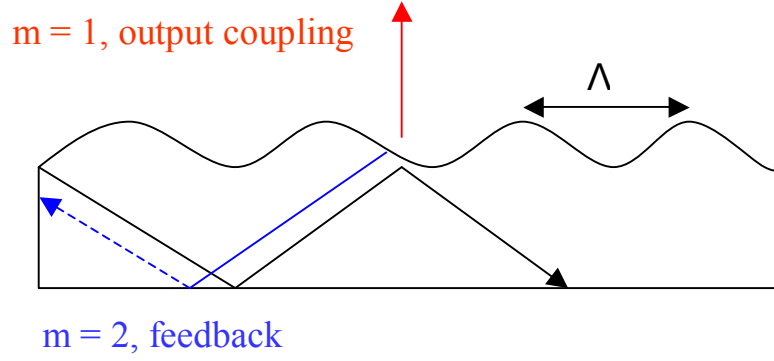


Figure 2.11: First and second order Bragg scattering from a periodic waveguide.

2.2.3 Distributed Feedback Lasers

The incorporation of periodic microstructure into a polymer waveguide device provides the geometry required for a Distributed Feedback (DFB) laser. Typically, this is a periodic change in the refractive index in the plane of the gain medium. DFB lasers were introduced by Kogelnik and Shank in the 1970s [38], where interference patterns were used to introduce a periodic refractive index change in gelatin. McGehee *et al.* [28] demonstrated the first polymer DFB laser using BuEH-PPV as a gain medium. Since then, performance has been improved through techniques such as using 2D gratings as in the work by Turnbull *et al.* [29] (threshold = 4 nJ, efficiency = 6.8% on one side) and promoting feedback in all directions in the plane by fabricating circular gratings [39-41]. The use of different polymers allows lasing in different parts of the visible spectrum such as the blue DFB laser (threshold = 0.8 nJ, efficiency = 7.8%) using polyfluorene demonstrated by Heliotis *et al.* [42]. Varying the film thickness or changing the period of the grating [43] allows the emission wavelength to be varied. Unlike cavity types such as the microring [44,45], the lasing emission also forms a good output beam.

A DFB laser has a distinctive stop band around the Bragg wavelength, within which light cannot propagate. At the edges of this stopband the light can propagate and experiences feedback. Let us consider a second order DFB laser such as the one depicted earlier in figure 2.11 and used throughout this work. If we look at the distribution of the electric field in the gain medium, given by $E_m(x,z)\exp(i\beta_m z)$.

The complex amplitude is given by:

$$E_m(x, z) = R(z)E_m^{(0)}(x) + S(z)E_m^{(-2)}(x) \quad (m \neq 0, -2) \quad [2.15]$$

$$E_m(x, z) = R(z)E_0(x) \quad (m = 0) \quad [2.16]$$

$$E_m(x, z) = S(z)E_{-2}(x) = S(z)E_0(x) \quad (m = -2) \quad [2.17]$$

Here, the $m = 0, -2$ modes correspond to the guided mode propagating in the $\pm z$ direction. $R(z)$ and $S(z)$ are their slowly varying amplitudes in the z direction. The radiation mode or the $m = -1$ mode represents travelling waves in the vertical $\pm x$ direction. This mode (and all other modes where $m \neq 0, 2, -1$) derives its energy from the interaction with the guided modes.

$R(z)$ and $S(z)$ are related through coupling coefficients for the interaction between counterpropagating guided waves (usually designated κ) and also through indirect coupling between the partial waves (for $E_m(x)$, $m \neq 0, -2$). Solutions of $R(z)$ and $S(z)$ satisfying the coupling equations and boundary conditions ($R(0) = S(L) = 0$) are of the form:

$$R(z) = \sinh(\gamma z) \quad [2.18]$$

$$S(z) = \pm \sinh(\gamma(z - L)) \quad [2.19]$$

γ is a parameter that contains the direct and indirect coupling coefficients, the gain (g) and the detuning from the Bragg wavelength (Δk). γ can be rewritten, multiplied by the length of the region propagation occurs over (L), such that:

$$\gamma L = \sqrt{(g + i\Delta kL + Lh_1)^2 - (iLh_2 - Lh_1)^2} \quad [2.20]$$

Where the coupling coefficients specifically for the output coupling and feedback modes are given as h_1 and h_2 respectively. Thus, when all conditions are satisfied (i.e. the oscillation threshold condition), the following is true:

$$D \equiv \gamma L \cosh(\gamma L) - (g - Lh_1 + i\Delta k L) \sinh(\gamma L) = 0 \quad [2.21]$$

Upon plotting the parameter D as a function of gain value g , and the detuning from the Bragg wavelength ($\Delta k L$), a contour plot is obtained containing the points where equation 2.21 is satisfied. These are the longitudinal laser modes. An example for a MEH-PPV laser with an imprinted 25 nm deep sinusoidal grating at the air-polymer interface is shown below in figure 2.12. As well as the solutions to equation 2.21, a further trivial solution to the equation where $\gamma = 0$ (which is disregarded) can also be seen at the lower centre of the plot.

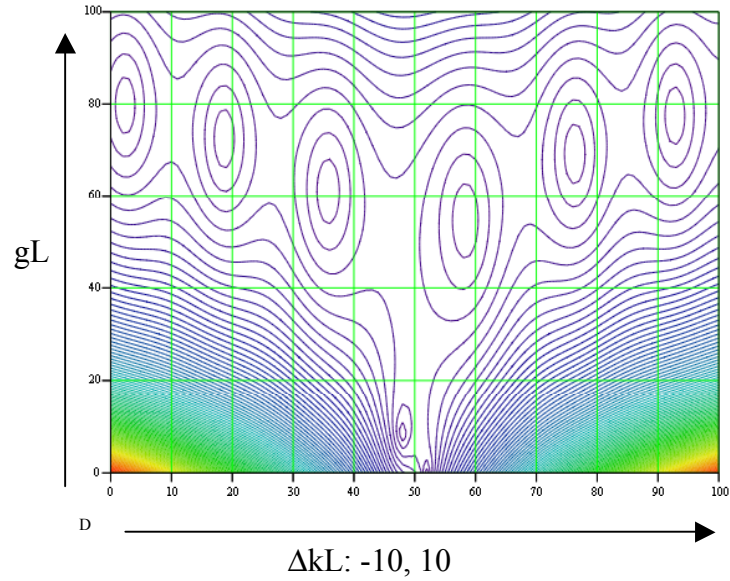


Figure 2.12: Gain contours in the g - Δk plane showing the lower order longitudinal modes.

Since $\Delta k = \beta - \beta_0 \approx (\omega - \omega_0)n_{\text{eff}}/c$ we note that no oscillations can take place exactly at the Bragg frequency ω_0 , lasing is instead established on the band edge, as discussed previously. The two lowest threshold modes are those with $m = 0$ and $m = -1$ and are positioned symmetrically on either side of the bandgap. A further comparison of calculated DFB laser modes to theoretical predictions is discussed later in chapter 4.

2.3 Summary

In this chapter, the origins of semiconductivity in conjugated polymers have been discussed. Basic photophysical principles applying to this family of materials such as absorption and emission processes, electronic configuration as well as their ability to amplify light has been presented. The processes that give rise to spontaneous and stimulated emission are described in terms of energy levels including the specific case of population inversion in a four level system.

In the latter half of the chapter, techniques to control and manipulate the flow of light through waveguides have been presented. These include various geometries from past literature as well as an analysis of the basic theory that describes the profile of an electric field in a sample. Bragg scattering has been introduced leading into a discussion of distributed feedback lasers, which forms the basis of much of the work that will be presented later in this thesis.

2.4 References

- [1] H. Shirakawa, E.J. Louis, A.G. Macdiarmid, C.K. Chang and A.J. Heeger, *Journal of the American Chemical Society: Chemical Communications*, **16**, 578-580, (1977).
- [2] J.P.J. Markham, *Highly Efficient Dendrimers and Polymers for Solution Processed Organic Light Emitting Diodes*. PhD thesis, University of St. Andrews, (2003).
- [3] R. Peierls, *Annals of Physics*, **13**, 905, (1932).
- [4] L.J. Rothberg, M. Yan, F. Papadimitrakopoulos, M.E. Galvin, E.W. Kwock and T.M. Miller, *Synthetic Metals*, **80**, 41, (1996).
- [5] N.T. Harrison, G.R. Hayes, R.T. Phillips and R.H. Friend, *Physical Review Letters*, **77**, 1881, (1996).
- [6] B.E. Kohler and I.D.W. Samuel, *Journal of Chemical Physics*, **103**, 6248 (1995).
- [7] B.E. Kohler and J.C. Woehl, *Synthetic Metals*, **84**, 851 (1997).
- [8] P.W. Atkins. *Physical Chemistry*, Oxford University Press, UK, (1994).
- [9] J.S. Blakemore. *Solid State Physics*, Cambridge University Press, UK, (1985).
- [10] W.P. Su, J.R. Schrieffer, A.J. Heeger, *Physical Review Letters*, **42**, 1698, (1979).
- [11] K. Fesser, A.R. Bishop and D.K. Campbell, *Physical Review B*, **27**, 4804, (1983).
- [12] H. Bässler, C. Brandl, M. Deussen, E.O. Göbel, R. Kersting, H. Kurz, V. Lemmer, R.F. Mahrt and A. Ochese, *Pure and Applied Chemistry*, **67**, 377, (1995).
- [13] J. Frenkel, *Physical Review*, **37**, 1276, (1931).

- [14] G.H. Wannier, *Physical Review*, **52**, 191, (1937).
- [15] M. Pope and C.E. Swenberg, *Electronic Processes in Organic Crystals and Polymers*. Oxford Science Publications, UK, (1999).
- [16] P. Wood, *Conformational Disorder and the Degree of Conjugation in Conjugated Polymers*. PhD thesis, University of St. Andrews, (2002).
- [17] B. Mollay, U. Lemmer, R Kersting, R.F. Mahrt, H. Kurz, H.F. Kaufmann and H. Bässler, *Physical Review B*, **50**, 10769, (1994).
- [18] G.R. Hayes, I.D.W. Samuel and R.T. Philips, *Physical Review B*, **52**, 11569, (1995).
- [19] M.C.J.M. Vissenberg and M.J. deJong, *Physical Review Letters*, **77**, 4820, (1996).
- [20] H. Bässler and B. Schweitzer, *Accounts of Chemical Research*, **32**, 173, (1999).
- [21] S. Heun, R.F. Mahrt, A. Greiner, U. Lemmer, H. Bässler, D.A. Halliday, D.D.C. Bradley and A.B. Holmes, *Journal of Physics-Condensed Matter*, **5**, 247, (1993).
- [22] I.D.W. Samuel, B. Crystall, G. Rumbles, P.L. Burn, A.B. Holmes and R.H. Friend, *Synth. Met.* **54**, 281, (1993).
- [23] A. Yariv, *Optical Electronics (4th Edition)*. Oxford University Press, (1991).
- [24] A. Siegman, *Lasers*, University Science Books, California, U.S.A. (1986).
- [25] N. Tessler, G.J. Denton, R.H. Friend, *Nature*, **382**, 695, (1996).
- [26] R. Osterbacka, M. Wohlgenannt, D. Chinn and Z.V. Vardeny, *Physical Review B*, **60**, 11253 (1999).
- [27] L.J. Rothberg, M. Yan, M.E. Galvin, E.W. Kwock, T.M. Miller and F. Papadimitrakopoulos, *Synthetic Metals*, **80**, 41 (1996).

- [28] M.D. McGehee, M.A. Diaz-Garcia, F. Hide, R. Gupta, E.K. Miller, D. Moses and A.J. Heeger, *Applied Physics Letters*, **72**, 1536 (1998).
- [29] G.A. Turnbull, P. Andrew, W.L. Barnes and I.D.W. Samuel, *Applied Physics Letters*, **82**, 313 (2003).
- [30] J.R. Lawrence, G.A. Turnbull and I.D.W. Samuel, *Applied Physics Letters*, **82**, 4023 (2003).
- [31] J.M. Lupton, B.J. Matterson, I.D.W. Samuel, M.J. Jory and W.L. Barnes, *Applied Physics Letters*, **77**, 3340 (2000).
- [32] Wolfram Research Inc., Mathematica, Version 4, Champaign, IL, (1999).
- [33] D. Moses, *Applied Physics Letters*. **60** (1992).
- [34] F. Hide, B.J. Schwartz, M.A. DiazGarcia and A.J. Heeger, *Chemical Physics Letters*, **256**, 424 (1996).
- [35] T. Tsutsui, N. Takada, S. Saito and E. Ogino, *Applied Physics Letters*, **65**, 1868 (1994).
- [36] D.G. Lidzey, M.A. Pate, D.M. Whittaker, D.D.C. Bradley, M.S. Weaver, T.A. Fisher and M.S. Skolnick, *Chemical Physics Letters*, **263**, 655 (1996).
- [37] M. Berggren, A. Dodabalapur, R.E. Slusher and Z. Bao, *Nature*, **389**, 466 (1997).
- [38] H. Kogelnik and C.V. Shank, *Applied Physics Letters*, **18**, 152 (1971).
- [39] C. Bauer, H. Giessen, B. Schnabel, E.B. Kley, C. Schmitt, U. Scherf and R.F. Mahrt, *Advanced Materials*, **13**, 1161 (2001).
- [40] G.A. Turnbull, A. Carleton, G.F. Barlow, A. Tahraoui, T.F. Krauss, A.K. Shore and I.D.W. Samuel, *Journal of Applied Physics*, **98** (2005).

- [41] G.A. Turnbull, A. Carleton, A. Tahraouhi, T.F. Krauss, I.D.W. Samuel, G.F. Barlow and A.K. Shore, *Applied Physics Letters*, **87** (2005).
- [42] G. Heliotis, R. Xia, G.A. Turnbull, P. Andrew, W.L. Barnes, I.D.W. Samuel and D.D.C. Bradley, *Advanced Fucntional Materials*, **14**, 91 (2004).
- [43] G.A. Turnbull, T.F. Krauss, W.L. Barnes and I.D.W. Samuel, *Synthetic Metals*, **121**, 1757 (2001).
- [44] S.L. McCall, A.F.J. Levi, R.E. Slusher, S.J. Pearton and R.A. Logan, *Applied Physics Letters*, **60**, 289 (1992).
- [45] S.V. Frolov, M. Shkunov, Z.V. Vardeny and K. Yoshino, *Applied Physics Letters*, **56**, 4363 (1997).

Chapter 3: Experimental Methods

3.1 Introduction

In this section, an overview of the experimental techniques and methods, which were used to prepare and study organic semiconductors are presented. Equipment used throughout this work to characterise devices will also be introduced. One of the major advantages of polymeric materials over their inorganic counterparts is ease of processing, especially from solution. Efficient devices can be fabricated quickly by spin-coating a single layer of polymer or dendrimer onto a substrate, minimising material consumption. This extreme ease of fabrication coupled with the ability to directly pattern the polymers on the nanometre regime is highly promising for the development of cheap, disposable organic semiconductor lasers. When also considering the great steps being taken towards large area ink-jet printing and flexible substrates in the area of organic displays, the prospects are also highly favourable for manufacturing.

3.2 Material Preparation

The light emitting materials investigated throughout this work can be divided into two categories: soluble polymers and dendrimers, and small molecular compounds. The preparation required for each of these material types will be discussed in turn.

3.2.1 Soluble polymers and dendrimers

Many common conjugated polymers such as PPV are rigid and insoluble which makes processing an inconvenience to say the least. There are two methods one may pursue in overcoming this limitation. The first is the addition of solubilising groups such as 2-ethyl-hexyloxy or *t*-butyl attached as side chain units (in the case of conjugated polymers) or at the periphery of the molecule (for dendrimers). Such groups confer solubility in many common organic solvents including chlorobenzene, toluene, tetrahydrofuran (THF) and chloroform (CHCl_3) and allow PPV derivatives such as MEH-PPV and $\text{OC}_{10}\text{C}_{10}$ -PPV to dissolve relatively quickly. The second is to use a precursor polymer material.

Depending on their molecular weight, polymers may form quite viscous solutions. For the material MEH-PPV (supplied by Covion and also by American Dye Source), the solution concentration used was typically 5 mg / ml. This provides a film thick enough for waveguiding while preventing the polymer solution entering a saturated regime (where the polymer concentration is too great for the level of solvent used and forms a gel-like material). Once added to the chosen solvent (usually chlorobenzene), the solution would be stirred at room temperature to ensure complete dissolution. After this stage, the solution may be spin-coated directly onto a substrate. The combination of varying concentration and spin speeds could be used to fine tune film thickness, a 5 mg / ml solution typically providing films between 80 and 150 nm for spin speeds of 1000 – 2000 RPM. For experiments requiring the polymer to remain in solution form rather than a thin film (such as solution based amplifier work), the concentration would be reduced as necessary.

Dendrimer materials have a much lower viscosity due to their relatively low molecular weights (typical $M_w \sim 4 \times 10^3$ for bisfluorene). Thus, in order to obtain a film sufficiently thick for waveguiding, concentrations of the order of 25 mg / ml were used. More details concerning dendrimer materials and the results gained through their use are discussed later in chapter 7.

An alternative method for producing films from conjugated polymers is to use a precursor polymer [1,2]. Precursor polymers are non-conjugated materials that are spun from solution. Thermal conversion of the precursor polymer eliminates a removable solubilising group from the molecule. For PPV derivatives, the removal of this group creates a vinylene link, fully conjugating the material. This process is depicted in figure 3.1 below. All materials used in this work were of the soluble variety, as described above.

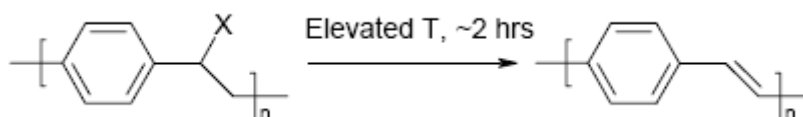


Figure 3.1: Thermal conversion of a precursor polymer under vacuum to a fully conjugated molecule (taken from [3]).

3.2.2 Small molecular compounds

Small molecular compounds do not contain solubilising groups, thus they are less soluble in organic solvents than polymers such as MEH-PPV that contain side chains. They tend to form poor quality, often semi-crystalline films when spin-coated. To process, they can either be evaporated under high vacuum (typically 10^{-6} mBar) or blended in conjunction with a dendrimer or polymer which acts as a soluble matrix. In

this thesis, small molecular compounds fill this latter role, used as host systems once blended with dendrimer materials. More details of which can be found in chapter 7.

3.3 Photophysical Characterisation

3.3.1 Absorption measurements

The absorbance of organic solutions and films was measured directly using a Cary Varian 300 UV-Vis absorption spectrometer. The sample to be measured was placed in one channel of the spectrometer. A blank sample was placed in the reference channel and acts to remove the absorption of either the quartz cuvette containing the solvent (solution based measurements) or the quartz / silica substrate for film based measurements. Prior to all measurements, a baseline scan was performed using blank substrates. This series of corrections allows the absorption of the film or solution to be measured.

The optical density is measured by comparing the reference beam to the illumination beam (both samples are illuminated equally). Assuming absorption has occurred, then the transmission through the sample T , as compared to the reference beam will be given by:

$$T = \frac{I_{sample}}{I_{reference}} \quad [3.1]$$

Where I_{sample} and $I_{reference}$ are the intensities measured through the sample and after the reference respectively. This is then converted to an absorbance using equation 3.2.

$$A = -\log(T) \quad [3.2]$$

3.3.2 Fluorescence measurements

Photoluminescence (PL) measurements were performed using a Jobin Yvon Fluoromax 2 spectrometer. A xenon lamp source is coupled to a monochromator, allowing an excitation wavelength to be selected. Emission from the illuminated sample is collected through a second monochromator (operating through a preset range) by a photomultiplier tube in photon counting mode. Readings from the spectrometer were then corrected using known calibration figures due to the quantum efficiency of the detector being greater in the blue than in the red.

3.3.3 Photoluminescence quantum yield

Measurement of the photoluminescence quantum yield (PLQY) Φ for a conjugated polymer or dendrimer is performed using an integrating sphere [4,5]. This consists of a hollow sphere internally coated with a highly reflective, diffuse material. Samples are mounted through a clip in the centre of the sphere, which collects all the emitted light. A small hole at the front of the sphere allows the entry of the excitation beam (either the 325 nm or 442 nm line of a Kimmon Helium-Cadmium CW laser depending on whether the test sample was a dendrimer or polymer).

There are two methods to collect the output from the sphere. The method of Greenham *et al.* [4] uses of a calibrated photodiode and selective cut-off filters (the method used in this work). The alternative is to use a CCD spectrometer [5]. The PLQY measures the ratio of the photons emitted by a sample compared to the number absorbed and hence provides an upper limit to the efficiency within an organic layer [4].

The calculation for the PLQY is straightforward and requires three spectral measurements. The first is the spectrum of the excitation beam with no sample present

(L_a) followed by the spectrum of the sample in place, but with the laser directed against the sphere wall (P_b). Finally, the spectrum of the laser directed against the sample is taken (P_c). Integrating these emission spectra allows calculation of the PLQY. In polymers, the luminescence results from the radiative decay (k_r) of singlet excitons, which are in competition with non-radiative processes (k_{nr}). In terms of these rates, the PLQY is given by:

$$\Phi = \frac{k_r}{k_r + k_{nr}} = \frac{\tau}{\tau_r} \quad [3.3]$$

Where the symbols τ and τ_r represent the measured emission lifetime and the natural radiative lifetime respectively. Once the measurements stated above are performed, the integrated intensities are used to calculate the PLQY as given in equations 3.4 and 3.5:

$$\Phi = \frac{P_c - (1 - A)P_b}{L_a A} \quad [3.4]$$

$$A = (1 - \frac{L_c}{L_b}) \quad [3.5]$$

A is the amount of light absorbed by the sample. L_a , L_b and L_c are the integrated intensities of the laser peak in the three measurements mentioned above.

3.4 Device Preparation

The fabrication of a polymer laser is a multiple-step process. These are namely, substrate preparation, active layer preparation and finally (in the case of devices prepared through soft-lithography) pattern transfer. Each of the steps is discussed in turn below.

3.4.1 Substrate preparation

Three types of substrates were used during this work, two of which were pre-prepared. The first of which being fused silica discs of 12 mm diameter and the second being silica substrates with a grating etched into the surface via holography (supplied by Dr. P. Andrew and Prof. W. L. Barnes from the University of Exeter). Usage of these gratings for devices is discussed later in chapter 4. The rest of the substrates were cut from silica slides (Fisher Scientific) to the desired dimensions. Typically, these were either 12 mm or 24 mm squares. All of the substrates described above were then cleaned in the same way.

Substrates were immersed in an acetone bath and ultrasonicated for 12 minutes before being dried in nitrogen. The process was then repeated for a further 12 minutes using isopropyl alcohol (IPA) before again drying in nitrogen. Especially stubborn organic material could be removed if required, by plasma-ashing in oxygen for 5 minutes at a pressure of $\sim 10^{-3}$ mbar.

3.4.2 Active layer preparation

The deposition of the active layer onto the prepared substrate is a relatively simple process. The active layer is spin-cast directly onto the clean substrate from the desired solution. By varying the spin speed, one can fine-tune the thickness of the active layer, as shown below in figure 3.2 for three films of MEH-PPV (5 mg / ml), characterised with ellipsometry. The dotted line is a model fit of a second order polynomial. MEH-PPV films were typically spun at speeds of 1100 – 1500 RPM, giving films varying between 100 and 145 nm, depending on concentration. Films not

requiring any pattern transfer were then immediately removed for testing to prevent unnecessary degradation.

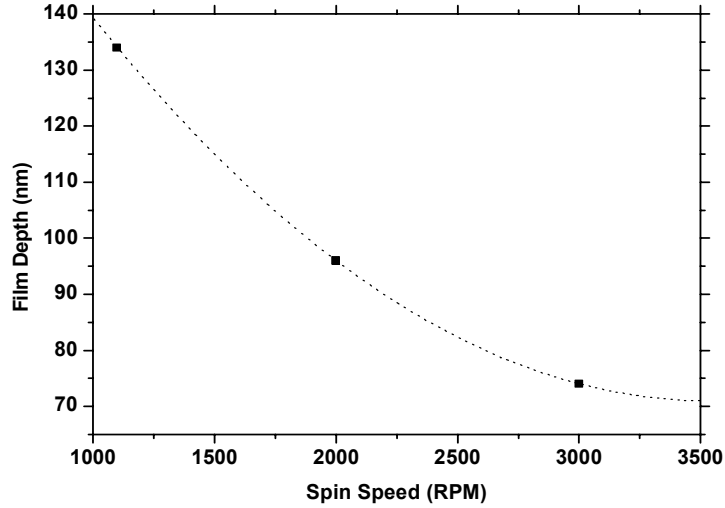


Figure 3.2: *Variation of the film thickness as a function of spin speed for a MEH-PPV solution of 5 mg / ml concentration.*

For particularly delicate samples (where exposure to air must be kept to a minimum), the above procedure would be carried out inside a nitrogen glovebox using solvents, which have been degassed prior to the fabrication process.

3.4.3 Preparation of pattern transfer elements

Transfer of the wavelength-scale gratings to the polymer-air interface was performed using a soft lithography technique known as solvent assisted micromoulding (SAMiM) [6,7]. This process involves making a replica (inverted) of a master grating in a co-polymer material, which then acts as a stamp when applied to the polymer surface. A full review of soft-lithographic techniques including SAMiM is covered later, in chapter 4.

The polymeric mould is fabricated by blending the co-polymers (supplied by Gelest GmbH) Methylhydrosiloxane-dimethylsiloxane (HMS) and Vinylmethylsiloxane-dimethylsiloxane trimethylsiloxy terminated (VDT) in the ratio of 3.4 parts VDT to 1 part HMS, as per the work conducted by Schmid and Michel [8]. The chemical structures of these polymers are shown below in figure 3.3. A platinum catalyst (Platinum-divinyl tetramethyl-disiloxane complex) is added to the VDT (a few ppm) and stirred in a beaker before adding the HMS. A silica master, which has been previously cleaned in a mixture of sulphuric acid (95 % w/v) and hydrogen peroxide (30 % w/v) to remove any organic residue on the grating surface is placed face up in a small plastic sample container before the co-polymer mixture is poured over the surface. The sample is then cured for 24 hours at a temperature of 70°C. After curing, the sample is carefully removed from the mould while the co-polymer is still warm and easily workable. The completed mould is then allowed to cool to room temperature under ambient conditions before use.

Once cured, the mould is inked with a suitable solvent before being brought into conformal contact with the polymer surface. The solvent flows around the relief grating allowing the polymer to conform to the shape of the mould. The entire stamping process is complete within three minutes although substantial transfer of the pattern from mould to polymer occurs in less. After this time period is complete, the finished polymer device is carefully removed from the mould, which is re-useable and shows little degradation over many months of applications.

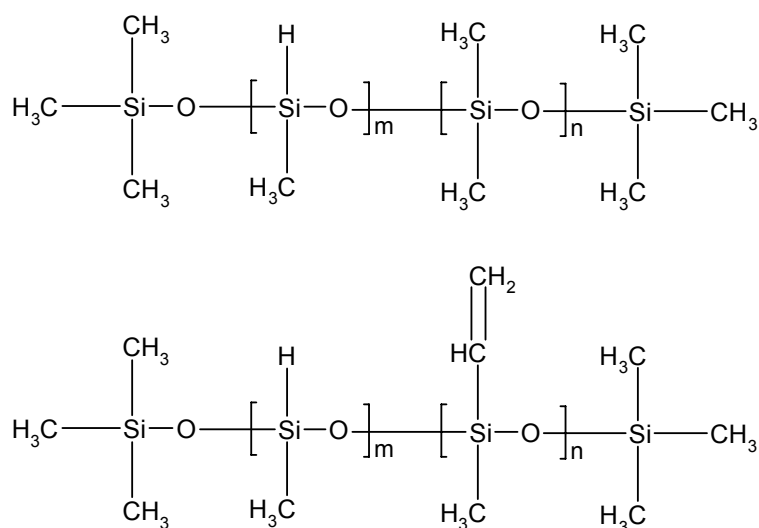


Figure 3.3: The chemical structures of the co-polymers HMS (top) and VDT (bottom), used in the fabrication of rubber moulds for soft lithography.

3.5 Device Characterisation

In this section the main equipment and techniques used to characterise the polymer and dendrimer lasers are presented. The processes used fall under two main categories, those used to map the device topography and those used to probe the photophysical performance of the samples. Each will be discussed in turn below.

3.5.1 Atomic Force Microscopy

An atomic force microscope (AFM) is a powerful high-resolution scanning tool and has been one of the foremost tools for imaging and measuring matter on the nanoscale since its inception by Binnig, Quate and Gerber twenty years ago [9].

An AFM consists of a cantilever, usually constructed from silicon or silicon nitride with a sharp probe at one end, which is then mounted on a piezo-driver unit. The tip, which has a radius of curvature of the order of a few nanometres is brought into close proximity with the surface of a sample where surface forces deflect the cantilever

according to Hooke's law. This deflection can be monitored through a laser spot focussed onto the cantilever. The reflected beam is incident on a segmented photodiode, which controls the level of feedback sent to the cantilever. The piezoelectric unit moves the tip over the surface of the sample while controlling the z height, forming a topographical map of the surface features. The system can be run in two main modes. In "contact" mode, the force between the tip and the surface is kept constant and feedback is provided through the static tip deflection. In "tapping" mode, the tip is oscillated close to resonant frequency. The amplitude and phase information are modified by the tip-sample interactions and the changes are compared to an external source to provide information about the surface characteristics.

As microstructure plays such a vital role in determining the characteristics of semiconducting polymer lasers, it is thus important to have an accurate picture of the quality of pattern transfer through techniques such as soft lithography. Knowledge of imperfections and defects caused by the lithographic processes will in turn help to produce better devices. A Vista Scanning Probe AFM supplied by Burleigh was used to characterise the devices presented in this work. Calibration was performed using ultrasharp silicon gratings of known pitch and step height (silicon MDT). AFM scans were corrected for deviations in the level of the plane by subtracting the background slope using the inbuilt software. The panels of figure 3.4 show a schematic of the AFM operation (top), and a topography map for a $5\text{ }\mu\text{m} \times 5\text{ }\mu\text{m}$, 90 nm deep section of a 2-D grating, formed in MEH-PPV via soft lithography (bottom).

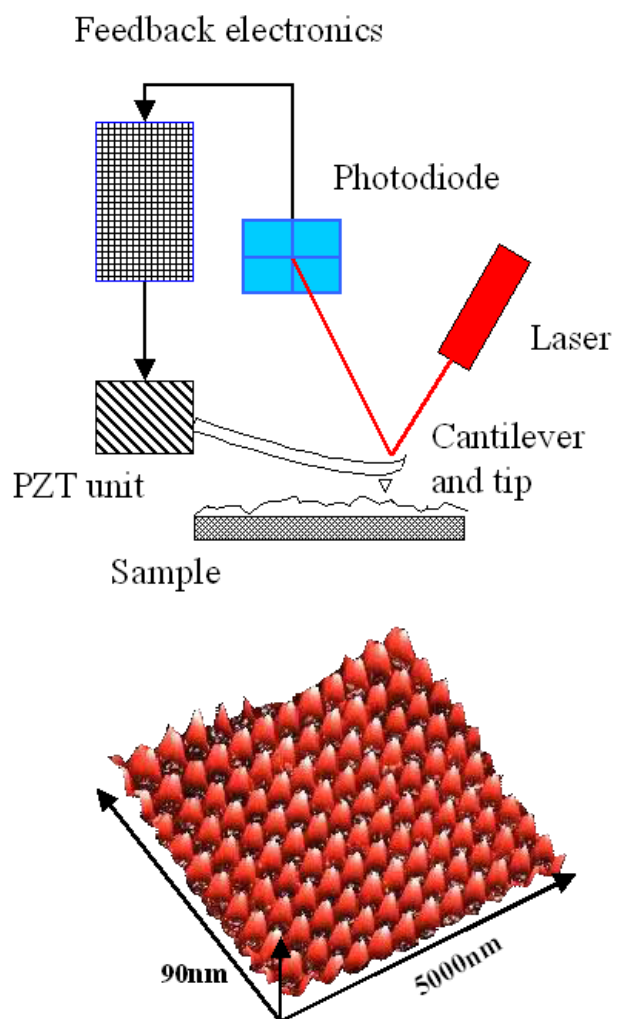


Figure 3.4: Schematic displaying the operation of an AFM (top panel). The lower panel contains a scan of a 90 nm deep, $5\ \mu\text{m} \times 5\ \mu\text{m}$ area of a 2-D ‘eggbox’ grating which has been imprinted in MEH-PPV using soft lithography.

3.5.2 Ellipsometry measurements

Variable Angle Spectroscopic Ellipsometry (VASE) [10,11] is a powerful optical technique for investigating the dielectric properties (both complex refractive indices and dielectric functions) of thin films, finding applications in microelectronics and biology as well as the field of semiconductor physics. An ellipsometer measures the change in the polarisation of light upon reflection from a sample; deriving its name from the fact the most general state of polarisation is elliptic.

The inbound radiation is emitted from a light source and passes through a linear polariser hitting the sample surface and being reflected in the plane of incidence towards the detection unit. The angle of incidence is equal to the angel of reflection. The elliptical polarisation state of the light on reflection can be decomposed into an s and a p component (where the s component oscillates perpendicular to the plane of incidence and the p component oscillates parallel to the plane).

The fundamental equation used in ellipsometry is described by the following:

$$\rho = \frac{r_p}{r_s} = \tan(\Psi)e^{i\Delta} \quad [3.6]$$

Standard ellipsometry measures two of the four Stokes parameters, conventionally named Δ and Ψ where Δ is the phase shift upon reflection and $\tan\Psi$ is the amplitude ratio. The amplitudes of the s and p components, taken after reflection and normalised to their initial value are denoted by r_s and r_p respectively. As ellipsometry is measuring this ratio of values rather than the absolute value of either, it

is a very robust, reproducible method that is relatively insensitive to fluctuations. A schematic showing the basic operating principle of ellipsometry is shown below in figure 3.5. The particular model used in this study was a J.A.Woolam Co. Inc. M-2000DI.

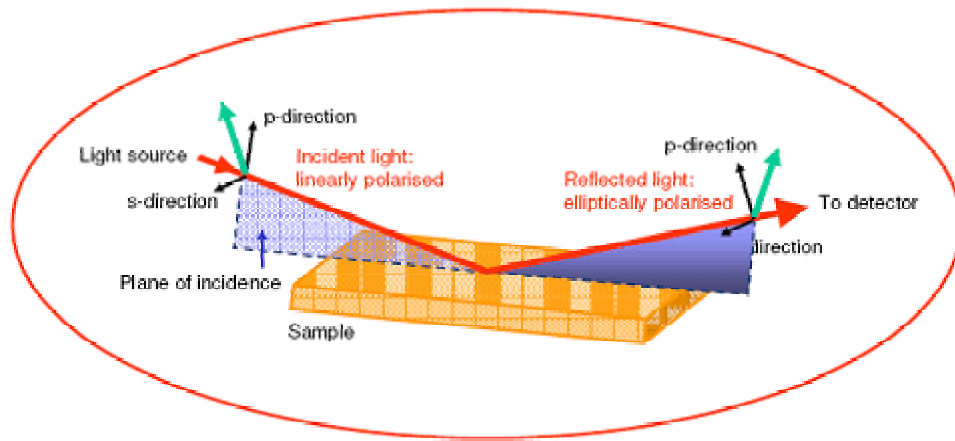


Figure 3.5: Overview of ellipsometer operation displaying the change in polarisation of the incident ray upon reflection on the sample surface.

Data analysis for ellipsometry is an indirect method – the measured Δ and Ψ generally cannot be directly converted to the optical constants for the sample apart from very simple cases for isotropic, homogeneous and infinitely thick films. In general cases, a layer model is established which considers the optical constants and thickness parameters of the individual layers in the sample, in the correct sequence. A least squares iterative procedure varies the unknown optical constants and/or film thickness and calculates Δ and Ψ values using the Fresnel equations. The calculated values are compared to the experimental data, the best fit of the model to the data, provides the optical constants and thickness of the sample.

For the measurements contained within this thesis, the ellipsometer was calibrated prior to each run using a silicon wafer covered with a SiO₂ layer approximately 18 nm thick. A model with known parameters is supplied with the equipment for this material and is described in the literature by Herzinger *et al.* [12]. Fused silica substrates were preferred to borosilicate glass due to being transparent well into the UV part of the spectrum and also because of the extensive modelling which was already established for MEH-PPV films on these substrates [13].

Data for each sample was taken at 5° intervals for angles between 45° and 75° and at 2° intervals between 57° and 63°. The spread in angles allows more constraint over the fitting parameters when applying the model (several sets of parameters can match a single data set well as solutions are not unique). The measurements are also more sensitive around Brewster's angle (~ 60° for MEH-PPV) where they show strong variations in the Δ data, adding further constraints to the parameter fitting. Normal incidence transmission data is used in the modelling in addition to Ψ and Δ values, the quality of the fit to the intensity transmission gives confidence the right set of optical constants have been used. Transmission data in particular is very effective in helping to determine the film thickness (forcing fitted curves to match the maximum of the absorption spectrum).

3.5.3 Laser characterisation

In order to characterise the quality of semiconducting polymer lasers, devices were tested for efficiency (energy out / energy in) and for threshold. A suitable pump source is chosen to coincide with the absorption spectra of the material in question. Typically, for MEH-PPV films, this was the $\lambda = 532$ nm output of a frequency doubled,

passively Q-switched Nd:YVO₄ microchip laser (Alphas Lasers GmbH). For devices fabricated from the blue-emitting bisfluorene dendrimer, either the $\lambda = 355$ nm third harmonic of the microchip laser or the $\lambda = 337$ nm output of a nitrogen laser was used. Output from both pump sources would be focussed to the required dimensions using appropriate lenses and attenuated using calibrated neutral density filters. The microchip laser supplies 1 ns pulses at a frequency of 5 kHz. Un-attenuated pulse energy is $\sim 1 \mu\text{J}$ / pulse for the 532 nm emission. The frequency of the nitrogen laser can vary between 0 and 20 Hz. Pulse duration is 500 ps.

The pump beam is aligned to be incident on the top surface of the polymer film (usually an air-polymer interface). The sample is rotated $\sim 10^\circ$ from the normal to prevent reflections back along the beam path. Emission from the sample is collected close to normal incidence using a fibre coupled CCD spectrometer (Triax 180, J.Y. Horiba). A schematic of the general experimental set-up is shown below in figure 3.6.

A series of emission spectra are recorded for varying excitation energies both above and below device threshold. After removing the background, the resulting spectra can then be integrated with respect to wavelength to give relative output power, which varies linearly above threshold. A calibrated power meter (Molelectron) is used to record the absolute value of the emission energy from both the device and the excitation source separately with appropriate filters being applied to remove the unwanted component in each case. The power readings are then corrected using supplied calibration files (the energy response of the power meter is not linear for all parts of the spectrum).

The corrected readings are then used to plot the relationship between input energy and output energy as shown below in figure 3.7 (taken from [14]). Shown is the performance of a MEH-PPV film spin-cast onto a corrugated silica substrate. For this

sample, there is a sharp increase in the gradient of the slope at 4 nJ indicating the threshold. Finally, the power characteristics of the laser can be extracted, namely in this case, a threshold of 4 nJ / pulse and an efficiency of 6.8 % on one side. Efficiency values from the lasers characterised in this thesis (unless stated otherwise) are for the output from one side of the device.

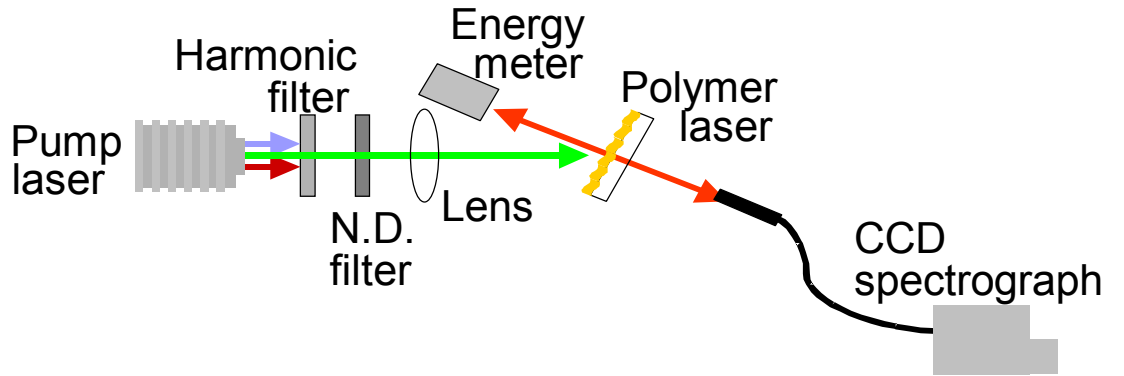


Figure 3.6: Experimental setup for testing the polymer lasers presented in this work.

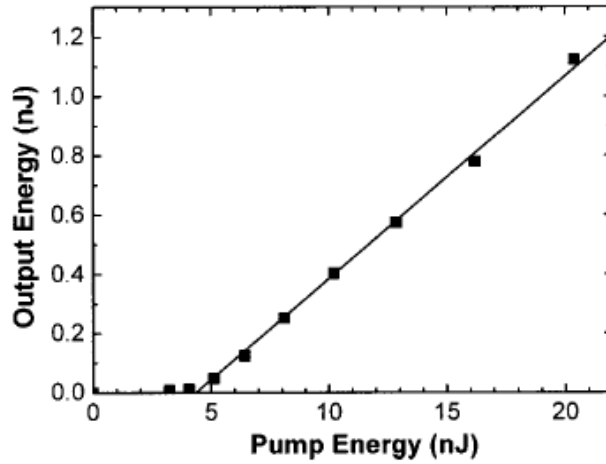


Figure 3.7: Output energy of a MEH-PPV laser as a function of input energy. Device efficiency is 6.8 % (on one side) with a threshold of 4 nJ / pulse (taken from [14]).

3.6 References

- [1] D.A. Halliday, D.D.C. Bradley, P.L. Burn, R.H. Friend and A.B. Holmes. *Synthetic Metals*, **41-43**, 931, (1991).
- [2] W. Bijmens, M. Van Der Borght, J. Manca, W. DeCeuninck, L. DeSchepper, D. Vanderzande, J. Gelan and L. Stals. *Optical Materials*. **9**, 150, (1998).
- [3] J.P.J. Markham. *Highly Efficient Dendrimers and Polymers for Solution Processed Organic Light Emitting Diodes*. PhD thesis, University of St. Andrews, (2003).
- [4] N.C. Greenham, I.D.W. Samuel, G.R. Hayes, R.T. Phillips, Y.A.R.R. Kessener, S.C. Moratti, A.B. Holmes and R.H. Friend. *Chemical Physical Letters*. **241**, 89, (1995).
- [5] J.C. deMello, H.F. Wittmann and R.H. Friend. *Advanced Materials*. **9**, 230, (1997).
- [6] E. Kim, Y. Xia, X.-M. Zhao and G.M. Whitesides. *Advanced Materials*. **9**, 651, (1997).
- [7] J.R. Lawrence, G.A. Turnbull and I.D.W. Samuel, *Applied Physics Letters*, **82**, 4023 (2003).
- [8] H. Schmid and B. Michel. *Macromolecules*. **33**, 3042, (2000).
- [9] G. Binning, C.F. Quate and C. Gerber, *Physical Review Letters*, **56**, 930 (1986).
- [10] J.A. Woollam, B. Johs, C.M. Herzinger, J. Hilfiker, R. Synowicki and C.L. Bungay, *SPIE, Critical Reviews of Optical Science and Technology*, **CR72** (1999).
- [11] B. Johs, J.A. Woollam, C.M. Herzinger, J. Hilfiker, R. Synowicki and C.L. Bungay, *SPIE, Critical Reviews of Optical Science and Technology*, **CR72** (1999).

- [12] C.M. Herzinger, B. Johs, W.A. McGahan, J.A. Woollam and W. Paulson, *Journal of Applied Physics*, **83**, 3323 (1998).
- [13] Olivier Gaudin, Private Communication.
- [14] G.A. Turnbull, P. Andrew, W.L. Barnes and I.D.W. Samuel, *Applied Physics Letters*, **82**, 313 (2003).

Chapter 4: Soft lithography for polymer lasers

4.1 Introduction

The ability to manipulate and control the emission of light through the use of wavelength scale microstructure is especially important for the development of polymer lasers. The grating that is applied is responsible for generating the feedback in the device [1]. A number of grating geometries in the plane of the material have been reported for distributed feedback polymer lasers over the years. These include square lattices [2-6], hexagonal [7-9], honeycomb [8], circular [10-12] and even random scattering structures [13,14]. All reports show a variety of processing conditions and beam characteristics.

In many of these reports, the microstructure is positioned at the substrate-polymer interface through traditional lithographic means. Using equipment such as electron beam lithography is a time consuming, expensive process however and negates one of the key aspects of conjugated polymers: their ease and speed of processing from solution. Perhaps a more desirable solution is to apply the microstructure quickly and simply to the polymer device, which is the motivation behind the group of techniques collectively, termed soft lithography [15].

In this chapter, a brief review of a number of soft lithographic methods is presented. One of these techniques, solvent assisted micromoulding is used to fabricate a number of polymer DFB laser devices. A study of how the depth varies in these devices and its impact on the lasing threshold is examined, including devices with exceptionally deep grating structures in the polymer surface, approaching that typically

associated with gratings etched in silica through conventional means. Later in the chapter, solvent assisted micromoulding is used to pattern a MEH-PPV film with a circular grating. The results are compared to lasers formed on pre-etched substrates. Finally, a flexible polymer laser is presented, fabricated by spin-coating a thin plastic substrate and imprinting the polymer layer. Flexible polymer lasers offer many benefits to the end user such as conforming to curved surfaces and being inherently more robust than rigid devices. The results from this study are again compared to devices fabricated on silica substrates.

4.2 Review of lithographic techniques

In this section, a variety of lithographic methods for imprinting wavelength scale microstructures into a device will be reviewed. There are two main processes used in the fabrication of such structures. The first is conventional lithography where the microstructure is etched into a surface via technologies such as laser interference or an electron beam. The second method is designated soft lithography and typically employs a re-usable pattern transfer element, much like a stamp. Both techniques will be discussed in turn, focussing in more detail on the soft lithographic method known as solvent assisted micromoulding (SAMiM), which was primarily used to pattern the polymer surface of the laser devices reported throughout this thesis.

4.2.1 Conventional Lithography

Electron beam lithography (EBL) is based on a similar system to scanning electron microscopes, commonly used in the microelectronics industry to pattern photomasks and is capable of producing sub-micron scale structures. An electron beam

scans across the surface of a substrate exposing an electron sensitive coating. A grid of pixels is superimposed into the surface by the computer software, which then directs the beam to realise the pattern pixel by pixel on the coating. These coatings or electron beam resists exhibit physical or chemical changes when exposed to the high-energy electron beam. Positive resists break down into less complex fragments on exposure, becoming more soluble to the developing agent than unexposed resist. Negative resists have the opposite effect, forming complex links and becoming less soluble after exposure.

The beam is generated from an electron source, which is either heated or has a field applied to produce the electrons. The beam is guided by magnetic deflection. A schematic of an EBL system is shown in figure 4.1.

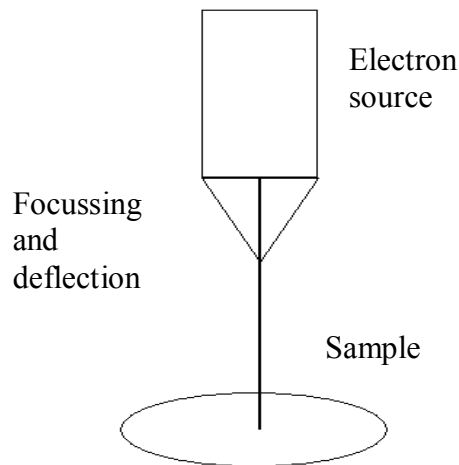


Figure 4.1: A schematic representation of an electron beam lithography system.

While the advantages of the EBL technique are the very high resolution and accurate registration of a variety of patterns, the equipment is slow and expensive. Further disadvantages include swelling when developing negative photoresists, back-

scattering of the electrons in the substrate which limit the resolution and also charging of the sample by the electrons.

An alternative method commonly used in the microfabrication of silicon wafers is photolithography. This process uses light to transfer a geometric pattern from a mask to a light-sensitive photoresist on the substrate by selectively removing parts of the film. The mask is usually patterned with the desired design through the EBL method detailed above. The sample is then exposed to ultra-violet light shone through the mask, chemically modifying the resist, which can then be removed by the developing agent in the same way as with EBL. This pattern can then be transferred into the substrate (e.g. Si or SiO₂) through wet etching using an acid such as HF or by dry etching using reactive ion etching. Photolithography is cheaper and faster than electron beam lithography but the resolution is also diffraction limited by the wavelength of the light.

An alternative way of performing photolithography is to use holography. In this case, an incoming laser beam is split into two components which subsequently overlap in the plane of the resist causing an interference pattern. The alternating regions of low and high intensity provide the patterned chemical modification of the resist such that it can be developed in the usual way. One simple technique to etch gratings in this way is to create an interference pattern in photoresist using a system based on Lloyd's mirror when incoming and reflected sources partially overlap. Changing the angle of incidence between beam and sample can adjust the period of the grating once the photoresist has been developed.

4.2.2 Soft Lithography

Industry demands ever-decreasing feature sizes to keep up with trends such as Moore's Law for packing transistors onto a single chip. As a result, a number of photolithographic (PL) techniques have been explored in order to produce feature sizes smaller than 100 nm (including extreme UV lithography, soft X-ray lithography and ion beam writing in addition to EBL, which was discussed above). The continued shrinking of feature sizes pose challenges for photolithography, which cannot always be easily adapted to low-cost applications. Photolithography also has difficulty patterning non-planar surfaces [16]. Another serious disadvantage to PL is the limited range of photoresist materials [17,18] that are compatible and provides reason for alternative lithographic methods to be pursued.

A range of such techniques, which are not limited by diffraction (due to no radiation being involved) nor hampered by set-up and maintenance costs fall under the collective term of *soft lithography* [15,19]. These techniques are named as such due to an elastomeric stamp or mould being the key element in transferring the pattern to the substrate and also due to the more general use of flexible organic materials in the fabrication process. The mould is a replica of a master structure (such as a grating fabricated through photolithography) in a flexible polymeric material. The choice of this material is highly important to the entire process, as it will form the basis of the pattern transfer to the substrate. One common polymer used to fabricate the mould is polydimethylsiloxane (PDMS) which is cheap and commercially available. PDMS is a flexible, transparent material that is chemically inert, does not stick to other substances and does not swell or react with many common solvents used in producing polymer

solutions. PDMS is a very soft polymer and prone to deformations and distortions during the transfer process [20,21] (see figure 4.2). Moulds consisting of a co-polymer blend developed by Schmid and Michel [22] have a greater rigidity and while not as flexible as PDMS, have been demonstrated to produce feature sizes at higher resolution. The work presented throughout this thesis was performed using moulds fabricated from this co-polymer blend, details of which can be found in section 3.4.3.

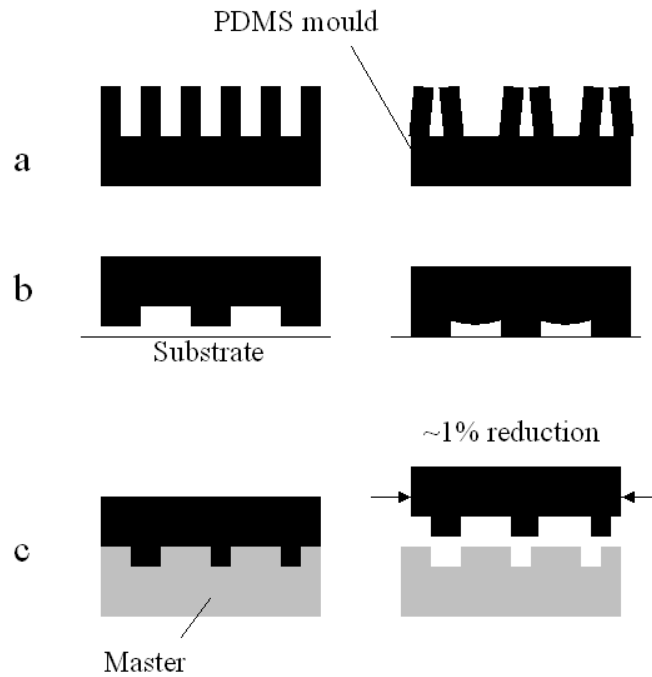


Figure 4.2: *Illustration of various deformations: a) pairing, b) sagging and c) shrinking, which affect microstructures in elastomeric moulds fabricated from polymers such as PDMS.*

In the remainder of this section, I will briefly review some of the main soft lithographic methods including microcontract printing, microtransfer moulding,

micromoulding in capillaries, hot-embossing lithography and finally, solvent assisted micromoulding.

Microcontact printing [23] is a remarkably simple, flexible process that transfers molecules from the mould to the surface of the chosen substrate by forming patterned self-assembled monolayers (SAMs) and for which exists a number of review articles [24,25]. The stamp is coated with ‘ink’ before being pressed into the surface that is to be patterned. The technique was first demonstrated for SAMs on gold [23]. The alkanethiol molecules attach to the surface via the sulphur group, leaving the rest of the molecule standing vertically out of the substrate. Varying the end group on the inking molecule can tailor the surface properties as desired. The ink could just as easily be a photoresist, which can subsequently be etched in the usual fashion. Transfer time from mould to substrate using microcontact printing varies with the solvent concentrations but is typically in the range of 10 – 20 seconds. A schematic of this technique is given in panel a, of figure 4.3.

In microtransfer moulding [26] (figure 4.3, panel b), a liquid prepolymer is applied to the patterned surface of the mould, the excess liquid being removed by scraping or by blowing in a stream of nitrogen. Heating or irradiation can then be employed to cure the polymer, after which the mould can be peeled away to leave a replica of the mould structure in the polymer. Microtransfer moulding can pattern relatively large ($\sim 3 \text{ cm}^2$) areas in a short space of time (~ 10 minutes) with reports of using this technique to pattern optical waveguides, couplers and interferometers [27].

Micromoulding in capillaries [28] (MIMIC) is another replica moulding technique that can pattern both planar and curved surfaces. The mould is placed in conformal contact with the surface to be patterned, the relief structure in the mould

forming a network of empty channels. A low viscosity liquid prepolymer is placed at the open ends of these channels, filling them through capillary action.

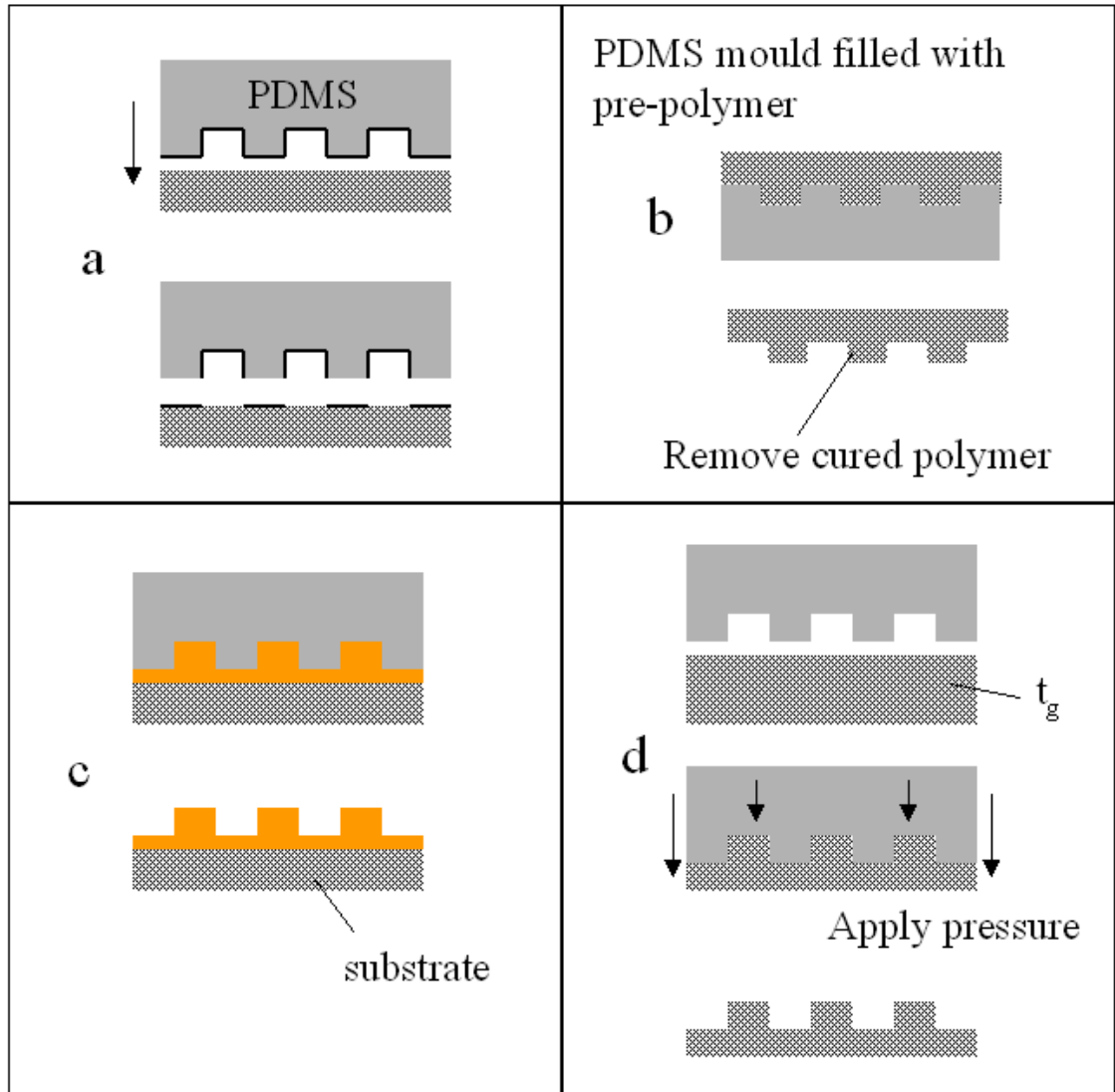


Figure 4.3: Schematic representation of the different soft lithography techniques; microcontact printing (a), microtransfer moulding (b), micromoulding in capillaries (c) and hot embossing lithography (d).

The prepolymer is then cured before the mould is carefully peeled away leaving the patterned polymer on the substrate surface. The MIMIC method is depicted in panel

c of figure 4.3. Due to the capillary mechanism required for this pattern transfer technique, MIMIC is not suitable for forming isolated structures (a connected network of capillaries are required). Additionally, viscous drag of the fluid prevents the liquid from spreading over large areas, shorter distances of ~ 1 cm is achieved quickly and efficiently.

Hot embossing lithography (HEL) is a development from injection moulding and was first demonstrated by Chou *et al.* [29] who have formed feature sizes down to 25 nm in polymethylmethacrylate (PMMA). In HEL, a master structure is brought into contact with a polymer surface (figure 4.3, panel d). The polymer is then heated above its glass transition (T_g) temperature. Under applied pressure, the polymer flows around the master structure and is forced up along the walls of the cavity slowly filling the relief structure through capillary action [30]. Once cooled, the shape of the master is effectively “frozen” in place within the polymer surface. Submerging the master in a solution of octadecyltrichlorosilane dissolved in toluene for twelve hours prevents the master sticking to the polymer upon removal by forming a hydrophobic monolayer on the surface of the master. This is essential to reduce imperfections in the transferred microstructure caused by the stress of removing the master from the polymer layer. One major drawback to using HEL is the requirement to heat the material into which the pattern will be transferred to its glass transition temperature. For conjugated polymers such as MEH-PPV or OC₁C₁₀-PPV, this is approximately 200°C and has an adverse effect on the PLQY of the material [31] thus reducing the overall effectiveness of the device. Despite these limitations, HEL has been successfully employed to modify the light-emitting properties from a thin film of semiconducting polymer improving light extraction from the device [32].

4.2.3 Solvent Assisted Micromoulding

To complete this review section, the use of a very simple, powerful technique for directly applying nanometre scale microstructure to polymer films is discussed. Solvent assisted microcontact moulding (SAMiM) [33] has many similarities with other soft lithography methods but requires no heat or pressure to operate. With SAMiM, an elastomeric mould is used as a transfer element. The mould is inked with a small amount of a suitable solvent via a Q-tip before being brought into conformal contact with the polymer surface that is to be patterned. The solvent on the surface of the element dissolves the polymer film allowing it to flow and conform to the shape of the mould structure. After a short time, the solvent evaporates and the mould is separated from the polymer film, leaving a replica of the microstructure in the surface. A schematic of this technique is depicted in figure 4.4.

It is critical to select the correct solvent for the SAMiM process. Non-polar solvents are preferred [22] due to polar solvents such as acetone or toluene causing swelling in the elastomer. This in turn causes the polymer film to stick to the mould and therefore facilitates a poor transfer of the microstructure to the polymer.

SAMiM has previously been used to directly pattern an OC₁C₁₀-PPV film with a 2D grating structure to successfully form a polymer laser [5] using PDMS as the mould material. In this work, I will demonstrate that use of this technique with moulds fabricated from a co-polymer blend [22] significantly improves the transfer depth and thus forms devices with thresholds approaching those when using the master silica gratings. A scanning electron microscope image of the surface of a co-polymer mould is shown below in figure 4.5.

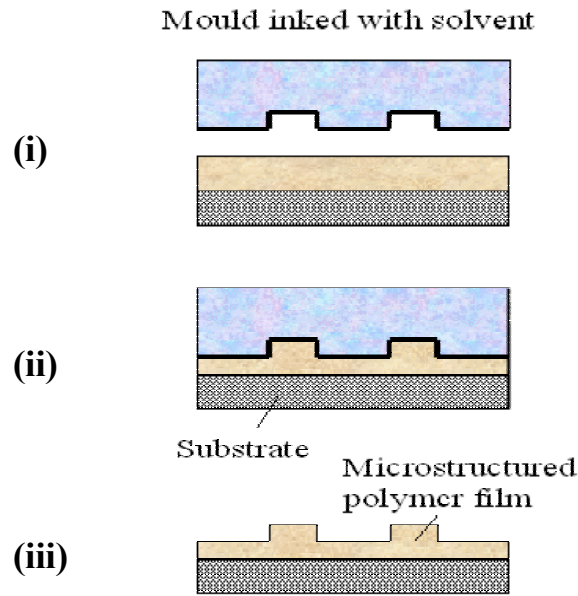


Figure 4.4: Diagram showing the method for patterning polymer films using solvent assisted micromoulding. The mould is lightly inked with an appropriate solvent using a *Q*-tip (i) before it is brought into contact with the polymer film (ii). The solvent dissolves the film allowing the polymer to conform to the shape of the grating. After a short time (typically 2 minutes), the and film are separated leaving the imprint in the polymer (iii).

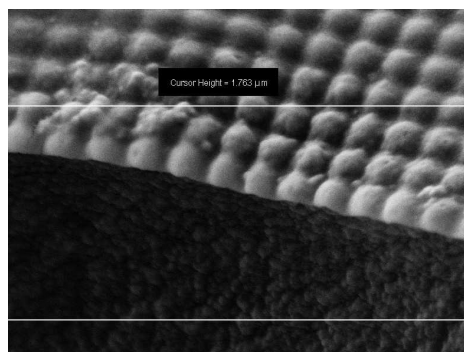


Figure 4.5: An SEM image of a co-polymer mould. The grating period is 400 nm in both directions. The grating depth was undetermined due to the inability to cleave the soft mould cleanly at a specific point.

4.3 Effect of grating depth on threshold for polymer lasers

In this section I investigate the effect that variations in grating depth has on the lasing properties of MEH-PPV DFB lasers that have been fabricated using SAMiM. In order to determine how effective SAMiM is as a tool for fabricating good quality laser devices, a comparison is made between the experimental data and what is predicted from the theory.

4.3.1 Experimental

A total of 11 devices (labelled a to k) were fabricated under identical cleanroom conditions. Thin films of MEH-PPV (5 mg / ml in chlorobenzene) were spin-coated onto pre-cleaned silica substrates (dimensions were 12 mm x 12 mm) giving films approximately 130 nm thick. The air-polymer surface was microstructured through SAMiM, transferring a 2-D ‘eggbox’ grating that had a period of ~400 nm in both directions. The depth of the structure was varied between 10 and 72 nm by changing the contact time between the mould and the film (between 5 and 180 seconds) and by subtle variations in the amount of solvent used (chlorobenzene) to ink the mould.

Films were isolated from oxygen and water by being placed in a vacuum chamber, operating at a pressure less than 10^{-4} mbar. The MEH-PPV films were pumped with the $\lambda = 532$ nm 2nd harmonic of a passively Q-switched Nd:YVO₄ microchip laser (1 ns pulse duration). The incident beam passed through an optical chopper, reducing the frequency to 80 Hz. Calibrated neutral density filters were used to attenuate the beam as necessary. Samples were mounted at a slight angle to the incoming beam path (~ 10°). Emission was collected close to normal incidence using a fibre coupled CCD spectrometer of resolution ~0.7 nm (see figure 3.6 for experimental

set-up). The gratings in the polymer film were characterised using a Vista scanning probe AFM in contact mode, supplied by Burleigh.

4.3.2 Results

The energy input/output characteristics for devices a to j are shown in figures 4.6 and 4.7 below and show a range of thresholds varying between 18 and 125 nJ / pulse. The efficiency of these devices ranged from 0.12 to 1.3% and had grating depths varying from 10 to 50 nm (summarised in table 4.1, which can be found towards the end of this discussion). The threshold values are typically an order of magnitude better than those reported for an OC₁C₁₀-PPV device (225 nJ) fabricated using SAMiM [5] and also for a BuEH-PPV laser (~130 nJ / pulse) using a microstructured substrate [4]. Device c also showed an order of magnitude increase in efficiency (1.3%) versus the OC₁C₁₀-PPV laser (0.1%). In figure 4.8, the efficiency for all eleven devices (a-k) is shown as a function of laser threshold. The general trend is for the most efficient devices to also have the lowest thresholds although there is a degree of scatter to the data.

The improvement in the emission characteristics are largely attributed to an increase in the grating depth from using a co-polymer mould compared to the softer PDMS material (which afforded a maximum transfer depth of ~20 nm). Device efficiencies were generally found to be slightly lower than the highest reported value of 6.8% for MEH-PPV using a 2-D DFB geometry [3]. If it is assumed that strong feedback and output coupling is best for the device (which may not necessarily be the case), one explanation for this is that although the refractive index contrast is greater for a grating at the air-polymer interface there is also less overlap between the feedback structures and the optical mode. A possible improvement to this experiment would be to

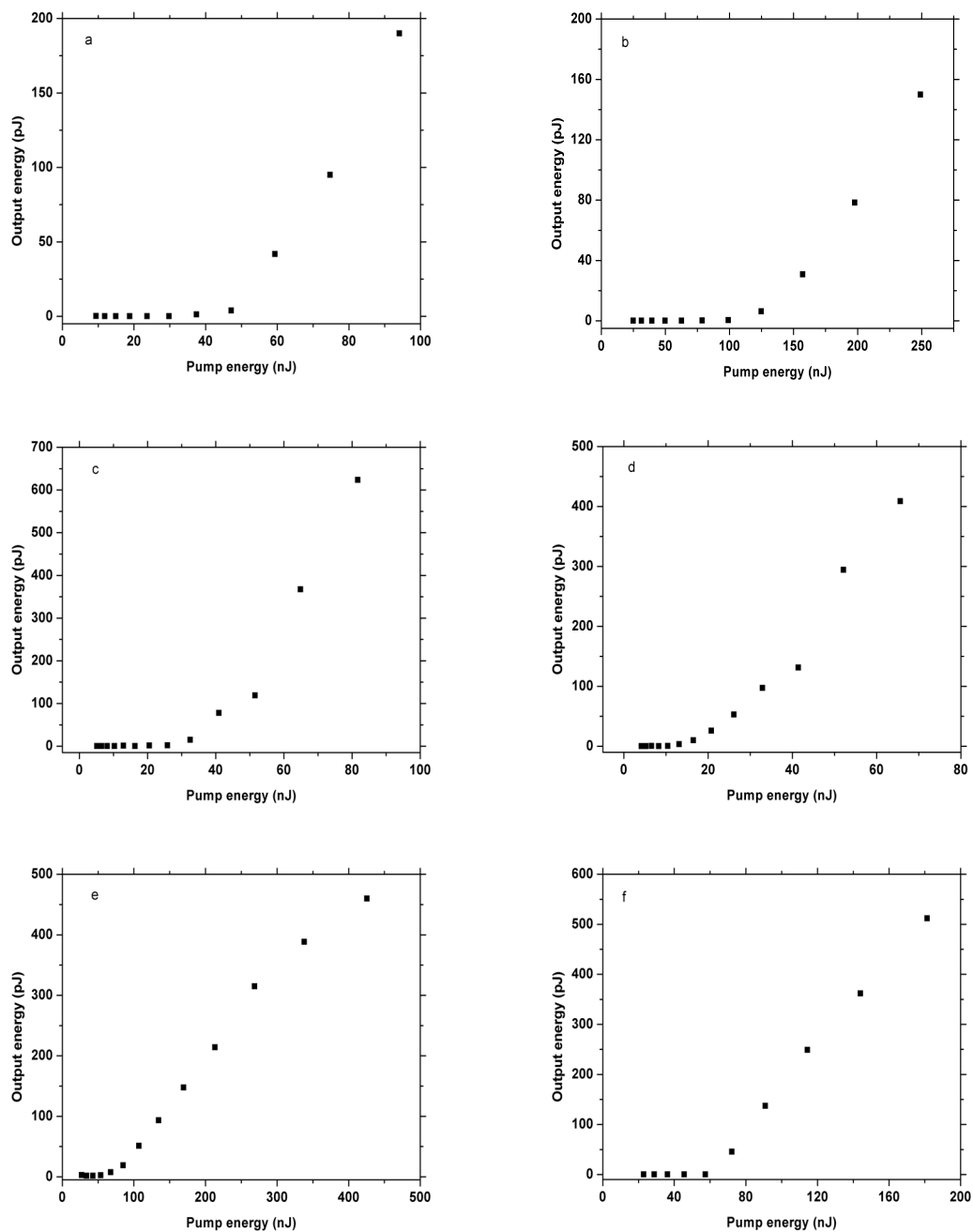


Figure 4.6: Power efficiency curves for MEH-PPV DFB lasers (devices a – f) using a two dimensional grating structure imprinted at the polymer-air interface using solvent assisted micromoulding.

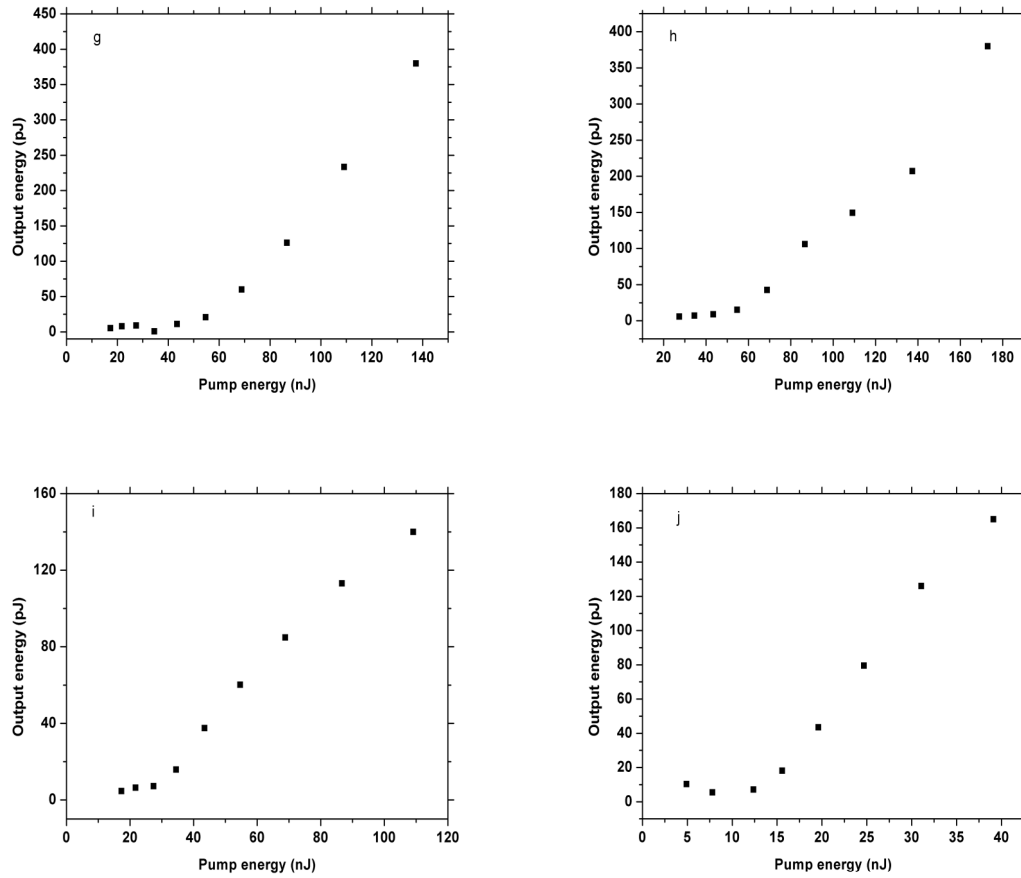


Figure 4.7: Power efficiency curves for MEH-PPV DFB lasers (device g – j) using a two dimensional grating structure imprinted at the polymer-air interface using solvent assisted micromoulding.

tailor separate gratings at the substrate-polymer and air-polymer interfaces to control the feedback and output coupling of the device independently, extracting the best possible performance from the laser.

Device k (figure 4.9) was found to have extremely good transfer of microstructure from the mould to the polymer surface with a grating depth in excess of 70 nm in places. Efficiency from this device was ~1 % and also had a low threshold of 3 nJ / pulse, two orders of magnitude better than the OC₁C₁₀-PPV device and directly

comparable with the threshold of 4 nJ from the MEH-PPV device demonstrated by Turnbull *et al.* [3].

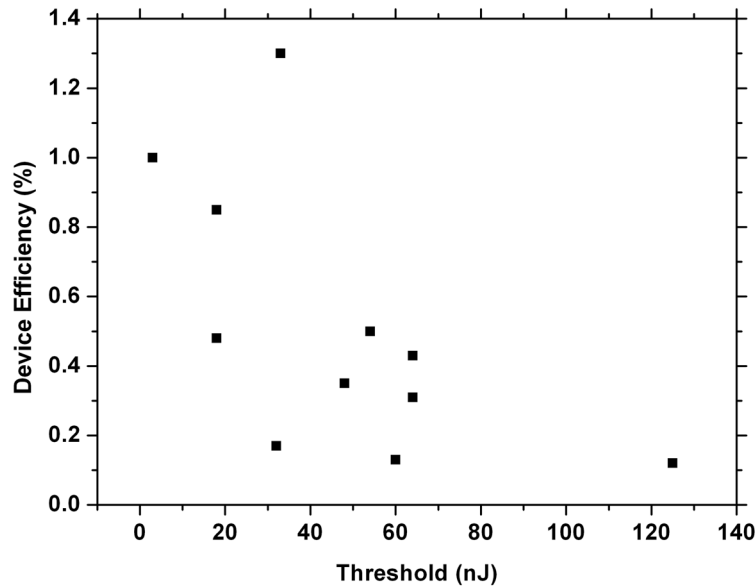


Figure 4.8: Laser efficiency as a function of threshold for devices a - k. Generally, the most efficiency devices fabricated also had the lowest thresholds.

The AFM trace in figure 4.9 is for a cross section through device k and shows a dramatically different profile and duty cycle (resembling a square grating in places) compared to the other 10 devices, which were sinusoidal (see figure 4.12) despite undergoing similar processing conditions. An explanation for this is that while the contact between the mould and the film was very good, the transfer of the microstructure to the film for device k was incomplete, possibly due to insufficient solvent to fully allow the polymer to flow into the full depth of the relief grating.

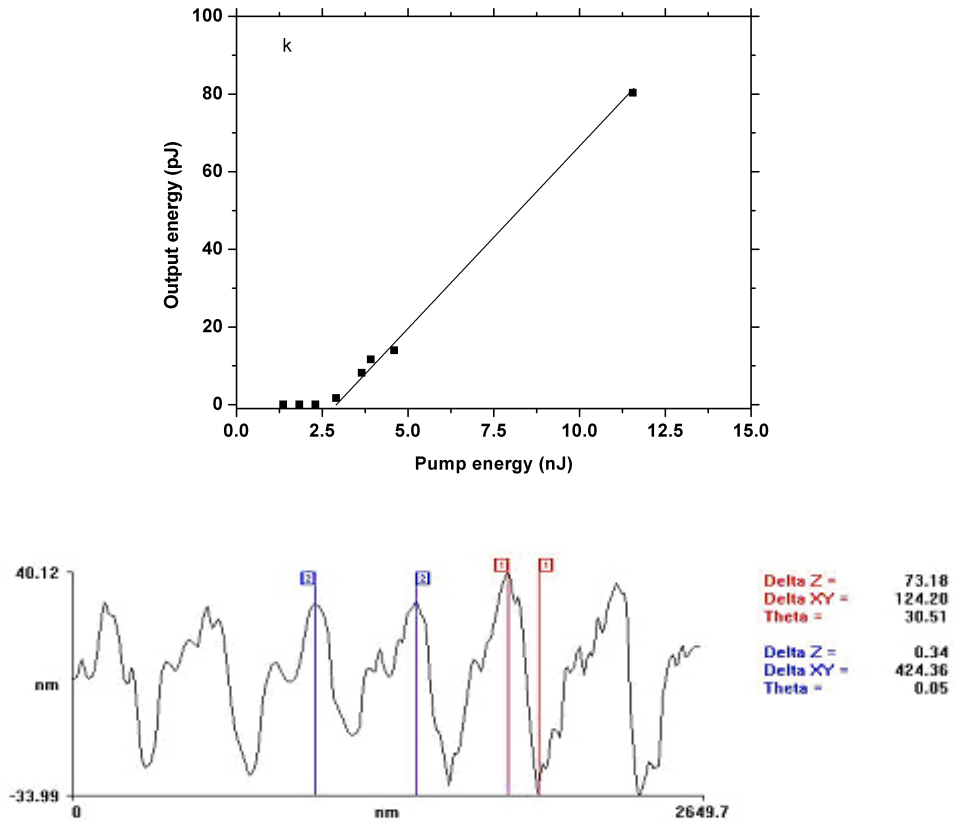


Figure 4.9: Efficiency curve (top) for device *k*. The threshold for the laser was 3 nJ/pulse. Efficiency for the device was 1 %. The lower panel contains an AFM cross-section through the grating showing the deep but irregular transfer of microstructure from the mould to the polymer film.

Thus, the polymer begins to flow up the walls of the grating cavity through capillary action [30] but does not fully fill it. This manifests in the double-humped structure evident in the cross-section, forming volcano like craters in the grating where peaks should exist. A further example of this incomplete transfer in a different device is shown in figure 4.10 below.

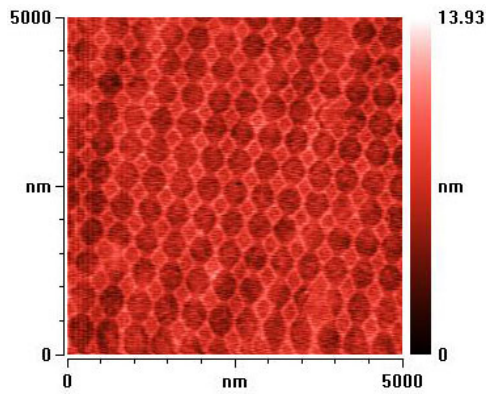


Figure 4.10: AFM surface map of a MEH-PPV film patterned by SAMiM where the grating has not fully transferred, resulting in the volcano like structure in the surface.

Achieving such low thresholds from a two dimensional DFB laser due to deep grating structure - despite an incomplete transfer does demonstrate further potential may be extracted from this geometry. Figure 4.11 shows an AFM trace for a 90 nm deep imprint in OC_1C_{10} -PPV. The ability to reproduce the quality of these gratings consistently in semiconducting polymers using soft lithographic techniques may be the key to pushing lasing threshold for DFB polymer lasers into the pico-Joule regime and beyond.

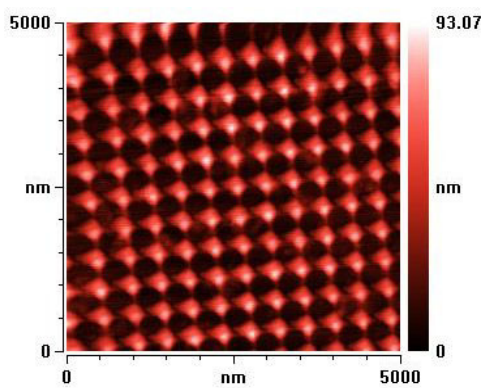


Figure 4.11: A 90 nm deep 2-D grating in an OC_1C_{10} -PPV film patterned by SAMiM.

In order to plot the threshold values for the 11 devices as a function of grating depth, the depth of each of the structures had to be established. As has already been demonstrated in figure 4.9, depending on the region of sample measured, the depth can vary by several nm and the shape of the profile may vary. Devices a-j all displayed sinusoidal behaviour for the shape of the grating and so an average depth was extracted from the AFM data by fitting a sine curve of the form:

$$y = A \sin\left(\pi \frac{x - x_c}{w}\right) \quad [4.1]$$

Here, x is the lateral offset from the centre point x_c , w is the width of one period of the oscillation and A is the amplitude of the curve. A best fit was obtained for each of the profiles by minimising the χ^2 value. The amplitude of the model fit was then recorded. An example model fit (red curve) to the AFM data (black curve) for device g (which had an amplitude of 27.5 nm implying an average depth of 55 nm) is shown below in figure 4.12.

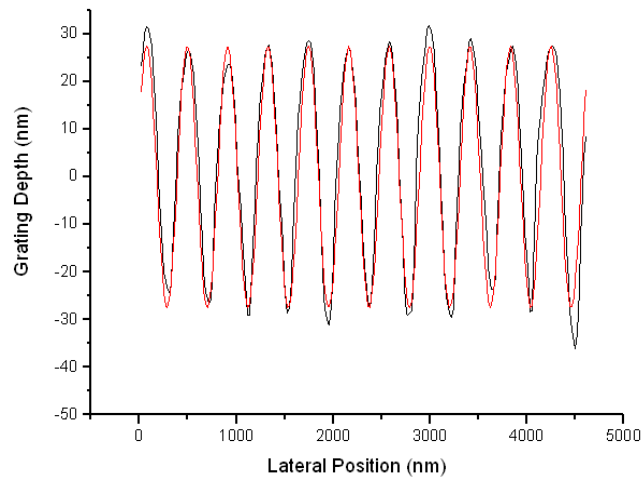


Figure 4.12: Curve fit (red line) to a sinusoidal AFM profile (black line) for device g for a minimised χ^2 value. The extracted depth for the grating was 55 nm.

A summary of the processing conditions, laser characterisation and grating data is given below in table 4.1.

Device	Processing Time (s)	Grating Depth (nm)	Threshold (nJ)	Efficiency (%)
a	5	27	48	0.35
b	15	10	125	0.12
c	30	44	33	1.3
d	180	50	18	0.85
e	60	35	60	0.13
f	180	31	64	0.43
g	180	21	54	0.5
h	180	14.5	64	0.31
i	180	55	32	0.17
j	180	48	18	0.48
k	180	72	3	1

Table 4.1: Laser threshold and efficiency data for the devices tested in this study. The processing time refers to the contact duration between the polymer film and the co-polymer mould while performing the solvent assisted micromoulding. The resulting grating depth is also shown.

The results of grating depth verses threshold for the 11 devices contained in table 4.1 are plotted in figure 4.14 below (black squares). The values have been normalised against the device with the highest threshold (device b, 125 nJ). The red data points represent values extracted from a simulation of the gain values (again normalised with respect to device b) for gratings with a perfect sinusoidal profile.

Theoretical analysis of second order gratings and surface-emitting DFB lasers has been performed previously by several authors [34-38] where forwards ($\phi(x)\exp(iK_0z)$) and backwards ($\phi(x)\exp(-iK_0z)$) propagating modes with wavevector K_0

are coupled together by second-order diffraction and also to a 90° radiating wave ($\Delta E(x,z)$) by first-order diffraction. The electric field for which is given in equation 4.2.

$$E = [A(z) \exp(iK_0 z) + B(z) \exp(-iK_0 z)] \phi(x) + \Delta E(x, z) \quad [4.2]$$

Here, $\phi(x)$ describes the transverse field and $A(z)$ and $B(z)$ are slowly varying functions of z . By considering how the dielectric function varies periodically with z (through expansion as a Fourier series) [34], a series of coupled-mode equations can be solved for the coefficients h_1 (the degree of output coupling arising from two first order diffractions) and h_2 (the level of feedback arising from a second order diffraction). The equations for these coefficients are given below.

$$h_1 = \frac{\omega^4 \Delta \epsilon^2}{4K_0 K_x c^4} \left| \int \exp(iK_x x) \phi(x) \xi_1(x) dx \right|^2 \quad [4.3]$$

$$h_2 = \frac{-\omega^2 \Delta \epsilon}{2K_0 c^2} \int \phi^2(x) \xi_2(x) dx \quad [4.4]$$

Here, ω is the angular frequency, $\Delta \epsilon$ is the change in the dielectric constant, c is the speed of light in vacuum, K_x is the wavevector for waves travelling in the x direction and ξ_i represents the i^{th} Fourier coefficient of the grating at position x within the grating layer. These coefficients are based on the fraction of the grating period occupied by the top dielectric at position x , often termed the duty cycle of the grating.

For this work, the model solves the Helmholtz equations for a slab waveguide and calculates the electric field overlap with the grating region (of depth d_g), which allows the calculation of the coupling coefficients h_1 and h_2 . Solutions to the coupled

mode equations in terms of the detuning from the Bragg wavelength (Δk) and the exponential gain coefficient of the cavity (g) give rise to equation 4.5, the reflectivity of a corrugated waveguide of length L [35,36], into which we substitute our values for h_1 and h_2 .

$$D \equiv \gamma L \cosh(\gamma L) - (g - Lh_1 + i\Delta kL) \sinh(\gamma L) = 0 \quad [4.5]$$

$$\text{where } \gamma L = \sqrt{(gL - Lh_1 + i\Delta kL)^2 - (iLh_2 - Lh_1)^2} \quad [4.6]$$

One method of extracting the poles of the reflectivity function (the longitudinal modes) is by using the Argument Principle Method (APM) [37]. The APM locates all the zeros of a given complex function within a closed contour in the complex plane. A contour map of D from equation 4.2 is plotted in the $\Delta kL / gL$ plane (figure 4.13); where D goes to zero for each device yields the value the gain parameter g and its corresponding Δk .

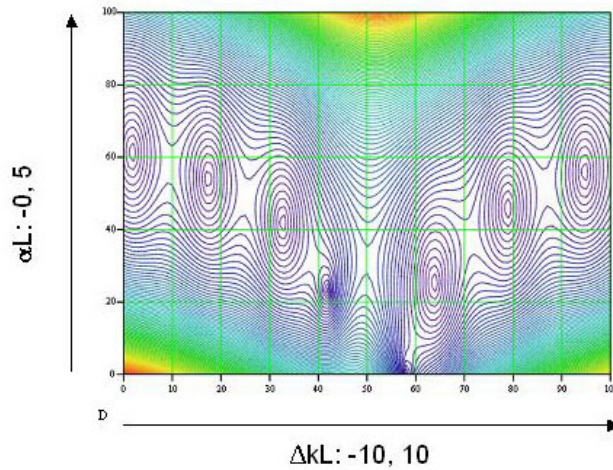


Figure 4.13: Contour map of D in the $\Delta kL : gL$ plane showing the solutions to equation 4.2 using the APM.

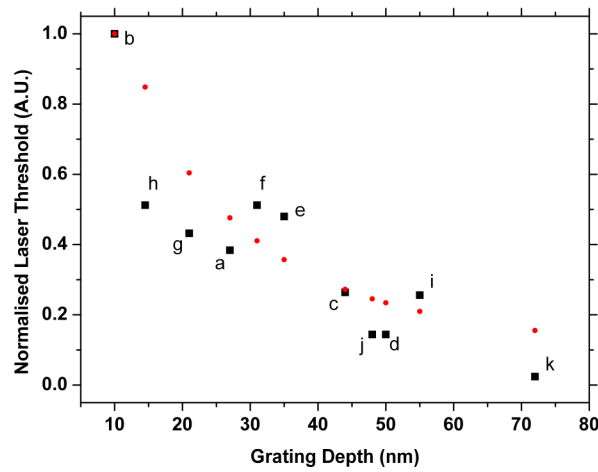


Figure 4.14: Normalised values of laser threshold for devices a-k as a function of the grating depth (black squares). The red data points represent the theoretical values for sinusoidal gratings from the model analysis, again normalised with respect to device b.

There is general agreement between the experimental data and the theoretical values over the range of grating depths tested (figure 4.14). The scatter in the experimental data compared to the predicted values is most likely due to small variations in the grating depth and grating shape over the pumped region. The threshold value for device k (72 nm depth) shows a greater variation from the theory than the other lasers. Device k has already been shown to have a substantially different grating shape to that of a sinusoid (as per the modelling), which is this most likely candidate for the observed differences. In conclusion, while exact control over the depth and shape of the grating structures may be slightly beyond the scope of solvent assisted micromoulding, the above work demonstrates that low threshold polymer DFB lasers can be fabricated quickly and simply and that their behaviour is very similar to what is predicted from the theory.

4.4 Application of soft lithography for novel device fabrication

4.4.1 Circular Distributed Feedback Lasers

We have seen that distributed feedback lasers are particularly promising resonators for achieving low oscillator thresholds in a compact geometry. The lowering of laser thresholds in devices fabricated from semiconducting polymers is a key goal in the drive towards electrical pumping. One area of interest is the study of applying feedback in more than one direction in the plane of the active material and there have been several demonstrations [2,39-40] of the significant improvements going from a one-dimensional structure to the two-dimensional structures, such as those reported in the previous section of this chapter.

An obvious extension to the 2D grating would be to apply feedback in all directions within the plane, an idea possible by using circular distributed feedback (CDFB) gratings. This geometry was proposed by Erdogan and Hall [41] and later demonstrated by Wu *et al.* in a GaInAsP/InP gain medium [42]. Semiconducting polymer CDFBs have been demonstrated both by Bauer *et al.* who observed lasing in one photon [10] and two photon [43] absorption and also by Turnbull *et al.* who have studied the influence of the grating characteristics on the lasing output [11] and the effects of gain localisation within the feedback structure [12].

The previous reports have all based their devices on a microstructured substrate, before applying the gain medium. In this section, I will demonstrate the successful

pattern transfer of a circular grating to a polymer film using solvent assisted micromoulding and characterise the subsequent laser emission from the device.

The grating pattern was initially defined by electron beam lithography using a Leica EBPG-5 Beamwriter at the University of Glasgow in a poly(methyl-methacrylate) resist layer on top of a silica substrate and comprises square-wave concentric circular trenches with period Λ , depth d and duty cycle Γ . A 30 nm layer of NiCr was used as a charge-dissipation layer and removed prior to etching. The pattern was transferred to the substrate via reactive ion etching using fluorine chemistry (CHF_3) and had a radial period of 400 nm and a depth of approximately 125 nm. The duty cycle measures the trench width to period ratio. A schematic of the grating structure is shown below in figure 4.15. For this study, the duty cycle was 25 % with the inner and outer diameter being 300 nm and 300 μm respectively.

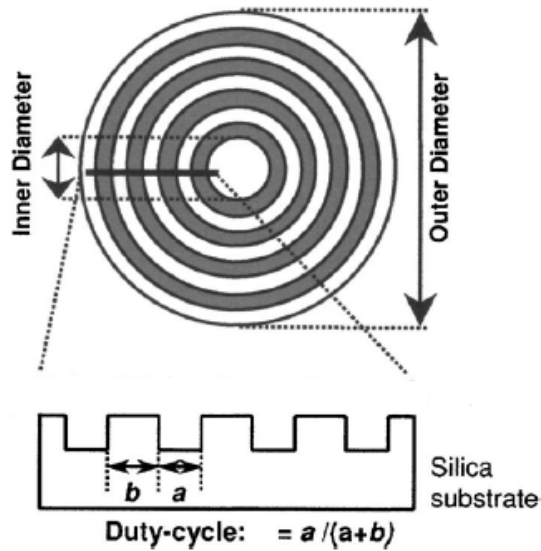


Figure 4.15: Schematic of the general structure of the CDFB grating including the plan view and a cross section through the grating demonstrating the duty cycle. Figure modified from [11].

To fabricate the laser structure, a thin film of the polymer MEH-PPV was spin-coated from solution (chlorobenzene, concentration = 5 mg / ml) onto a planar silica substrate of dimensions 12 mm x 12 mm forming a film thickness of ~ 120 nm. The master grating was replicated using a co-polymer mould (see section 3.4.3 for preparation). Transfer of the microstructure was through solvent assisted micromoulding (transfer time = 180 seconds). Immediately after fabrication, the sample was transferred to a vacuum chamber at a pressure of less than 10^{-4} mbar to isolate it from air and water during characterisation.

For lasing measurements, the sample was excited using the second harmonic of a passively Q-switched Nd:YVO₄ microchip laser ($\lambda = 532$ nm, 1 ns pulse duration, 80 Hz). The output was focussed to a circular spot of ~ 6 μ m radius incident upon the polymer film. Excitation energy was varied through the use of calibrated neutral density filters. Output emission was collected close to normal incidence using a fibre coupled CCD spectrometer. Grating structures were characterised by using a Vista scanning probe AFM, supplied by Burleigh.

In figure 4.16 below, the topography of the circular grating in the MEH-PPV film is shown for a region covering 30 x 30 μ m, centred on the middle of the microstructure. The 3D plot is centred on the 10 x 10 μ m region surrounding the central feature. Both images show effective transfer of the circular pattern to the polymer film. Also of note are the small defects in the image, which are attributed to dust particles. These manifest themselves as spikes in the z-height during the AFM scan. While the 2D eggbox gratings are fairly robust and unaffected by particles such as dust due the large surface coverage ($\sim \text{cm}^2$) of the grating, foreign bodies which could act as unwanted scattering centres for an incident beam must be kept clear from these small grating areas

(outer radius of 300 μm). The bottom panel of figure 4.16 shows a cross section taken through the grating profile highlighting the approximate period and depth of the structure. Maximum grating depth is 46 nm, which is approaching 40% of the master grating depth (~ 125 nm). It is expected that a fraction of the depth is lost when creating the co-polymer mould and the rest during the SAMiM process. In order to establish these values, a clear image of the co-polymer mould would be required, which was found to be too soft to obtain an AFM image.

Figure 4.17 demonstrates the typical spectral (top) and power (bottom) characteristics of the SAMiM circular grating. The emission wavelength was $\lambda = 625$ nm. The threshold and efficiency values were 37 nJ / pulse and 0.2% respectively. These values are very similar to those reported by Turnbull *et al.* [11] (19 nJ and 0.13%) for a CDFB device with the grating at the substrate/polymer interface demonstrating that once a replica of the master has been created in co-polymer, the potential of the SAMiM device is very similar to devices using a corrugated substrate. It is likely that the threshold value for the SAMiM laser is slightly higher due to the shallower grating depth transferred to the film (46 nm here compared to an effective depth of 80+ nm). The values are also larger than the best reported 2D DFB device reported in this chapter (which had a 3 nJ threshold), this is attributed to the differences between the grating profiles – the circular grating being designed to minimize surface output-coupling losses.

It is expected that significant improvements to the output from CDFB lasers fabricated through soft lithography will occur with deeper grating transfer. Additionally, mimicking the grating design of the 2D corrugation (which is a sinusoidal profile) may also offer improvements to the device performance. In conclusion, the CDFB lasers

characterised in this section have demonstrated very similar performance to those using patterned silica but with the benefit of much simpler fabrication as a result of using SAMiM.

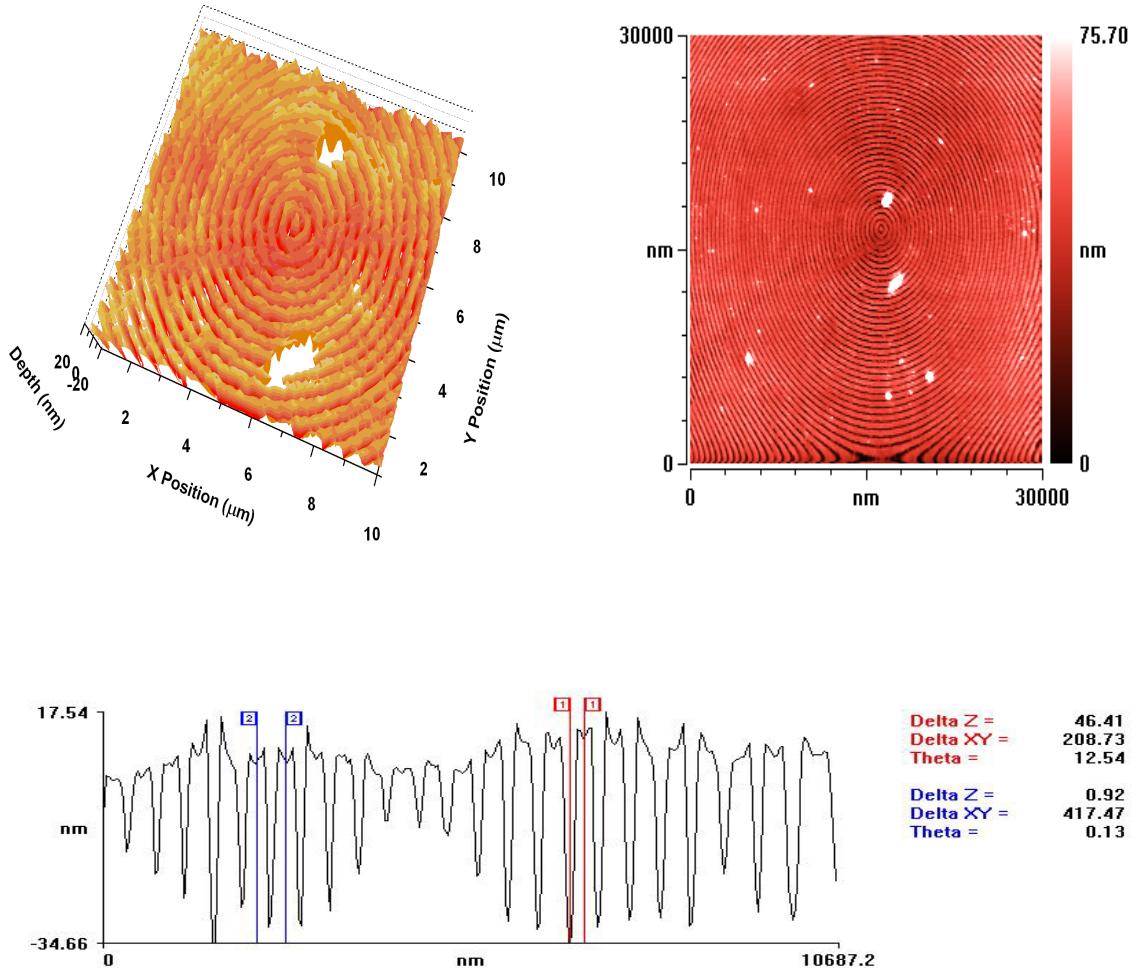


Figure 4.16: Surface map covering a $30 \times 30 \mu\text{m}$ area (top right) of a 400 nm period circular grating structure imprinted into MEH-PPV by use of SAMiM. The top left panel is a 3-D map of the central $10 \mu\text{m}$ region of the same device. In both images, intermittent damage to the surface is evident. The bottom profile shows a slice through a $10 \mu\text{m}$ cross section of the grating showing a maximum depth transfer of 46 nm, but also inconsistencies in the average depth.

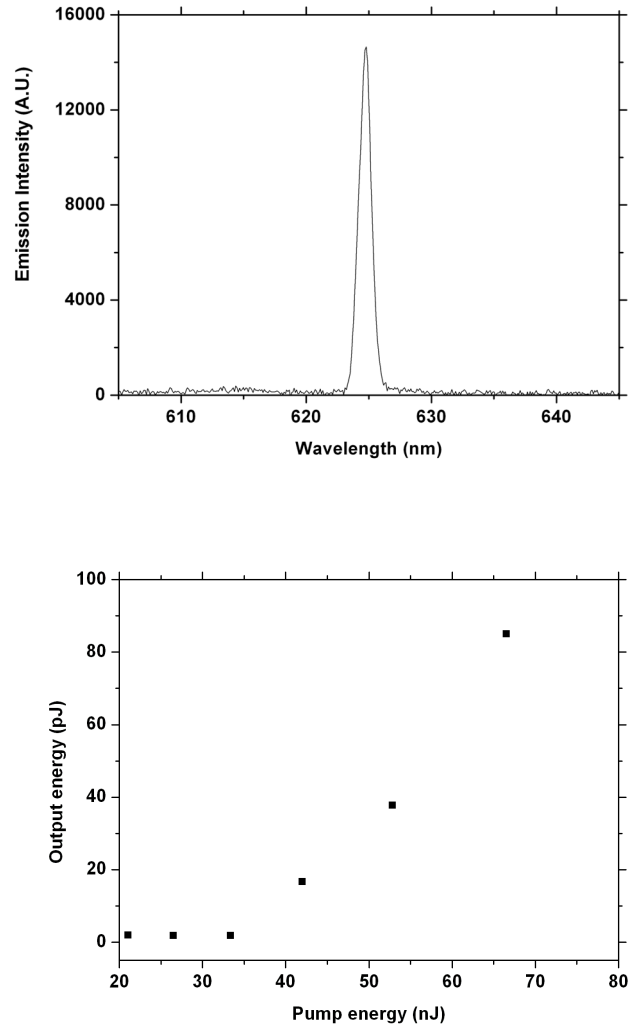


Figure 4.17: Spectral profile (top) for a polymer CDFB laser fabricated using SAMiM, operating above threshold. The linewidth is limited by the resolution of the spectrometer (~ 0.6 nm). The power characteristics (bottom) give a slope efficiency of 0.2% and a threshold value of 37 nJ / pulse, comparable to the MEH-PPV device fabricated by Turnbull et al. which had the corrugation at the substrate/polymer interface.

4.4.2 Flexible Polymer Lasers

One of the attractive properties of semiconducting polymers is the ease of which they process from solution, which opens up applications such as ink-jet printing. It is easy to imagine the benefits of mass fabricating organic semiconductor devices at an industrial level, where the polymer is sprayed onto a flexible substrate, which is housed on a roller. Previous demonstrations of LEDs [44], transistors [45,46] and organic solid state lasers [47,48] on flexible substrates have paved the way for increased effort in furthering fabrication techniques and the materials involved. As well as the obvious industrial benefits, flexible devices are inherently more robust than devices fabricated using brittle silica substrates, which also have obvious limitations when being applied to applications with curved surfaces. In this section, I use SAMiM to pattern a polymer film, which has been spin-coated onto a flexible substrate. Configured as a DFB laser, I compare the output characteristics for the device to the polymer lasers using silica substrates. The remarkably simple fabrication process is promising for development of cheap flexible polymer lasers.

Previous work by Berggren *et al.* [47] reported a flexible DFB laser device, formed by imprinting a heated benzocyclobutene (BCB) substrate with a mould. After removing the mould, the BCB was then photopolymerized under exposure to UV. This formed a 600 nm grating onto which a thin film of DCM doped 8-hydroxyquinolino aluminium (Alq) was deposited. Here, I directly spin-coat a layer of the polymer MEH-PPV (5 mg / ml in chlorobenzene) onto a modified flexible substrate and apply microstructure to the air-polymer surface through SAMiM. The resulting laser emission is then characterised using an identical set-up to the one described in section 4.3.1.

Additionally, I show that the option exists to create microstructure in the substrate itself using hot-embossing lithography, details of which are contained within the review at the beginning of this chapter.

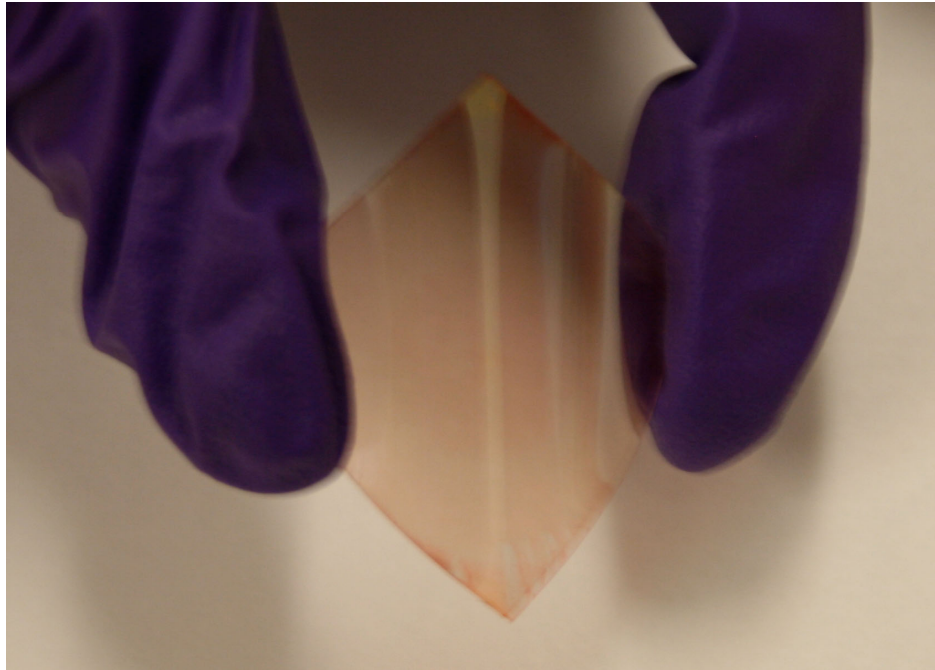


Figure 4.18: *Photograph of a flexible polymer laser. The device structure consists of a layer of N68 optical adhesive spin-coated onto a PEN substrate. A thin film of MEH-PPV is then coated onto the adhesive.*

The substrate material used was Teonex® poly(ethylene-2,6-naphthalate) (PEN) films supplied by Dupont. The PEN film thickness was approximately 125 μm and can be likened to a sheet of acetate. The absorption spectrum for a blank sheet of PEN is given below in figure 4.19 and shows that it is optically transparent for the absorption and emission wavelength range for MEH-PPV. The substrate is also smooth as can be seen from the AFM surface profile and cross section, also in figure 4.19 (mean square variation < 2 nm and maximum peak to trough variations < 10 nm). As a result, an even polymer film is formed during spin-coating.

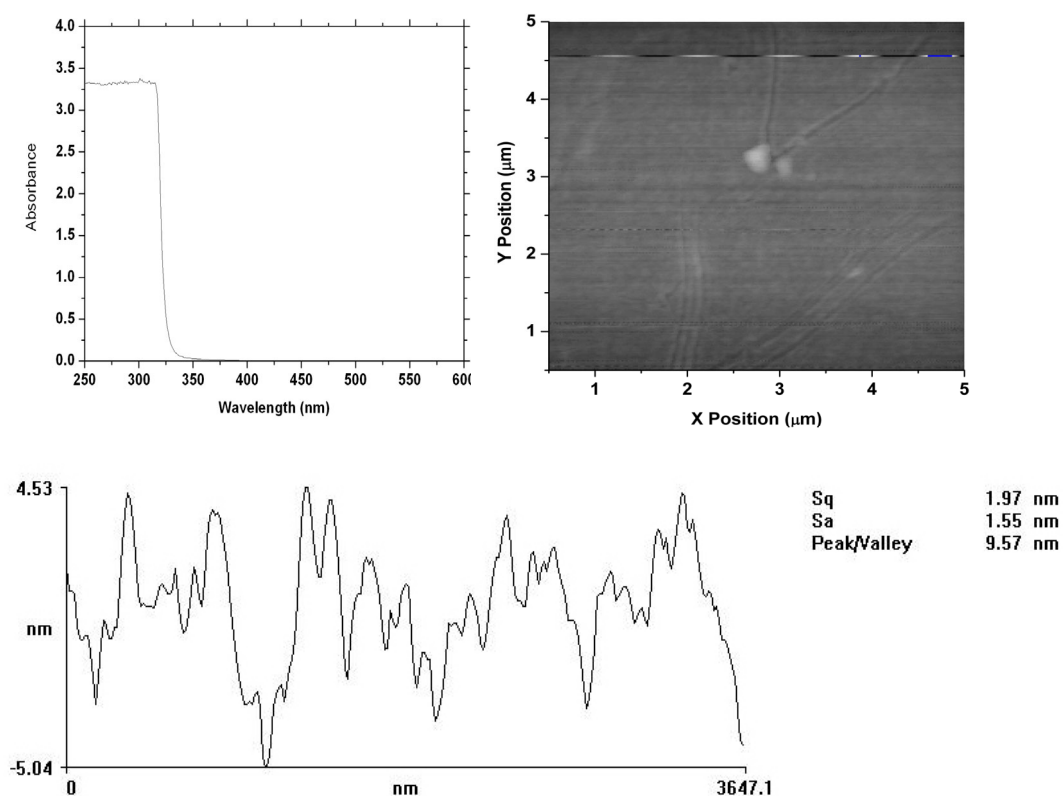


Figure 4.19: Demonstration of material properties for a PEN film including the absorption spectrum (top left) and AFM surface map (top right) with cross section.

The ability to flex and bend the PEN substrates presented here should make them ideally suited to several forms of soft lithography which require conformal contact to be successfully. To demonstrate this, hot embossing lithography [29] was used to pattern a flexible PEN film. The PEN was cleaned using ultrasound in a bath of acetone before the process was repeated using isopropanol. A mixture of sulphuric acid and hydrogen peroxide (see section 3.4.3) was used to clean the master grating, which was formed in silica through holography. The master was then left in a mixture of toluene and octadecyltrichlorosilane for 12 hours. This formed a hydrophobic monolayer on the surface of the grating through self-assembly and prevents the grating sticking to the target material during the embossing.

The PEN film was placed onto the microstructured surface of the master grating before being heated above its glass transition temperature (approximately 120°C) under normal laboratory conditions. Pressure ($\sim 50 \text{ N/cm}^2$) was applied to the process through the use of weights placed on top of the film. After 30 minutes had passed, the heating was switched off. The PEN film and the master grating were allowed to cool before being carefully separated.

The result of the imprint is shown through an AFM surface map in figure 4.20. A replica of the 2-D profile from the master grating is clearly visible in the PEN surface. A cross section of the grating shows a period of $\sim 400 \text{ nm}$ (the same as the master) and a depth varying between 32 and 38 nm, similar values to grating depths in polycarbonate using HEL [31].

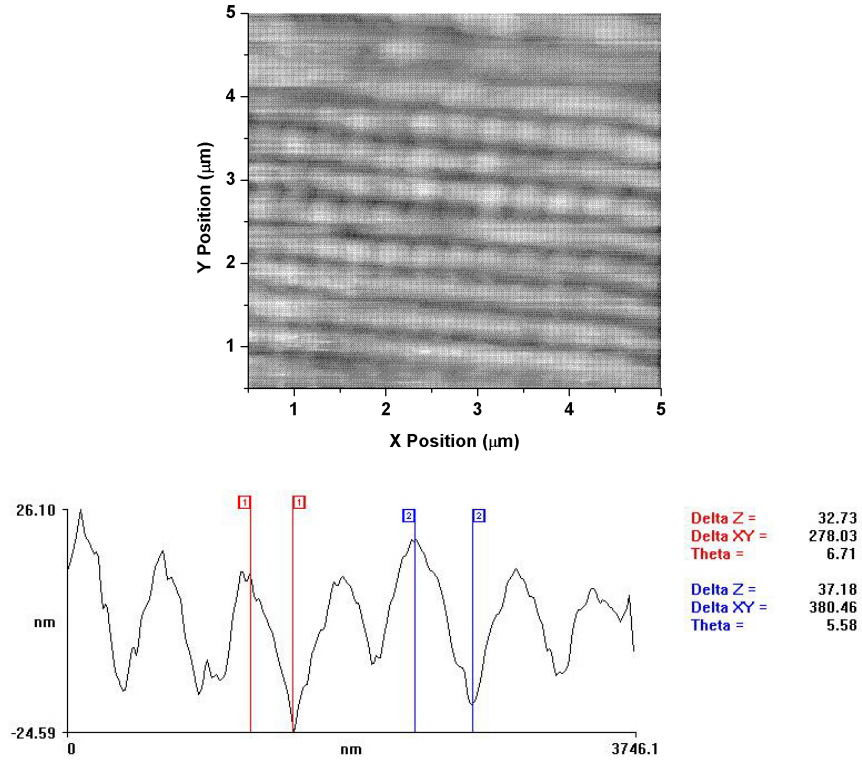


Figure 4.20: AFM image and cross section of a microstructured PEN substrate using HEL. The period of the grating is ~ 400 nm in both directions and has a depth varying between 32 and 38 nm.

Although it is clearly shown that HEL can be used as a tool to transfer microstructure to PEN flexible substrates, DFB laser devices were not fabricated in this geometry. The reason for this is PEN possesses an index of refraction ($n_x \approx n_y = 1.75$ [49]) much higher than that of silica. As a result, the range of emission wavelengths for this waveguide configuration (consisting air, MEH-PPV ($n \approx 1.88$ at $\lambda = 630$ nm) and the PEN substrate) with a corrugation period of 400 nm are too red-shifted to be supported by the polymer. To combat this, one can either change the corrugation period being used to microstructure the film or by creating a larger index contrast at the substrate – polymer interface. In this work, I pursued the latter option.

Various materials were tested as spacer layers between the substrate and the MEH-PPV film. Materials such as Cytop® ($n = 1.34$) [50] were found to act like Teflon making further layer deposition impossible while the photoresist S1818 reacted with the chlorobenzene solvent seconds after contact, forming an opaque film. The optical adhesive Norland 68 ($n = 1.58$) behaved in a similar fashion to the Cytop® but formed a more consistent film during spin coating. It has been shown [51] that the use of an oxygen plasma asher can dramatically change the surface adhesion properties of non-stick polymers such as PTFE. By plasma ashing a PEN flexible substrate coated with a layer of N68 for 5 seconds, subsequent films of MEH-PPV could be spin-coated onto the spacer layer with ease. The surface topography of the N68 film before and after plasma ashing is shown below in figure 4.21.

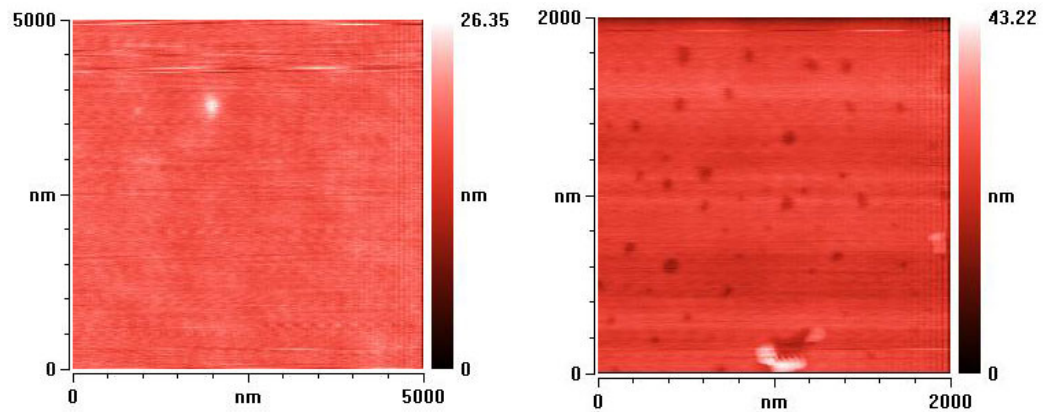


Figure 4.21: *AFM surface maps for a film of N68 adhesive before (left) and after (right) a 5 second exposure to an oxygen plasma asher. The change in the quality of the film is clearly evident and may be a contributing factor to the slightly reduced values of threshold and efficiency for the flexible laser when compared to the devices in section 4.3.2.*

The laser characteristics for a PEN / N68 / MEH-PPV device, microstructured with a 2-D 400 nm grating through SAMiM are given below in figure 4.22. The left panel shows the broad PL emission for a device below threshold. Above threshold, line narrowing occurs at a wavelength of 631 nm. The lasing threshold for the device (right panel) is 245 nJ/pulse and has a slope efficiency of 0.1%. Both values are around an order of magnitude below the performance of the devices fabricated using a silica substrate in section 4.3.2 earlier in this chapter. This is likely to be the result of the requirement for a spacer layer and the plasma ashing process. Performance for these flexible polymer lasers can almost certainly be improved either by using a substrate with a lower refractive index – which would simplify fabrication or through spacer materials with better adhesion properties.

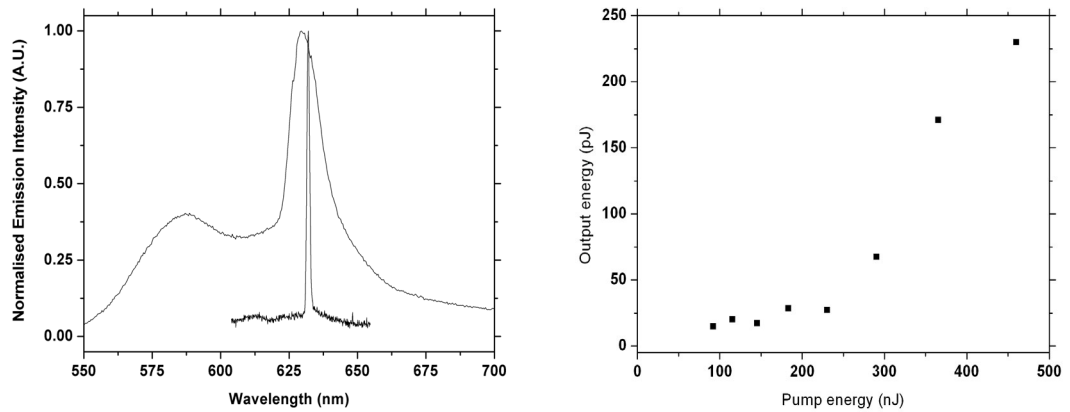


Figure 4.22: Spectral output of the flexible polymer laser above and below threshold (left). The power characteristics (right) yield a threshold value of 245 nJ and an efficiency of 0.1%.

4.5 Summary

In this chapter, a particular soft lithographic technique: solvent assisted micromoulding, was used to pattern thin films of the polymer MEH-PPV with wavelength scale microstructure. A range of polymer DFB lasers with different resonator geometries (square lattice, circular), grating depths and substrate types (silica, flexible PEN) were presented.

Comparisons were made to previous work involving MEH-PPV lasers where the grating was positioned at the substrate-polymer interface. The laser devices tested here were observed to perform with similar characteristics as those using pre-etched silica substrates with the advantage of far simplified processing. An increase in grating depth during the fabrication process led to a polymer laser with a threshold of 3 nJ and a slope efficiency of 1%, a marked improvement over previous reported results for a MEH-PPV laser which was fabricated using the same method. A range of devices with varying grating depth was tested for laser threshold. While inconsistencies in the grating depth and in the sinusoidal grating profile were observed, the devices were found to behave as predicted from the theory.

Solvent assisted micromoulding was then used to microstructure the polymer film directly with a circular grating demonstrating the flexibility of the technique in applying non-standard patterns. The resulting device had a threshold of 37 nJ and an efficiency of 0.2%, again very similar to results reported for the same material on an etched silica substrate.

Finally, SAMiM was applied to a MEH-PPV film spin-coated onto a flexible PEN substrate. Optical adhesive was used as a spacer layer to adjust the refractive index contrast so that laser operation was permitted. The resulting threshold was 245 nJ and the laser had an efficiency of 0.1%. These values are expected to improve by optimising the materials used in the construction of the device. Flexible electronics are set to play a very important part in future developments. The ease in the processing and fabrication of a working flexible polymer laser demonstrates the potential of both conjugated polymeric materials and solvent assisted micromoulding as a means for applying diffractive resonator structures for future applications.

4.6 References

- [1] H. Kogelnik and C.V. Shank, *Applied Physics Letters*, **18**, 152 (1971).
- [2] S. Riechel, C. Kallinger, U. Lemmer, J. Feldmann, A. Gombert, V. Wittwer and U. Scherf, *Applied Physics Letters*, **77**, 2310 (2000).
- [3] G.A. Turnbull, P. Andrew, W.L. Barnes and I.D.W. Samuel, *Applied Physics Letters*, **82**, 313 (2003).
- [4] M.D. McGehee, M.A. Diaz-Garcia, F. Hide, R. Gupta, E.K. Miller, D. Moses and A.J. Heeger, *Applied Physics Letters*, **72**, 1536 (1998).
- [5] J.R. Lawrence, G.A. Turnbull and I.D.W. Samuel, *Applied Physics Letters*, **82**, 4023 (2003).
- [6] A.E. Vasdekis, G.A. Turnbull, I.D.W. Samuel, P. Andrew and W.L. Barnes, *Applied Physics Letters*, **86** (2005).
- [7] K. Forberich, M. Diem, J. Crewett, U. Lemmer, A. Gombert and K. Busch, *Applied Physics B – Lasers and Optics*, **82**, 539 (2006).
- [8] A. Dodabalapur, M. Berggren, R.E. Slusher, A. Timko and O. Nalamasu, *Applied Physics Letters*, **72**, 410 (1998).
- [9] M. Notomi, H. Suzuki and T. Tamamura, *Applied Physics Letters*, **78**, 1325 (2001).
- [10] C. Bauer, H. Giessen, B. Schnabel, E.B. Kley, C. Schmitt, U. Scherf and R.F. Mahrt, *Advanced Materials*, **13**, 1161 (2001).
- [11] G.A. Turnbull, A. Carleton, G.F. Barlow, A. Tahraoui, T.F. Krauss, A.K. Shore and I.D.W. Samuel, *Journal of Applied Physics*, **98** (2005).

- [12] G.A. Turnbull, A. Carleton, A. Tahraoui, T.F. Krauss, I.D.W. Samuel, G.F. Barlow and A.K. Shore, *Applied Physics Letters*, **87** (2005).
- [13] R.C. Polson, M.E. Raikh and Z.V. Vardeny, *Advanced Materials*, **13**, 760 (2001).
- [14] F. Quochi, F. Cordella, A. Mura, G. Bongiovanni, F. Balzer and H.G. Rubahn, *Applied Physics Letters*, **88** (2006).
- [15] Y. Xia and G.M. Whitesides, *Angew. Chem. Int. Ed.*, **37**, 550 (1998).
- [16] W.D. Deninger and C.E. Garner, *The Journal of Vacuum Science and Technology B*, **6**, 337 (1988).
- [17] R.D. Miller and G.M. Wallraff, *Advanced Materials for Optics and Electronics*, **4**, 95 (1994).
- [18] A. Reiser, H.-Y. Shih, T.-F. Yeh and J.-P. Huang, *Angew.Chem. Int. Ed.*, **35**, 2428 (1996).
- [19] X.-M. Zhao, Y. Xia and G.M. Whitesides, *Journal of Material Chemistry*, **7**, 1069 (1997).
- [20] T. Tanaka, M. Norigama and N. Atoda, *Japanese Journal of Applied Physics*, **32**, 6059 (1993).
- [21] E. Delamarche, H. Schmid, H.A. Biebuyck and B. Michel, *Advanced Materials*, **9**, 741 (1977).
- [22] H. Schmid and B. Michel, *Macromolecules*, **33**, 3042, (2000).
- [23] A. Kumar and G.M. Whitesides, *Applied Physics Letters*, **63**, 2002 (1993).
- [24] J.L. Wilbur, A. Kumar, H.A. Biebuyck, E. Kim and G.M. Whitesides, *Nanotechnology*, **7**, 452 (1996).

- [25] Y. Xia, X.-M. Zhao and G.M. Whitesides, *Microelectronic Engineering*, **32**, 255 (1996).
- [26] X.-M. Zhao, Y. Xia and G.M. Whitesides, *Advanced Materials*, **8**, 837 (1996).
- [27] X.-M. Zhao, S.P. Smith, S.J. Waldman, G.M. Whitesides and M. Prentiss, *Applied Physics Letters*, **71**, 1017 (1997).
- [28] E. Kim, Y. Xia and G.M. Whitesides, *Nature*, **376**, 581 (1995).
- [29] S.Y. Chou, P.R. Krauss and P.J. Renstrom, *Applied Physics Letters*, **67**, 3114 (1995).
- [30] L.J. Heyderman, H. Schiff, C. David, J. Gobrecht and T. Schweizer, *Microelectronic Engineering*, **54**, 229 (2000).
- [31] J. Lawrence, *Organic Semiconductors: Optical Amplification, Lasing and Soft Lithography*, PhD Thesis, University of St.Andrews (2003).
- [32] J. Lawrence, P. Andrew, W.L. Barnes, M. Buck, G.A. Turnbull and I.D.W. Samuel, *Applied Physics Letters*, **81**, 1955 (2002).
- [33] E. Kim, Y. Xia, X.-M. Zhao and G.M. Whitesides, *Advanced Materials*, **9**, 651 (1997).
- [34] R.F. Kazarinov and C.H. Henry, *IEEE Journal of Quantum Electronics*, **21**, 144 (1985).
- [35] A. Hardy, D.F. Welch and W. Streifer, *IEEE Journal of Quantum Electronics*, **25**, 2096 (1989).
- [36] D. Park and M. Kim, *IEEE Journal of Quantum Electronics*, **32**, 1432 (1996)
- [37] G.F. Barlow and K.A. Shore, *International Journal of Numerical Modelling-Electronic Networks, Devices and Fields*, **14**, 291 (2001).

- [38] G.F. Barlow and K.A. Shore, *IEE proceedings – Optoelectronics*, **146**, 15 (1999).
- [39] G. Heliotis, R. Xia, G.A. Turnbull, P. Andrew, W.L. Barnes, I.D.W. Samuel and D.D.C. Bradley, *Advanced Functional Material*, **14**, 91 (2004).
- [40] J. Stehr et al, *Advanced Materials*, **15**, 1726 (2003).
- [41] T. Erdogan and D.G. Hall, *Journal of Applied Physics*, **68**, 1435 (1990).
- [42] C. Wu, M. Silvans, M. Fallahi, T. Makino, J. Glinski, C. Maritan and C. Blaauw, *Electronics Letters*, **27**, 1819 (1991).
- [43] C. Bauer, B. Schnabel, E.B. Kley, U. Scherf, H. Giessen, and R.F. Mahrt, *Advanced Materials*, **14**, 673 (2002).
- [44] G. Gustafsson, Y. Cao, G.M. Treacy, F. Klavetter, N. Colaneri and A.J. Heeger, *Nature*, **357**, 477 (1992).
- [45] F. Garnier, R. Hajlaoui, A. Yassar and P. Srivastava, *Science*, **265**, 1684 (1994).
- [46] Z. Bao, Y. Feng, A. Dodabalapur, V.R. Raju and A.J. Lovinger, *Chemistry of Materials*, **9**, 1299 (1997).
- [47] M. Berggren, A. Dodabalapur, Z. Bao and R.E. Slusher, *Advanced Materials*, **9**, 968 (1997).
- [48] M. Berggren, A. Dodabalapur, R.E. Slusher, A. Timko and O. Nalamasu, *Applied Physics Letters*, **72**, 410 (1998).
- [49] MSDS, Technical data sheet, Teijin DuPont films.
- [50] Bellex International Corporation.
- [51] C.-L. Li, C.-Y. Tu, J.-S. Huang, Y.-L. Liu, K.-R. Lee and J.-Y. Lai, *Surface Coatings and Technology*, 201, 63 (2006).

Chapter 5: Encapsulated Polymer Lasers

5.1 Introduction

The previous chapter demonstrated how incorporating wavelength scale microstructure into optical materials is a powerful tool for manipulating and controlling the output of light from a device. What makes polymeric DFB lasers attractive is the ease of fabrication from solution and their low cost. One present limitation of such devices however is their susceptibility to photodegradation in the presence of oxygen and water. As a result, many previous reports of polymer lasers have resorted to the testing of their devices under vacuum [1,2].

In the real world, operation of devices under such conditions is not always practical. Commercial lasers, while often expensive, operate for many thousands of hours in ambient conditions. The fabrication of more robust polymer laser devices coupled with an increase in their operational lifetime would naturally be highly beneficial for the continued development of practical polymer lasers, capable of operating in less than ideal environmental conditions. The following work seeks to address the issues, which have been highlighted above.

In the initial sections of this chapter, the optical implications of encapsulating the polymer waveguide using a protective layer are discussed. This begins with modelling of the changes to the electric field profile and the impact modifying the waveguide has on the emission. The device structure and fabrication methods are then presented. The experimental setup is shown along with the resulting data from the operation of encapsulated polymer DFB lasers based on the polymer MEH-PPV for a

range of test conditions. The results show significant improvements in operational lifetime over the equivalent unencapsulated devices.

In latter sections, I move on to discuss photodegradation effects witnessed during the continuous operation of the lasers. Absorption and ellipsometry measurements are performed on the samples in order to quantitatively explain the degradation mechanisms ongoing under intense optical pumping.

5.2 Encapsulation of organic devices

5.2.1 Encapsulated organic light emitting diodes

Organic semiconductors and the cathode materials (such as calcium and LiF) used in the fabrication of organic light emitting diodes (OLEDs) are especially sensitive to moisture and oxygen. For display technology using such materials, no more than 10^{-5} to 10^{-6} g/m²/day [3] of water can permeate into the device without problems such as pixel shrinkage and the appearance of dark spots. As a result, the protection of semiconducting polymers in devices from the elements is especially important. Typical lifetime performance for OLED devices (Iridium G1, MEH-PPV) in air is only of the order of a few hours [4]. If device operation is under vacuum or after being encapsulated with silica however, one can expect lifetimes in the many hundreds or even thousands of hours [4,5] with one report for a stable blue-emitting device having an extrapolated lifetime of 100,000 hours at a brightness of 100 cd/m² [6]. This dramatic improvement in performance forms the basis for the study of applying the same principles to polymer distributed feedback lasers.

5.2.2 Encapsulated lasers

There has been widespread research using various DFB laser geometries [7-10] and polymeric energy transfer blends [11-13], in attempts to reduce the lasing threshold as part of the drive towards realising electrical pumping in polymer lasers [14-16]. Equally, there is extensive work studying the spectral properties of semiconducting polymer lasers. For example: broad tuning [17-18], emission wavelengths in the ultraviolet [19] and in the near infrared [17,20]. There is however, less quantitative data on the operational lifetime of polymer laser devices.

Emission from organic lasers operating in air is quickly quenched due to photo-oxidation. There have been reports however of an organic semiconductor laser (OSL) operating for some 2×10^7 pulses while under vacuum by Heliotis *et al.* [17] using a proprietary copolymer ‘RedF’, from Dow Chemicals. Other examples include an LPPP VECSEL laser, which had a lifetime of 3.6×10^7 pulses [21] and an Alq3-DCM waveguide laser that exhibited a lifetime of 10^6 pulses whilst pumped 100 times above threshold [22]. These compare well with solid-state dye lasers that have lifetimes typically on the scale of $10^5 - 10^6$ pulses.

Unlike the case with using OLEDs, encapsulating the DFB laser structure modifies the waveguide properties of the device (device structures and field profiles are shown in figures 5.1 and 5.2 respectively). Part of the potential for strong feedback in a very compact resonator is partly due to the large change in refractive index between the polymer and air ($\Delta n \approx 1$ at $\lambda = 630$ nm). Clearly, the choice of encapsulating material should attempt to maintain as high a Δn as possible while simultaneously providing protection to the active layer without substantially modifying the surface properties.

Additionally, the material should be transparent at the absorption and emission wavelengths of the polymer. McGehee *et al.* [23] and Gupta *et al.* [24] used this approach by encapsulating the active layer with a thin ($\sim 1\ \mu\text{m}$) layer of poly(methyl glutarimide) to protect the layer from photo-oxidation. However, the authors did not report any quantitative data on the effect of this encapsulation.

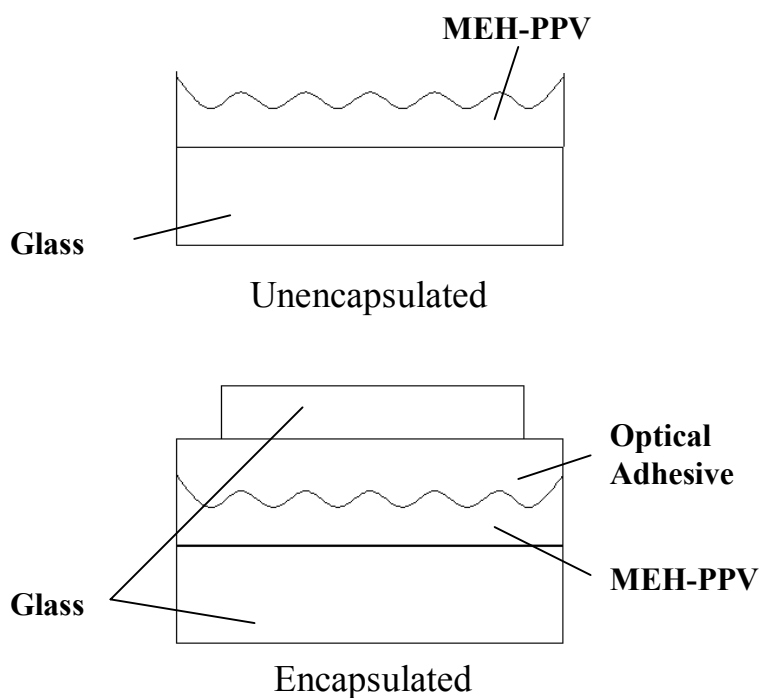


Figure 5.1: Device structures for the unencapsulated (top) and encapsulated (bottom) devices.

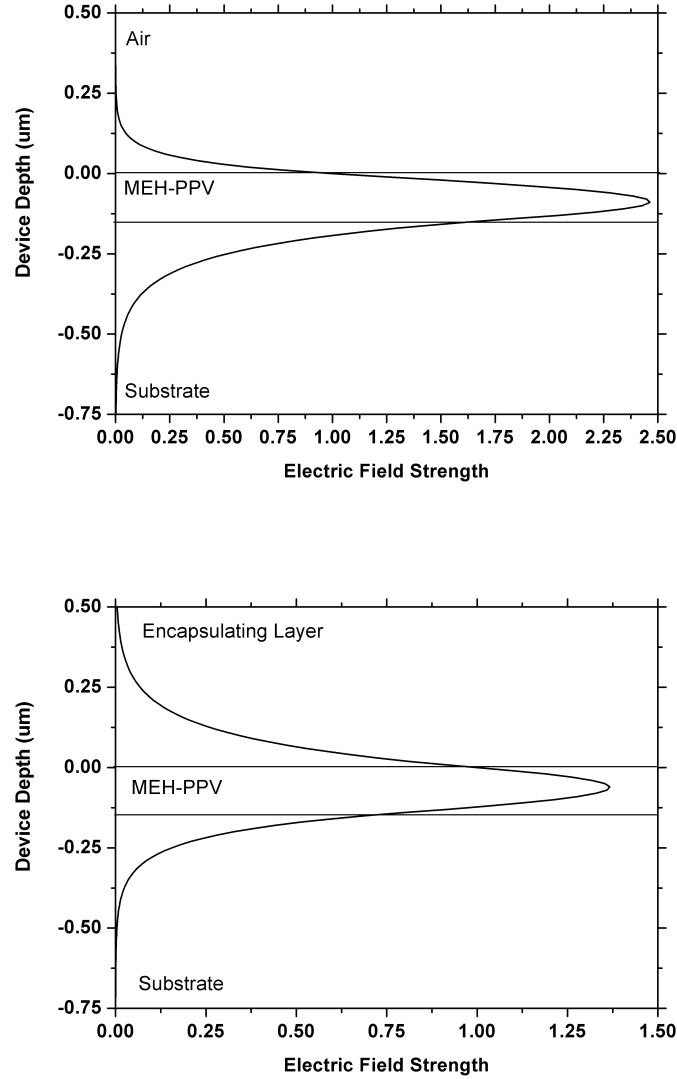


Figure 5.2: Layer boundaries as a function of depth for the unencapsulated (top) and encapsulated lasers with corresponding electric field profiles. The substrate for both devices is borosilicate glass ($n = 1.47$). The encapsulating layer (modelled) is the optical adhesive ($n = 1.58$). The refractive index of the MEH-PPV was taken to be 1.88 (at $\lambda = 630$ nm).

5.2.3 Experimental

In this section, fabrication of encapsulated polymer lasers with the aim of extending the operational lifetime is presented, along with the experimental set-up. The device consisted of a layer of MEH-PPV approximately 150 nm thick spin-coated onto a glass substrate with dimensions of 12 mm x 12 mm. The MEH-PPV solution concentration was 5 mg/ml in chlorobenzene.

Solvent assisted micromoulding was used to pattern the polymer film directly with a 2D ‘egg box’ sinusoidal corrugation of period 400 nm and approximate depth of 60 nm. The co-polymer mould was lightly wetted with chlorobenzene before it was brought into contact with the polymer film. Transfer time was 2 minutes and was performed under ambient conditions.

Devices were then transferred to a nitrogen atmosphere (glove box) in order to minimise the exposure of the MEH-PPV to oxygen and prevent oxygen bubbles being trapped during the encapsulating process. A small amount of optical adhesive (Norland 68) was added to the MEH-PPV surface. A borosilicate glass cover slip (150 μ m thickness) was lightly pressed into the adhesive forcing the Norland layer across the surface of the polymer removing any gas bubbles present between the MEH-PPV and the glass cover slip. The adhesive was cured using the 365 nm line of a UV lamp (8 W) for 3 minutes. Prolonged exposure was avoided to prevent any potential decrease to the PL of the polymer layer. A schematic of the encapsulation process is shown in figure 5.3.

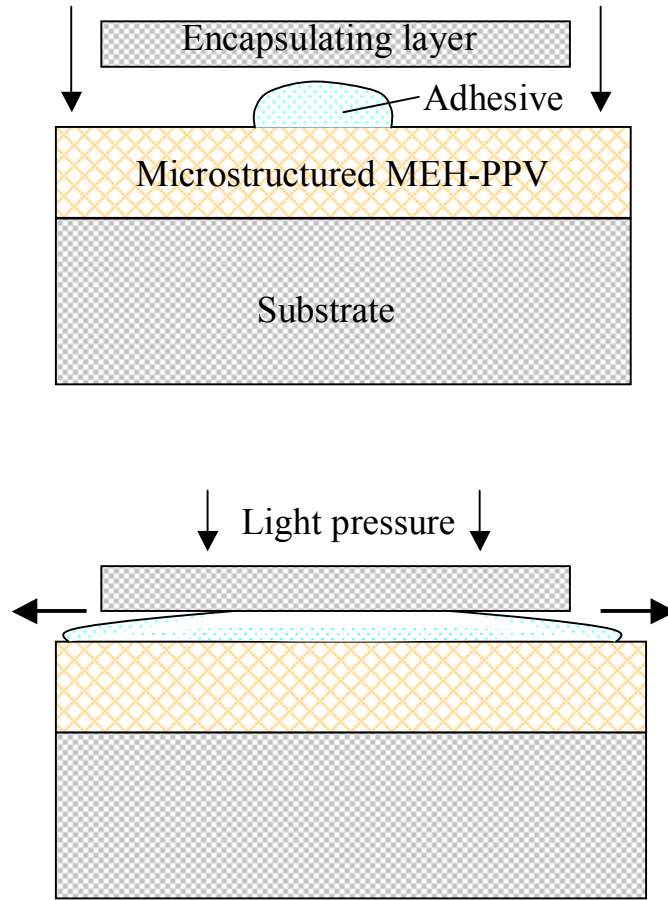


Figure 5.3: Schematic of the encapsulation method used to fabricate the lasers.

The samples were pumped using the 2nd harmonic of a passively Q-switched Nd:YVO₄ microchip laser (Alphas GmbH). The laser provided 1 ns pulses at a frequency of 5 kHz. Pulse energy was 1 μ J / pulse unattenuated. The frequency could be switched between 80 Hz and 5 kHz through use of an optical chopper and metallic neutral density filters were employed to attenuate the incident beam as required.

The beam was focussed to a spot size of approximately 10 μ m radius onto the encapsulated side of the laser. Alignment of the pump beam was trivial due to the corrugation covering some >80% of the sample surface. Spectral output from the laser

was measured around normal incidence using a fibre coupled CCD spectrometer of ~ 0.7 nm resolution (Triax 180, J.Y. Horiba). The experimental apparatus was depicted previously in chapter 3.

5.2.4 Results

Figure 5.5 below shows the range of lasing wavelengths observed for three separate unencapsulated lasers (top panel) and for a range of encapsulated lasers (bottom panel). The laser peak is typically established between 624 nm and 627 nm for the unencapsulated devices, the shift of a few nanometres consistent with small variations in the film thickness due to both the spin coating process and concentration of the polymer solution as the solvent evaporates. For the encapsulated devices, the lasing wavelength is red-shifted by around 10 nm from that of the unencapsulated devices for the same thickness of MEH-PPV, due to a slight increase in the effective index of the waveguide.

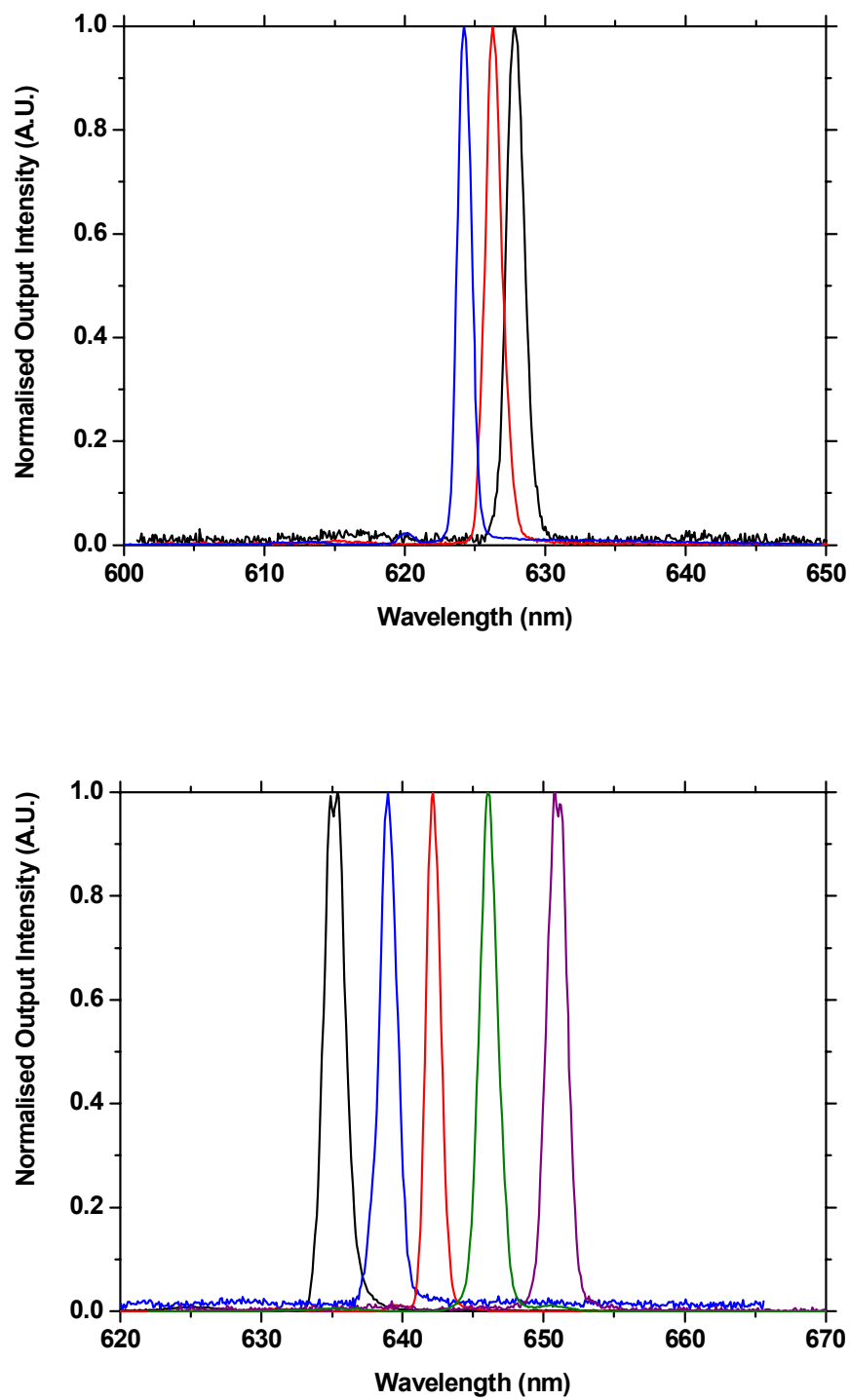


Figure 5.5: Range of emission wavelengths for unencapsulated lasers (top) and encapsulated lasers (bottom).

The spread in emission wavelengths is also greater for the encapsulated laser (~ 16 nm). Both sets of data are consistent with previous reports [18] demonstrating the potential for the tuning of the emission wavelength ($\Delta\lambda \sim 20$ nm) from MEH-PPV polymer lasers.

Output energy from a typical encapsulated laser was 2 nJ at 635 nm for a pump energy of 120 nJ. The threshold energy is ~ 30 nJ and a slope efficiency of 2.5% (for surface emitted output through the substrate). These values are similar to those reported for the unencapsulated lasers shown in the previous chapter and also for MEH-PPV DFB lasers in the literature [1,2]. The typical efficiency characteristics for an encapsulated laser are given in figure 5.6.

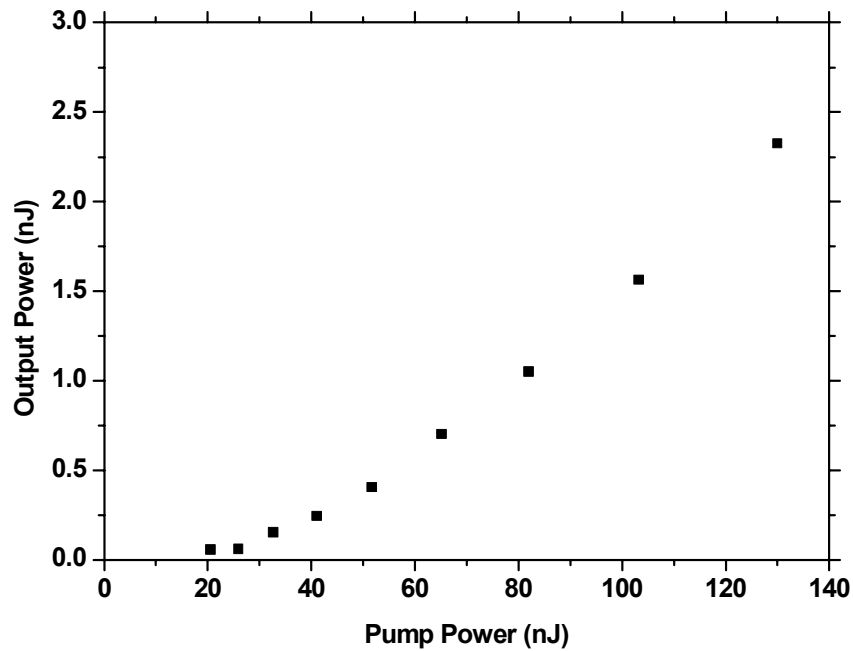


Figure 5.6: Power efficiency curve for a typical encapsulated laser device.

The consistency of the data values when comparing the power characteristics of encapsulated lasers to their unencapsulated counterparts, demonstrates there is no significant drawback to the fabrication technique. In this following section, the main advantage of encapsulating DFB lasers is detailed as we compare the lifetime performance of encapsulated and unencapsulated devices.

The experiment was set-up as described in the previous section. The pump beam was focussed onto the microstructured MEH-PPV surface. The detector was aligned close to normal incidence to collect the output beam. Once alignment was established, the sample's surface was moved a few microns along the x-axis via the translation stage, such that the focus of the pump beam remained constant, but a fresh region of film was pumped. Realigning the detector over this distance was trivial and could be performed quickly. This ensured that minimal damage or degradation was occurring locally to the film prior to the experiment. The experiment then recorded the output of the laser at regular time intervals while undergoing constant photopumping from the microchip pump source.

For the unencapsulated laser operating in ambient conditions, it quickly became evident that while operation of the device above threshold could readily be established at a pump repetition rate of 5 kHz, the output was incredibly unstable. Only a few seconds of operation could be maintained before the laser peak decayed into the background counts. An optical chopper was used to reduce the repetition rate to 80 Hz. At this frequency, the output beam was stable enough to perform the measurements. The result of this experiment for an unencapsulated laser is shown in figure 5.7

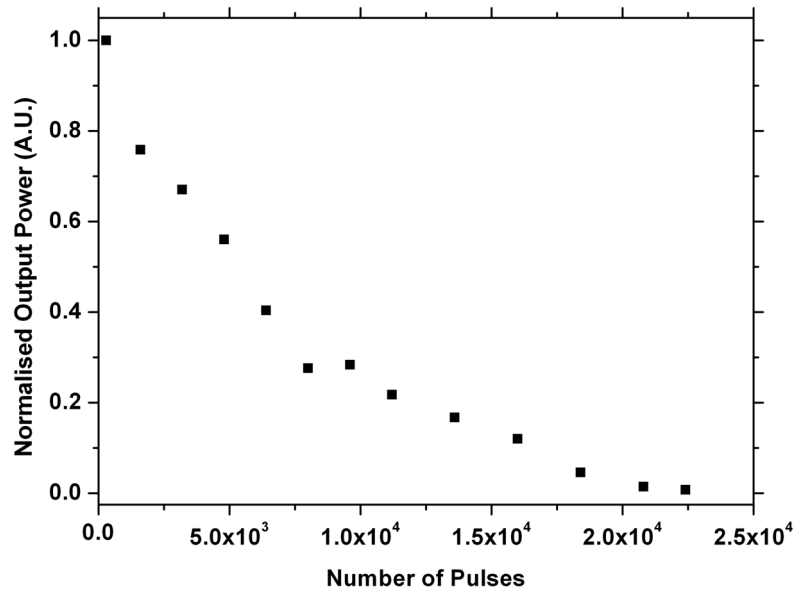


Figure 5.7: *Lifetime performance for an unencapsulated laser showing the decay in output power as a function of number of incident pump pulses.*

Figure 5.7 shows how the output power of the beam from a single region of the film decays with pump energy. The pump energy was 1 μJ per pulse. The values plotted are the integrals of the spectral curves obtained from the data after the background was removed. The values were then normalised relative to the initial value at time = 0 when the experiment began. After 6.5×10^3 pulses, the output has decayed to 40% of its initial value. This corresponds to ~ 90 seconds of constant operation. Further experiments exploring the effect of pulse energy on the unencapsulated laser by attenuating the beam resulted in a total lifetime of approximately 2×10^4 pulses for a pump energy of 300 nJ / pulse. This is a factor of 3 increase in lifetime for a third of the excitation energy – implying that the dose may be a key contributing factor.

With the encapsulated laser device, there were no issues in establishing a stable lasing output at the 5 kHz pump repetition rate. The experimental process was repeated for pump energies of 1 μJ , 500 nJ and 250 nJ per pulse to explore the effect of varying pump intensity versus device lifetime. For each of the pump energies, a new region of the sample was selected to prevent any cumulative effects from skewing the data. The results are shown below in figure 5.8. The spectral data were integrated and normalised relative to the initial value ($t = 0$) for each run.

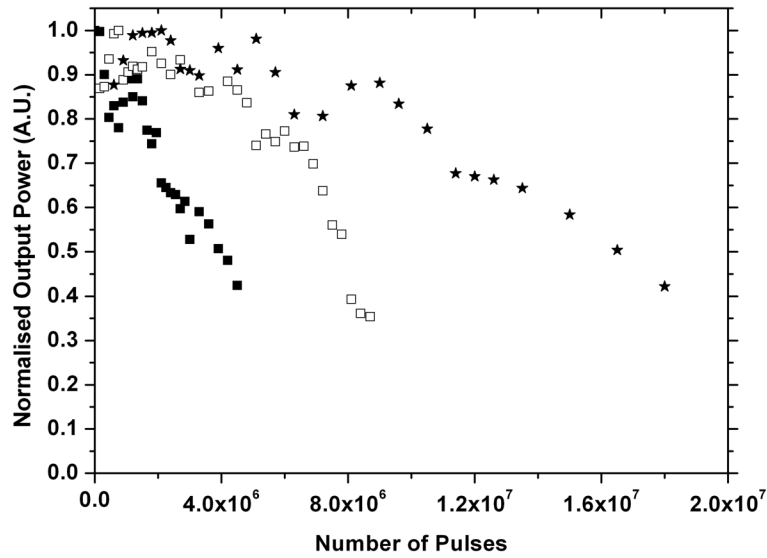


Figure 5.8. Lifetime performance of an encapsulated laser as a function of incident number of pulses for varying excitation intensities. Energy values are 1 μJ / pulse (solid squares), 500 nJ / pulse (open squares) and 250 nJ / pulse (filled stars).

The data in figure 5.8 represents continuous laser lifetimes of 15, 30 and 60 minutes respectively at the 5 kHz repetition rate whilst being pumped 40, 20 and 10 times above threshold respectively. The continuous operation of such a device for one hour or 2×10^7 pulses, during which output energy decays to 40% of initial, compares

well with values for other polymer lasers [16] and suggests great promise for developing cheap, disposable polymer laser sources from commercially available materials that can operate under ambient conditions. The initial scatter in the data at low numbers of pulses is attributed to photodegradation in the material whilst remaining oxygen present in the device interacts with the pump beam. When pumped at 250 nJ / pulse, the extension in continuous operating lifetime over the unencapsulated device pumped at the same incident energy is over 2500 times, showing that a major increase in lifetime performance can be achieved using the simple encapsulation process.

In order to try and extract as much continuous operation as possible from the encapsulated devices, an optical chopper was introduced to cut the repetition rate to 80 Hz, reducing the rate at which energy from the pump beam illuminated the polymer surface. An encapsulated device was pumped with an energy of 250 nJ / pulse at this frequency. The result of which is shown below, in figure 5.9 (open symbols), compared to an unencapsulated (filled symbols) laser.

This laser yielded a continuous operating lifetime of 28 hours. The gap in the dataset was when the experiment was left to run overnight. While reducing the pump frequency successfully extended the lifetime of the laser, the total number of pulses received by the polymer film was approximately the same as with the 5 kHz source ($\sim 10^7$). This may suggest that there is an upper limit to the energy per unit volume that MEH-PPV can absorb. The photostability of a material is defined as the total energy absorbed by one mole of the material in the sample when the output pulse energy has decreased to one-half of its initial value when measured [24]. Previous work with a pyrromethene laser dye in various solutions [24] report photostability values typically in the low tens of GJ/mol with a maximum value in a degassed 1,4-dioxane solvent of

1000 GJ/mol. Blends of pyrromethene and coumarin in both solution and in a solid polymer host (PMMA) [25] return similar figures, typically of low tens of GJ/mol with a maximum value of 350 GJ/mol for the blend (1:1 ratio/wt) when in a PMMA host. For the MEH-PPV encapsulated laser pumped with an energy of 250 nJ/pulse, the material absorbs a total of 4.25 J by the time it decays to 50% of its original value (equivalent to $\sim 1.7 \times 10^7$ pulses). If we assume a film density of 1 g/cm³, then for the volume of film undergoing pumping (44 μm^3) there are 2×10^{-13} moles of the MEH-PPV repeat unit. This gives us a photostability value for the encapsulated device of 21 TJ/mol, an order of magnitude greater than the best reported values for the P567 laser dye, a further indication of the performance of these polymer devices.

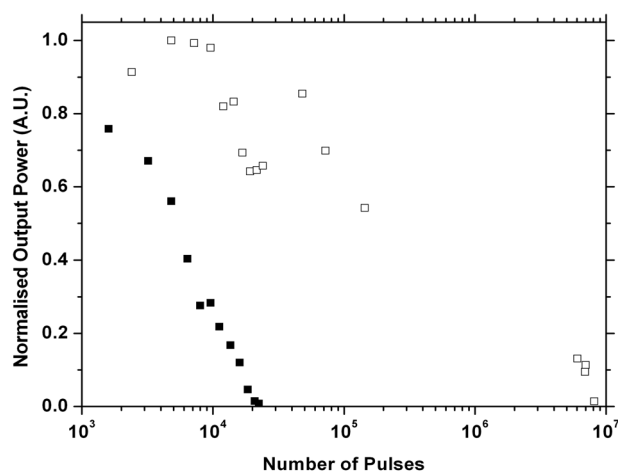


Figure 5.9: Comparison of an unencapsulated laser (filled symbols) operating for some 2×10^4 pulses (4 minutes) to an encapsulated laser pumped with the same frequency and energy per pulse. The encapsulated device operated above threshold for almost 10^7 pulses (28 hours).

When the energy of the pump beam was attenuated further to 100 nJ / pulse, the operational lifetime of an encapsulated device was further extended to almost 40 hours ($\sim 1.2 \times 10^7$ pulses). The experimental data for which is contained in Figure 5.10, shown below.

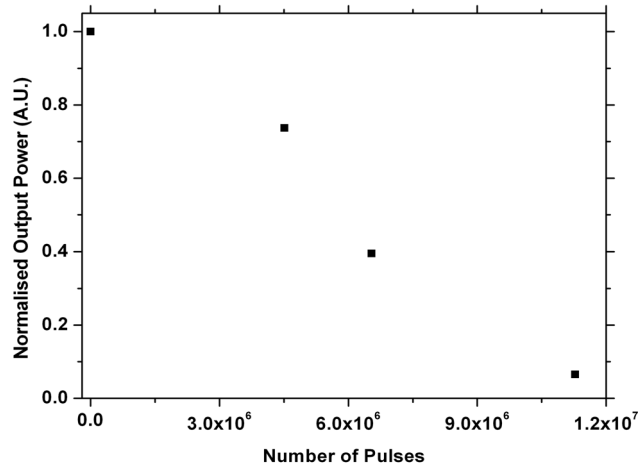
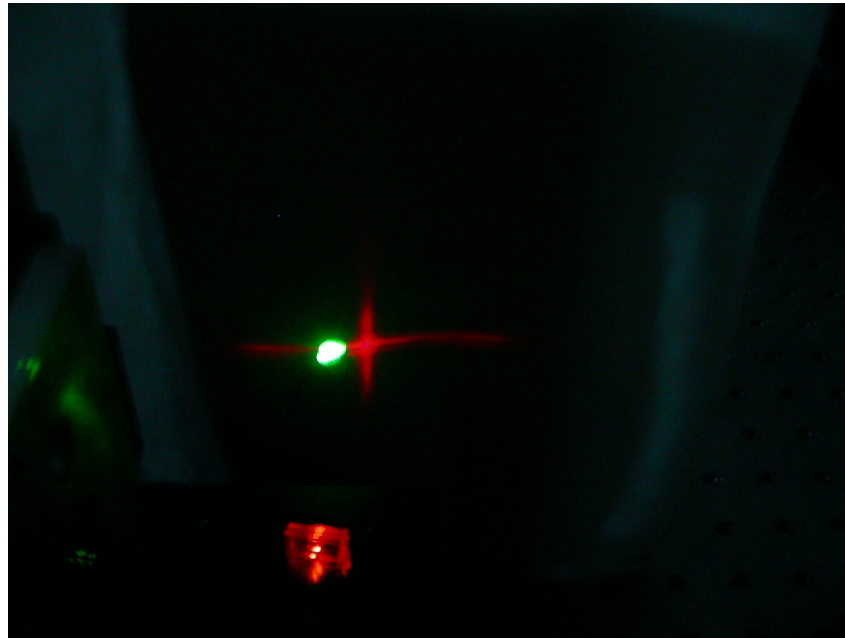


Figure 5.10: *An encapsulated laser operating continuously for almost 40 hours. Pump conditions were 100 nJ / pulse at a frequency of 80 Hz.*

In order for polymer laser technology to establish itself in the marketplace alongside conventional sources, many thousands of hours of operation would be required. Obviously, the demonstration of improved lifetimes presented here are not of this magnitude, however one should consider that over a 1 cm^2 microstructured area of polymer, assuming an excitation spot diameter of $20 \text{ }\mu\text{m}$, there are > 100000 possible emission sites. Provided one could ensure the device does not degrade sufficiently in the time it would take to exploit these sites, there is suddenly the potential for many thousands of hours operation. There may also be applications where shorter lifetime is acceptable, for example, disposable cartridges for point of care diagnostics.

The photograph in figure 5.11 (below) shows the experimental output of an encapsulated laser, operating some thirteen months after fabrication. The crossed-output of the encapsulated device can easily be seen (characteristic of the 2-D grating structure it is patterned with). The green spot is that of the pump source, a nitrogen pumped dye laser (rhodamine 110), operating at 532 nm with a repetition rate of 10 Hz. The spectral characteristics of this device can be found in figure 5.12.



***Figure 5.11:** Photograph of an encapsulated polymer laser in operation, thirteen months after fabrication. Laser emission is clearly visible. The encapsulated device can be seen in the foreground.*

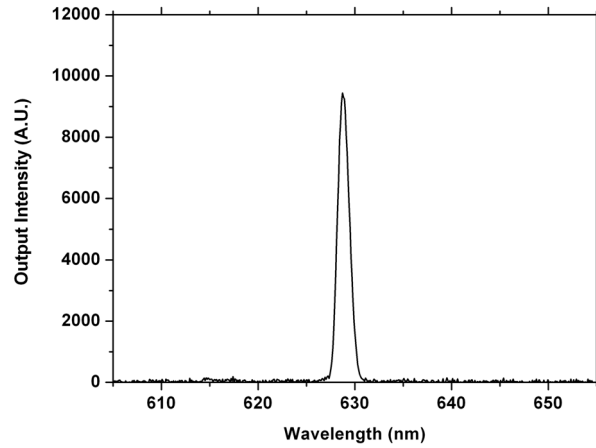


Figure 5.12: Spectral characteristics for the encapsulated polymer laser in figure 5.11 operating above threshold.

5.3 Photodegradation effects in encapsulated lasers

During the course of characterising the ability of encapsulated MEH-PPV distributed feedback lasers to operate continuously for extended periods an interesting side effect was recorded. As the number of incident pulses on the polymer increased, the laser emission wavelength underwent a steady blue-shift from its initial position. These emission characteristics were also noted in the study of the Dow proprietary red-emitting polymer ‘RedF’ by Heliotis *et al.* [16]. If one considers the Bragg condition for emission from the DFB laser:

$$m\lambda = 2n_{eff}\Lambda \quad [5.1]$$

We know that the period, Λ , is a constant. Therefore, any change to the emission wavelength must be related to a corresponding change in the effective index of the waveguide. In practice, for a blueshift to occur in the lasing output, the polymer must

react in such a way with the pump laser to cause a drop in the refractive index of the material.

5.3.1 Experimental

In this section, the experimental methods used for quantifying the photodegradation effects in MEH-PPV films are presented. Films were prepared from MEH-PPV (American Dye Source) using chlorobenzene as a solvent. The concentration was 5 mg / ml. Thin films of the solution were spin coated onto fused silica discs of 12 mm diameter.

Absorption measurements were performed with a Cary 300 Bio UV-Vis spectrophotometer from Varian Incorporated. A Baseline correction for all samples over a 650 nm range from 200 nm to 850 nm was applied and results taken with reference to a blank fused silica substrate. Markings around the edge of the quartz disc were used to ensure alignment of the samples remained constant for each data run.

The variable angle spectroscopic ellipsometry (VASE) was performed using a J.A. Woollam Co. Inc. M2000-DI ellipsometer. The system was calibrated using a silica wafer of known parameters prior to each run. Data was collected in intervals of 5° between 45° and 75° and intervals of 2° between 57° and 63°, close to Brewster's angle for a wavelength range of 190.55 – 1697 nm. Additional transmission information at 90° through the sample for p-polarisation was obtained. This data can be used to cross checking against the results gained from the absorption spectrometer. The VASE data was modelled by Dr. Olivier Gaudin at the University of St. Andrews using the WVASE32® analysis software (version 3.445) from J. A. Woollam Co., Incorporated.

To perform the ellipsometry successfully, a large area of the sample required exposure to the pump beam. As the output from the microchip laser is not suited to this task, an optical parametric oscillator (Continuum) was used. The OPO output was set to give an energy density equal to that of the microchip laser. Under lasing conditions, pulse energy was 40 μJ / pulse. The frequency and the wavelength of the OPO were set to 20 Hz and 532 nm respectively. Output spot size was approximately 10 mm diameter, centred on the middle of the sample.

5.3.2 Results

In figure 5.13 below, laser emission spectra are shown for the encapsulated laser tested in the previous section (frequency = 5 kHz, excitation energy = 250 nJ / pulse), which had operated continuously for one hour before decaying to 40% of its initial output. As can be seen, there is a clear blue-shift of the emission wavelength as a function of number of pulses. The full data set from this run has been re-plotted in figure 5.14 in terms of the wavelength of the output verses the number of pulses.

The total shift is ~ 3.5 nm or 0.2 nm per million pulses. This is a factor of 10 times larger than the shift observed by Heliotis *et al.* and suggests a greater extent of photodegradation in MEH-PPV compared to the RedF polymer. This wavelength shift requires a 0.5% reduction in the effective index of the device in order to satisfy equation 5.1. One explanation for this behaviour can be attributed to the conjugation level in the MEH-PPV. As the polymer absorbs an ever-increasing amount of energy from the pump beam, the conjugation length or number of alternating single-double bonds in a segment begins to break up into smaller components. The conversion of long-chain

segments into short-chain segments leads to emission from higher energy sites and an overall reduction in the refractive index of the material.

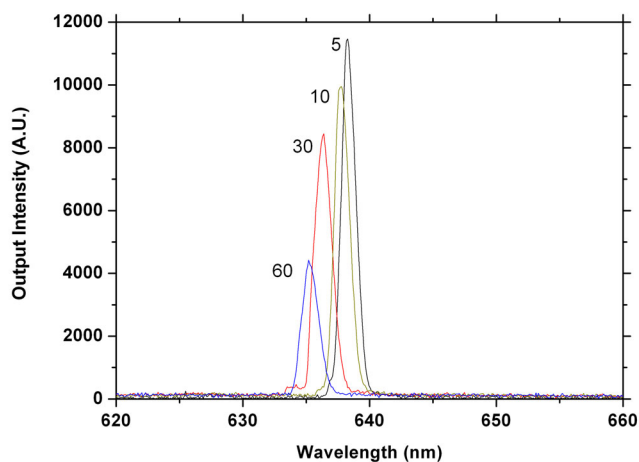


Figure 5.13: *Demonstration of the blueshift and decay of the emission wavelength for the encapsulated laser described in figure 5.8 (filled stars), as the number of pulses increases (pump energy = 250 nJ / pulse). Laser spectra are shown for the device at various time intervals (minutes).*

In order to quantify the hypothesis of refractive index change due to a breaking of the conjugation length, a series of experiments were performed comparing absorption spectra and ellipsometry data as detailed in section 5.3.1. To establish that the degradation was in fact a direct result of photo-oxidation due to the pump laser, two samples were prepared from a solution of MEH-PPV (5 mg / ml in chlorobenzene), spin-coated onto circular fused silica substrates of diameter 12 mm. One sample was stored under nitrogen between testing whilst the other was stored under ambient conditions. Both samples were kept in darkness. The purpose of the control was to eliminate the possibility of environmental effects on the degradation of the device.

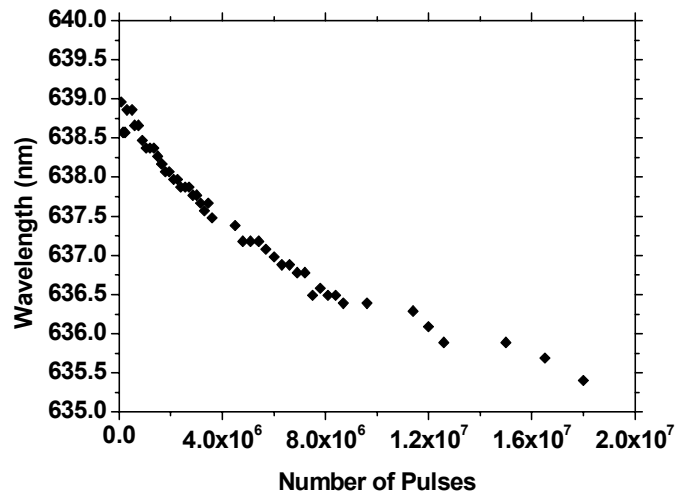


Figure 5.14: *The change in wavelength as a function of number of pulses for an encapsulated device operating for one hour (see figure 5.8, filled stars).*

In figure 5.15 below, the absorption spectra can be seen for the sample stored in nitrogen (top) and the sample stored in air (bottom) for a period of just over 8 days. In both cases, there is a small reduction in amplitude of the absorption feature centred on 490 nm. The sample stored under nitrogen had a reduction of 2.2% after 212 hours, as opposed to 8.2% for the sample stored in air. For both control samples, there is no discernable shift of the absorption spectra to either the red or blue. While this loss of absorption due could be a contributing factor to the decrease in refractive index, it is reasonable to conclude from the data that this process is due to ambient conditions alone is too slow to account for the degradation witnessed during laser operation.

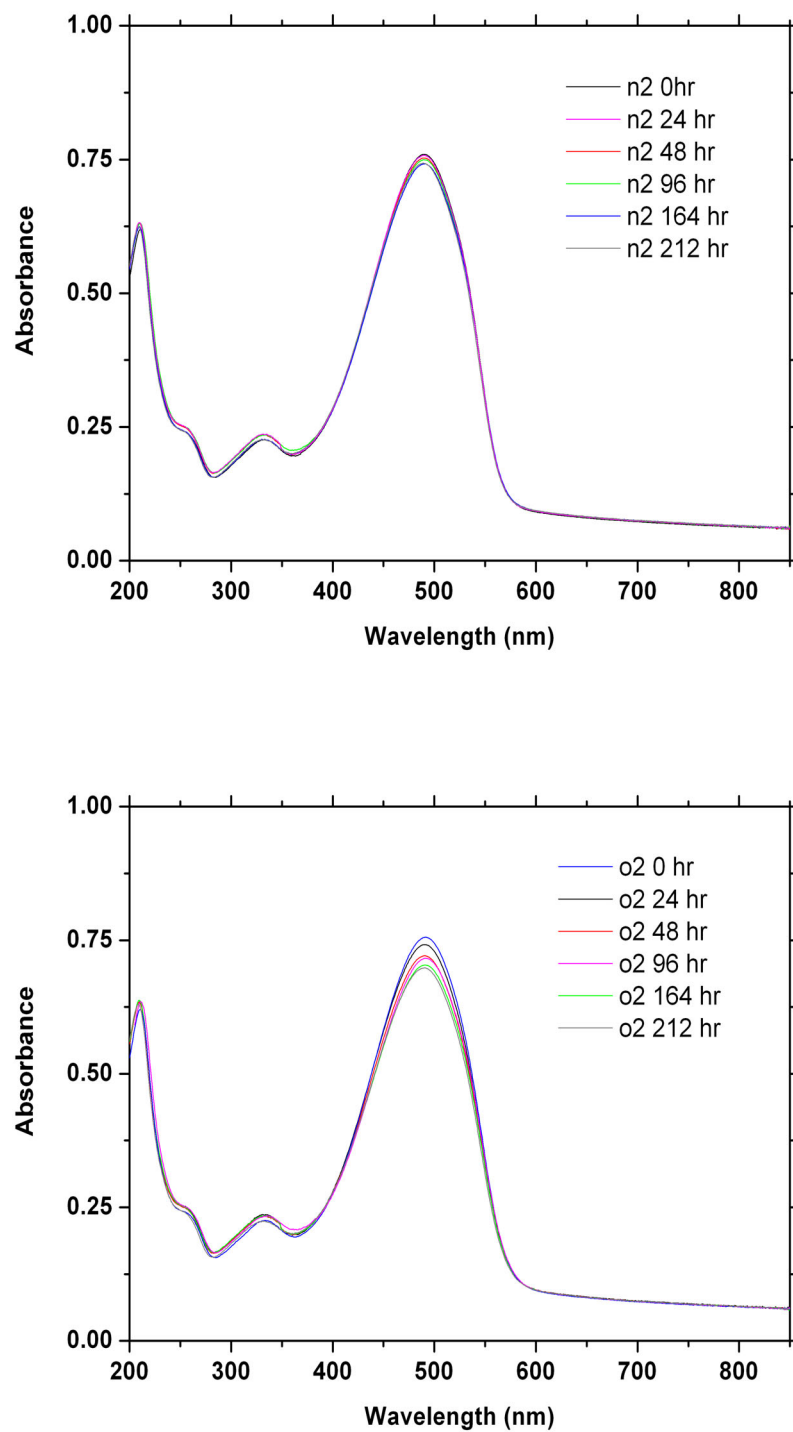


Figure 5.15: Demonstration of changes to the absorbance of MEH-PPV over an 8 day period when stored under nitrogen (top) and oxygen (bottom).

To quantify the effects of photo-induced degradation, a second experiment directly measuring the effect of the pump beam on a film of MEH-PPV (5 mg / ml in chlorobenzene spin-coated onto a fused silica substrate of diameter 12 mm) was prepared. Additionally, a control sample was prepared under identical conditions. Both films had a thickness of 94 ± 3 nm as derived from VASE data.

Absorption spectra were recorded for both the control and the test sample immediately after fabrication and were found to be identical. The control sample was then placed under vacuum (10^{-3} mbar) for one hour while the test sample was exposed to the output of the OPO for one hour (see section 5.3.1), also under a vacuum of 10^{-3} mbar. After exposure, both samples were removed from their respective chambers and absorption spectra were again recorded. The control sample was unchanged from its initial trace. The exposed sample however, had changed remarkably. The results of this experiment are plotted below, in figure 5.16.

After the exposure, the absorption peak underwent a strong reduction in amplitude (36.1 %) as well as showing signs of broadening. The peak of the visible absorption underwent a blue-shift of 18 nm. This behaviour can be directly related to the shift of the laser peak witnessed earlier by understanding the absorption spectrum of the MEH-PPV polymer.

In PPV and its derivatives, the low-energy band is assigned to transitions between delocalised π -bands [27]. The changes to the spectra for the exposed sample in this region strongly suggest degradation of the π -electron conjugated system. This is an effective reduction of the conjugation length for the polymer chains. Similar behaviour to this has been witnessed in photodegradation studies of MEH-PPV [28] and also in other conjugated polymers [29,30]. This has been assigned to the formation of oxidized

carbon species along the chains due to the presence of oxygen, which is in the environment [28,29] and also trapped in the film [29]. Direct film degradation due to ablation or heating from the laser is unlikely at this power level of laser pulse. Although experiments were performed under vacuum, fabrication of the devices was in air, thus it is possible that the oxidative degradation of the MEH-PPV film during the exposure is due to oxygen trapped in the film. Fully degassing solutions and preparing devices in an inert atmosphere if this is the case could achieve further improvements in lifetime.

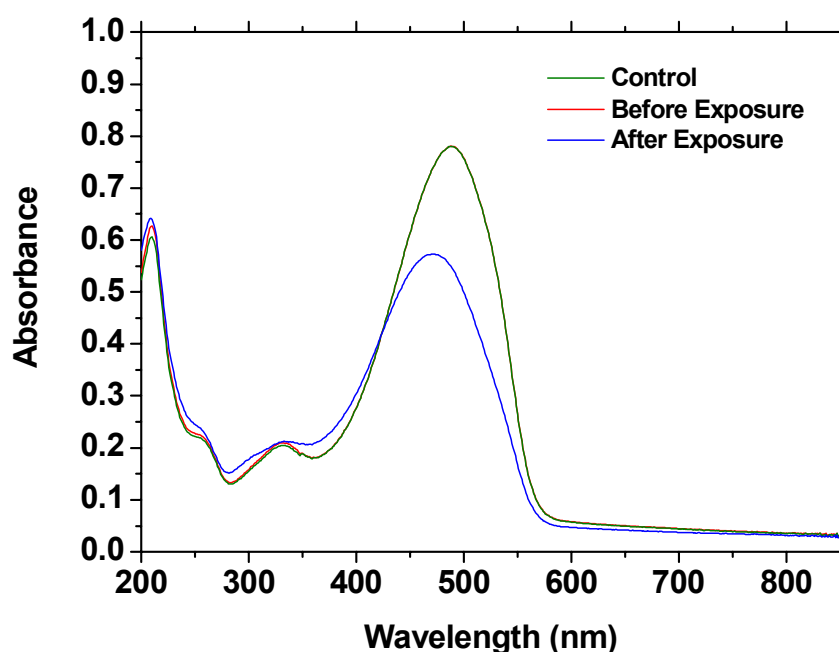


Figure 5.16: Absorption profile of a MEH-PPV sample before (red line) and after (blue line) exposure to the laser source. The absorption by the control sample (green line) was unchanged over the one-hour time period while held under vacuum, and so only one line has been plotted for clarity.

The analysis of the VASE data was restricted to wavelengths longer than 600 nm. In this region, the polymer does not absorb incident light allowing the extinction coefficient to be set to zero. The films analysed were assumed to be isotropic. This reduces parameter correlation problems as a limited number of samples were tested – preventing a multi-sample analysis to be performed [31,32]. To constrain the model further, normal incidence intensity transmission data were also fitted [33]. The refractive index was assumed to be a two-coefficient Cauchy function of the wavelength.

The result of this analysis is shown below in figure 5.17. The solid curve is for the control experiment, obtained immediately after fabrication. The dotted curve is for the exposed sample, clearly demonstrating a reduction in the index over the wavelengths of interest accounting qualitatively for the wavelength shift in figure 5.14. Optical anisotropy would need to be taken into account to provide a more precise analysis.

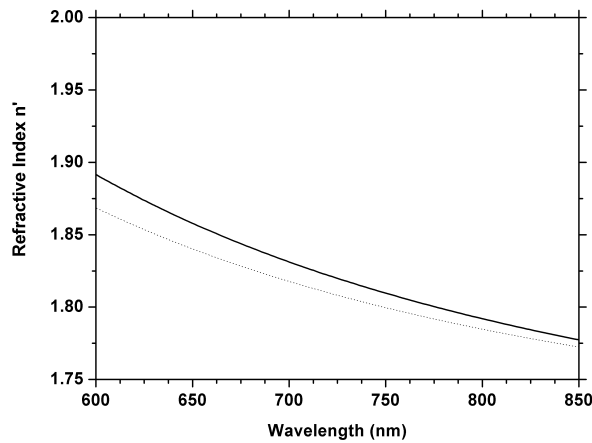


Figure 5.17: The index of refraction as a function of wavelength for the control sample after fabrication (solid curve) and the test sample after a one-hour laser exposure (dotted curve). The reduction in index is clearly visible.

5.4 Towards improved device performance

The ability to extract many thousands of hours of performance from a device without significant reduction in its inherent optical properties could make organic semiconducting lasers very attractive to industry. As has been demonstrated earlier in this section, encapsulating a polymer DFB laser can extend its operational lifetime by several orders of magnitude.

The lasers presented in the work above collectively attempt to exclude environmental conditions passively by forming a barrier layer between the harmful oxygen and the polymer film. The ability to actively remove or ‘get’ any oxygen present in a device would serve to bolster the performance against degradation. This is precisely the function of incorporating a getter into the device.

The use of a getter material is based on the ability of certain solids to collect free gases. This can be performed via absorption, adsorption or occlusion. Getters are widely utilised in the electronics field, one common example being silica gel, which is used as a desiccant to help control humidity. For this work, the getter material is based on an alloy of Zirconium, Cobalt and rare earth metals in powder form with a metal backing for stability, commercially available from Saes getters [3]. Zirconium has valuable getting characteristics as it forms very stable solid compounds with oxygen, nitrogen and carbon dioxide.

As an extension to the above work, efforts were made to incorporate a getter into the design of an encapsulated laser. One possibility was to use the getter material directly and apply the powder to the surface of the polymer film before the encapsulation process began. A schematic of this structure is depicted in figure 5.18

below. The issue with this approach is that the opaque powder obscured the beam path through the device, at best acting as multiple scattering centres as the pump beam was incident on the surface.

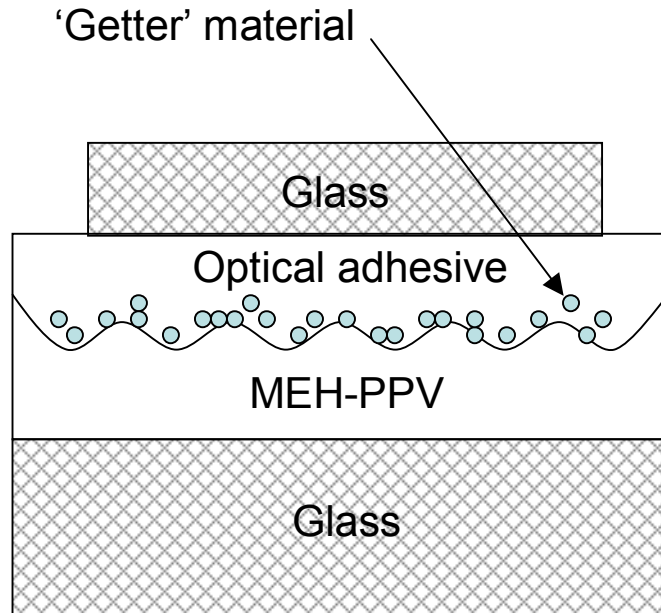


Figure 5.18: Structure of an encapsulated DFB laser illustrating the positioning of the getter material between polymer and encapsulating layer.

An alternative geometry would be to encase both the getter and the DFB laser within a sealed compartment. This would allow for the removal of excess oxygen without impeding the optical path through the device. Figure 5.19 shows a photo of an early prototype device of this arrangement. A coverslip is attached to one side of a reusable aluminium frame using optical adhesive, forming a recessed chamber into which a getter and an unencapsulated DFB polymer laser can be inserted. Attaching a second coverslip to the remaining face of the aluminium frame completes the encapsulation. All fabrication was performed under a nitrogen atmosphere within a

glove box. The streaking effect apparent in the polymer film is a reflection from the surface upon which the device is positioned and not an indication of film quality. The initial foray into fabricating this geometry exposed the issue of ensuring the polymer layer is not sealed against the outer glass encapsulating slips, which are prone to concaving. Re-addressing the makeup and dimensions of the components should solve this issue and produce good quality devices ready for extensive testing.

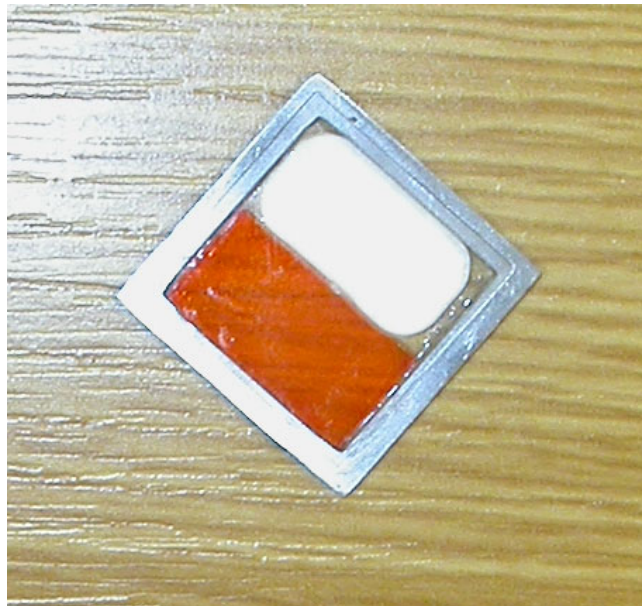


Figure 5.19: Photograph of prototype design of an encapsulated laser incorporating an active getter device.

5.5 Summary

In this chapter, a MEH-PPV distributed feedback laser was successfully encapsulated using an optical adhesive and silica layer without any substantial impact on the threshold or efficiency. For equivalent pump energies, an encapsulated laser ran under continuous operation for a total of 1.8×10^7 pulses during a 1-hour period, an improvement over the unencapsulated laser of over 2500 times and similar to the best reported values for other polymers tested under vacuum. By reducing the frequency of the excitation source from 5 kHz to 80 Hz, an encapsulated laser operated above threshold for almost 40 hours. This result, coupled with the demonstration that devices can be stored in ambient conditions and operate many months later shows the great potential for the development of practical polymer lasers with many thousands of hours lifetime.

The photostability of the MEH-PPV film was calculated to be 21 TJ/mol and compared to that of some common dye lasers showing an order of magnitude increase for the pump conditions used.

Through a combination of absorption measurements and variable angle spectroscopic ellipsometry, a 4 nm blue-shift of the emission wavelength during operation is explained. A photodegradation of the π -conjugated system and formation of oxygen groups in the polymer leads to an effective reduction in the conjugation length of the material, this is evident in the ellipsometry data for a sample after a 1-hour exposure to a laser source, when compared to a non-exposed sample.

Finally, the potential for developing even more efficient lasers by actively removing oxygen from the device through the use of getters was addressed and could be a key development for the future fabrication of encapsulated laser devices.

5.6 References

- [1] J.R. Lawrence, G.A. Turnbull and I.D.W. Samuel, *Applied Physics Letters*, **82**, 4023 (2003).
- [2] G.A. Turnbull, P. Andrew, W.L. Barnes and I.D.W. Samuel, *Applied Physics Letters*, **82**, 313 (2003).
- [3] Stefano Tominetti, SAES Getters S.p.A., Lainate, Italy.
- [4] S. Stephenson, Private Communication.
- [5] A. McNeill, Private Communication.
- [6] Cambridge Design Technology (<http://www.cdtltd.co.uk/technology/36.asp>)
- [7] S.V. Frolov, Z.V. Vardeny and K. Yoshino. *Applied Physics Letters*, **72**, 1802 (1998).
- [8] A. Rose, Z.G. Zhu, C.F. Madigan, T.M. Swager and V. Bulovic. *Nature*, **434**, 876 (2005).
- [9] V.G. Kozlov, G. Parthasarathy, P.E. Burrows, V.B. Khaflin, J. Wang, S.Y. Chou and S.R. Forrest, *Ieee Journal of Quantum Electronics*, **36**, 18 (2000).
- [10] G. Heliotis, R.D. Xia, G.A. Turnbull, P. Andrew, W.L. Barnes, I.D.W. Samuel and D.D.C. Bradley, *Advanced Functional Materials*, **14**, 91 (2004).
- [11] T. Riedl, T. Rabe, H.H. Johannes, W. Kowalsky, J. Wang, T. Weimann, P. Hinze, B. Nehls, T. Farrell and U. Scherf, *Applied Physics Letters*, **88** (2006).
- [12] R. Gupta, M. Stevenson, M.D. McGehee, A. Dogariu, V. Srdanov, J.Y. Park and A.J. Heeger, *Synthetic Metals*, **102**, 875 (1999).
- [13] R.D. Xia, G. Heliotis, B.Y. Hou and D.D.C. Bradley, *Organic Electronics*, **4**, 165 (2003).

- [14] N. Tessler, *Advanced Materials*, **11**, 363 (1999).
- [15] M.D. McGehee and A.J. Heeger, *Advanced Materials*, **12**, 1655 (2000).
- [16] I.D.W. Samuel and G.A. Turnbull, *Chemical Reviews*, **107**, 1272 (2007).
- [17] G. Heliotis, R.D. Xia, D.D.C. Bradley, G.A. Turnbull, I.D.W. Samuel, P. Andrew and W.L. Barnes, *Journal of Applied Physics*, **96**, 6959 (2004).
- [18] G.A. Turnbull, T.F. Krauss, W.L. Barnes and I.D.W. Samuel, *Synthetic Metals*, **121**, 1757 (2001).
- [19] D. Schneider, T. Rabe, T. Riedl, T. Dobbertin, M. Kroger, E. Becker, H.H. Johannes, W. Kowalsky, T. Weimann, J. Wang, P. Hinze, A. Gerhard, P. Stossel and H. Vestweber, *Advanced Materials*, **17**, 31 (2005).
- [20] D. Schneider, T. Rabe, T. Riedl, T. Dobbertin, M. Kroger, E. Becker, H.H. Johannes, W. Kowalsky, T. Weimann, J. Wang and P. Hinze, *Applied Physics Letters*, **85**, 1886 (2004).
- [21] S. Stagira, M. Zavelani-Rossi, M. Nisoli, S. DeSilvestri, G. Lanzani, C. Zenz, P. Mataloni and G. Leising, *Applied Physics Letters*, **73**, 2860 (1998).
- [22] V.G. Kozlov, V. Bulovic, P.E. Burrows, M. Baldo, V.B. Khaflin, G. Parthasarathy, S.R. Forrest, Y. You and M.E. Thompson, *Journal of Applied Physics*, **84**, 4096 (1998).
- [23] M.D. McGehee, M.A. Diaz-Garcia, F. Hide, R. Gupta, E.K. Miller, D. Moses and A.J. Heeger, *Applied Physics Letters*, **72**, 1536 (1998).
- [24] R. Gupta, M. Stevenson and A.J. Heeger, *Journal of Applied Physics*, **92**, 4874 (2002).
- [25] M. Ahmed, T.A. King, D.-K. Ko, B.H. Cha and J. Lee, *Optics Communications*, **203**, 327 (2002).

- [26] M. Ahmed, T.A. King, D.-K. Ko, B.H. Cha and J. Lee, *Optics and Laser Technology*, **34**, 445 (2002).
- [27] M. Chandross, S. Mazumdar, S. Jeglinski, X. Wei, Z.V. Vardeny, E.W. Kwock, and T.M. Miller, *Physical Review B*, **50**, 14702 (1994).
- [28] M. Atreya, S. Li, E.T. Kang, K.G. Neoh, Z.H. Ma, K.L. Tan, and W. Huang, *Polym. Degrad. Stab.*, **65**, 287 (1999).
- [29] S.M. Lipson, D.F. O'Brien, H.J. Byrne, A.P. Davey, and W.J. Blau, *Thin Solid Films*, **370**, 262 (2000).
- [30] J. Ficker, H. von Seggern, H. Rost, W. Fix, W. Clemens, and I. McCulloch, *Applied Physics Letters*, **85** 1377 (2004).
- [31] C.M. Herzinger, B. Johs, W.A. McGahan, J.A. Woollam, and W. Paulson, *Journal of Applied Physics*, **83**, 3323 (1998).
- [32] M. Tamer and A.P. Monkman, *Advanced Materials*, **14**, 210 (2002).
- [33] B. Johs, R.H. French, F.D. Kalk, W.A. McGahan, and J.A. Woollam, *Proc. SPIE*, **2253**, 1098 (1994).

Chapter 6: Gain and absorption saturation in conjugated polymers.

6.1 Introduction

In chapter 2, I discussed the ways that a two level system could interact with light along with the associated transitions between the ground state (N_1) and excited state (N_2). It is this interaction and the subsequent populating of the N_2 level that is responsible for the onset of gain in these conjugated materials and hence amplification.

The number of atoms in the N_2 state is a key factor in the availability of phenomena such as amplified spontaneous emission (ASE). If the fraction of atoms promoted from the ground state to the excited state is large and the gain of the active material (given by equation 6.1 where σ is the absorption cross section and L is the length of the cavity) is high enough, then the stored energy is preferentially emitted from the medium into a given solid angle. This provides directionality to the emission (as opposed to spontaneous emission). The output also typically displays spectral narrowing.

$$G = e^{\sigma(N_2 - N_1) / L} \quad [6.1]$$

A high population density in the N_2 state is beneficial in aiding the amplification of a weak incident probe beam. As the excited state population is reduced, the gain becomes saturated. This occurs as the pump beam intensity is increased. When the pump intensity equal to that of the saturation intensity I_{SAT} [1], we obtain the situation

where a material becomes bleached and the difference in the populations of the levels $\Delta N = N_1 - N_2$ is equal to $N_T/2$ (where N_T is the total population of the system).

Further complications to this picture occur by including the role of the exciton in depleting the excited state further. Excitons diffusing through the material collide into each other transferring the energy from the collision onto one of the particles. This exciton is promoted to a higher excited state before immediately undergoing a fast radiationless transition back to the N_2 level. Meanwhile the other exciton relaxes back to the ground state, thus removing a significant fraction of the excited state population. This in turn has an effect on the ability of a conjugated polymer to absorb incident light.

In this section, optical transitions and mechanisms such as gain and exciton-exciton annihilation are explored for conjugated materials undergoing intense optical pumping.

Firstly, a demonstration of a solution based polymer amplifier is presented. Polymer optical fibres have featured strongly in the recent, intense development of high-speed optical communication systems [2]. While high optical attenuation currently prevents their usage in long-haul networks, the low cost of polymer technology is attractive over short-haul local area networks where bandwidth, higher than is possible with copper wire, is desired. Plastic fibres exhibit increased durability and flexibility over their silica counterparts [3] as well as offering larger core diameters, which are less prone to coupling losses associated with misalignment. Semiconducting polymers are also known for showing high optical gain throughout the visible range where their high chromophore density promotes strong gain from a compact volume and are relatively free from concentration quenching which affects the performance of organic dyes [4,5].

The overlap of gain in conjugated polymers and the main transmission window of polymer optical fibre suggests applications for within this area.

In the latter half of this chapter, the ability of thin films of MEH-PPV to absorb light under saturating conditions is presented. By modelling the change in intensity through the film including terms describing the exciton-exciton annihilation, a fit to the experimental data allows the annihilation rate to be calculated for MEH-PPV. A discussion of the results compare the values obtained here to those measured for the material using alternative techniques.

6.2 Solution based optical amplifier

In this section, the operating characteristics of a solution based optical amplifier are presented. Despite the strong interest in the realisation of such devices, prior to this work, there had only been a single demonstration of such an optical amplifier [6]. This section of work was carried out in collaboration with Dr. George Heliotis of Imperial College during a visit he made to the University of St. Andrews and with Dr. Mark Goossens, of the University of St. Andrews. My role in this work was in performing the experimental measurements upon the solution based amplifier.

6.2.1 Experimental

The material used in this experiment was the conjugated polymer poly(9,9-dioctylfluorene-*co*-benzothiadiazole) (F8BT, supplied by The Dow Chemical Company), the structure of which is shown in figure 6.1 along with the absorption and emission spectra for the polymer. A modified Photonics Technology International GL-302 dye laser was employed in a standard pump-probe configuration. A nitrogen laser

with output characteristics of $\lambda = 337$ nm, 500 ps pulse duration and 7 Hz repetition rate was used as a common excitation source to transversely pump the cells containing both the probe dye laser and the F8BT polymer amplifier. This output was split into two beams one of which pumps the dye laser (configured as a grazing incidence Littman oscillator), which can be tuned over the range of 530 nm to 590 nm. The output of the dye laser is focussed to a spot size of $150 \times 200 \mu\text{m}^2$ and is carefully aligned to spatially overlap the excited region of the polymer amplifier, which is pumped by the second part of the nitrogen output with dimensions of 10 mm x 200 μm . The input signal intensity was adjusted by using calibrated neutral density filters. The system is configured such that the probe beam enters the amplifier approximately 0.5 ns after the pump beam (the photoluminescence lifetime of the F8BT polymer being ~ 2 ns [7]). A schematic of the experimental layout is shown below in figure 6.2.

Four concentrations of dilute F8BT solution were prepared (1.5, 3, 3.5 and 6 mg / ml) and contained within a quartz cuvette that was tilted at an angle of 10° to avoid reflections from the walls providing feedback for laser oscillation. The solutions were pumped at a constant energy of 350 $\mu\text{J}/\text{pulse}$. To cover the wavelength range required by the probe beam, the laser dyes Rhodamine 110 ($\lambda = 530 - 550$ nm, 7.5 mg/ml in ethanol), Fluoresceine 27 ($\lambda = 550 - 562$ nm, 1 mg/ml in ethanol and seeded with NaOH) and Rhodamine 590 ($\lambda = 568 - 600$ nm, 1.5 mg/ml in methanol) were prepared.

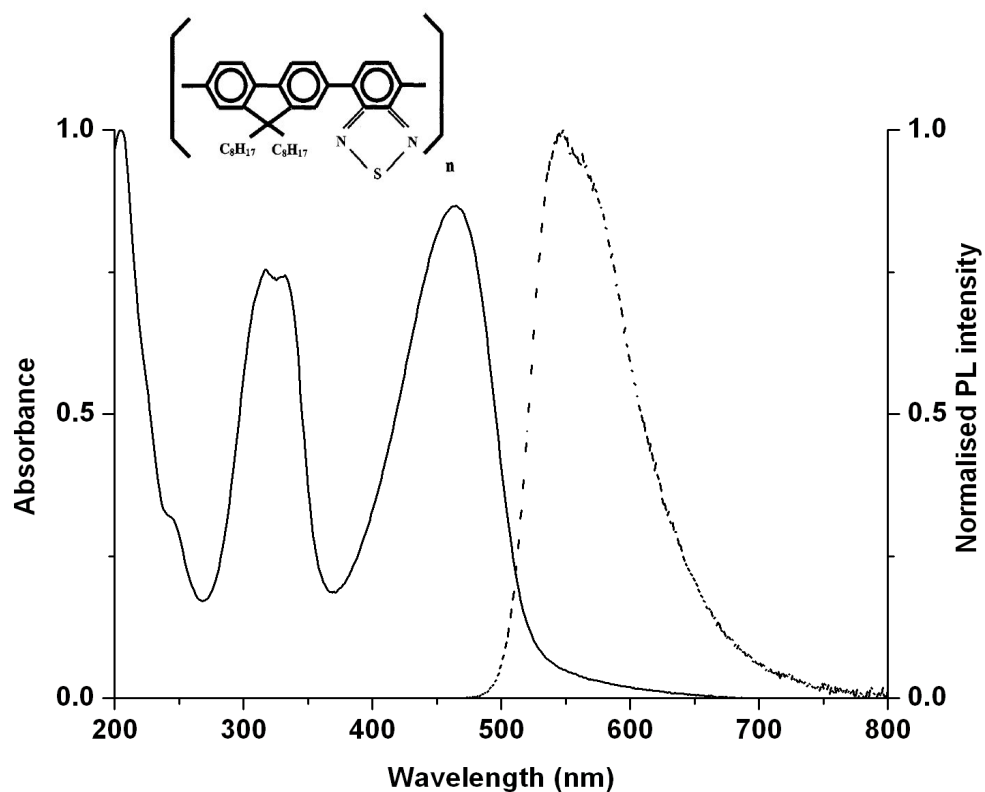


Figure 6.1: The absorption and emission spectra of the polymer F8BT. The chemical structure is shown in the inset.

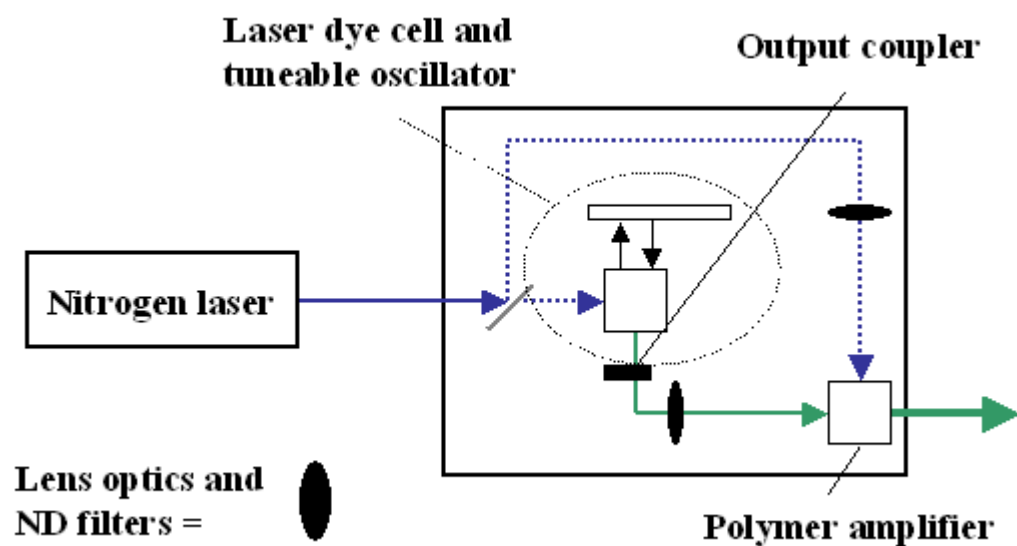


Figure 6.2: Schematic representation of the pump/probe amplifier set-up.

6.2.2. Results

In figure 6.3 below, amplification of a weak probe signal by the F8BT solution is demonstrated. The graph shows the weak input signal in the absence of a pump beam (black line) from a Rhodamine 110 dye laser ($\lambda = 543$ nm) detected after passing through an F8BT cell of concentration 1.5 mg/ ml. Initially, the polymer chains are in their ground state and there is no interaction between the probe beam and the polymer apart from some small scattering losses. Once the solution is optically pumped, polymer chains are promoted to excited states. As a result, the probe beam is amplified (red line) by stimulated emission. For this solution concentration, the probe beam is amplified some 27.5 times corresponding to a gain of 14 dB. With careful optimisation of the solution concentration and beam alignment, the F8BT solution (3.5 mg/ml concentration) can amplify an input signal ($\lambda = 536$ nm) by a factor of 3460, corresponding to a gain of 35.4 dB [8].

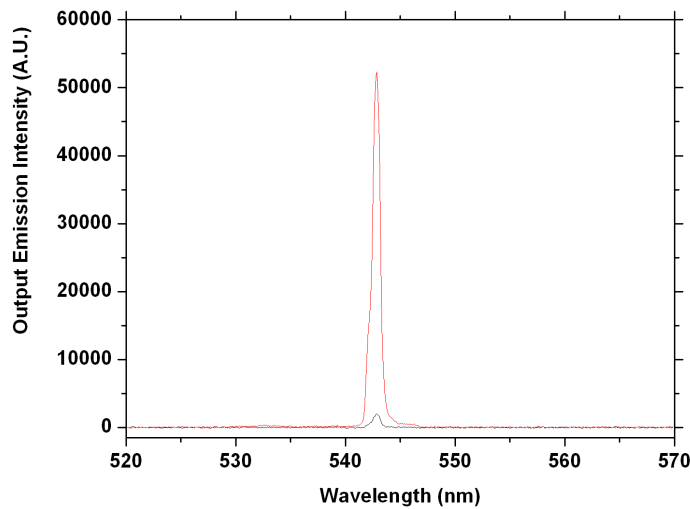


Figure 6.3: Optical amplification (red curve) of a weak input signal (black curve) after passing through the F8BT amplifier.

Additionally, there is no broadening of the input signal by the amplifier (within the 0.6 nm resolution of the spectrograph). It is also clear from figure 6.3 that the emission noise reaching the detector after amplification is very low indicating a high signal to noise ratio. The typical emission noise in the absence of an input signal is shown below in figure 6.4.

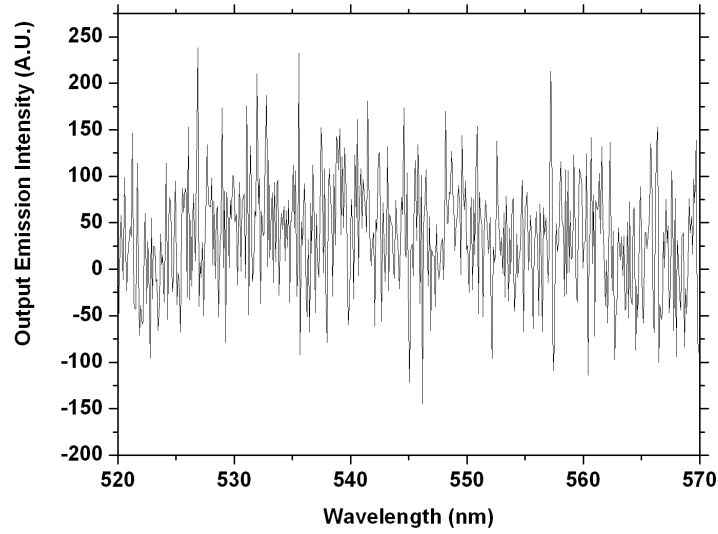


Figure 6.4: Typical polymer emission noise in the absence of an input signal.

Variation of the polymer concentration modifies the excitation density N_{ex} and therefore the gain coefficient g as given by $g = \sigma_{se}N_{ex}$, where σ_{se} is the stimulated emission cross-section. Low concentrations provide low excitation densities while solutions with high concentrations (above the 3.5 mg/ml optimum) absorb the pump radiation within a much shorter distance of the cuvette face upon which the light is incident. This leads to a smaller overlap between the pump and probe beams limiting the available amplification [6].

One attractive aspect of conjugated polymers is their ability to show gain over a broad spectral range [6,8] making them excellent candidates for cheap, broadband amplifiers. This aspect has been exploited in this work by demonstrating amplification in F8BT over a ~ 50 nm wavelength range. Figure 6.5 shows the results of determining the wavelength dependence by measuring the change in the amplified output as a function of input wavelength. The amplifier demonstrates optical gain (as high as 40 dB in places) across a minimum wavelength range of 48 nm (524 – 582 nm). Note that the range is limited by the available output of the dye laser. The gap in the data (562 – 570 nm) is due to no appropriate laser dye being available in this wavelength range.

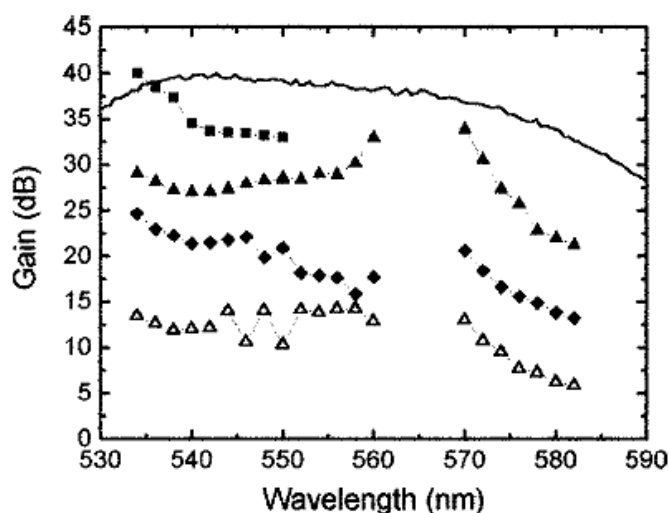


Figure 6.5: Demonstration of broadband gain as a function of wavelength for a range of polymer solution concentrations: 1.5 mg/ml (open triangles), 3 mg/ml (filled triangles), 3.5 mg/ml (filled squares) and 5 mg/ml (filled diamonds). The 8 nm gap in the data is due to no appropriate laser dyes being available. The solid line represents the spectral variation of the steady-state polymer PL. Figure taken from [8].

Finally in this section, the gain saturation characteristics of the F8BT polymer amplifier were deduced. Figure 6.6 shows the curve obtained for a solution concentration of 3 mg/ml at an input signal of $\lambda = 543$ nm along with the theoretical fit (solid line) deduced from the four-level laser model [9,10] given by equations 6.2 and 6.3 below.

$$G = \left(\frac{1}{S} \right) \ln [1 + G_0 (e^{(S)-1})] \quad [6.2]$$

$$S = \frac{E_{input} (\sigma_{abs} + \sigma_{se})}{Ah\nu_{input}} \quad [6.3]$$

In the above equations, G_0 is the small signal gain, E_{input} is the signal energy (per pulse), σ_{abs} and σ_{se} are the absorption and stimulated emission cross sections at the signal frequency ν_{input} , h is Planck's constant and A is the beam area.

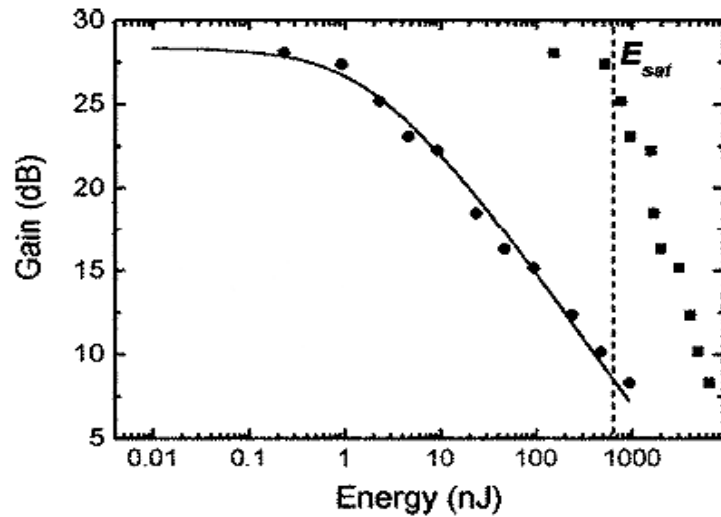


Figure 6.6: Gain saturation in the F8BT amplifier at a pump wavelength of 543 nm.

The experimental data is plotted along with a fit from equation 6.2 (solid line). The filled squares represent the dependence of the gain on the output signal. The dotted line shows the saturation energy of the amplifier. Figure taken from [8].

From the fit to the small signal gain, saturation energy and saturation energy density can be obtained for $\lambda = 543$ nm. These values are summarised in table 6.1 below. At this wavelength, if one assumed negligible absorption by the polymer (i.e. $\sigma_{abs} = 0$), then the stimulated emission cross-section σ_{se} can be estimated. Finally, the excitation density can be deduced through $g = \sigma_{se}N_{ex}$. Again, these values can be found in table 6.1.

Small signal gain (G_0) (dB)	Saturation energy (E_{sat}) (nJ)	Saturation energy density (mJ/cm^2)	Stimulated emission cross-section (σ_{se}) (cm^2)	Excitation density (N_{ex})
28.4 \pm 0.6	636	2.12	1.7 \pm 0.1 $\times 10^{-16}$	$\sim 3.8 \times 10^{-16}$

Table 6.1: Saturation characteristics for the F8BT polymer amplifier at a signal wavelength of $\lambda = 543$ nm.

The value of σ_{se} obtained here is comparable to that of polyparaphenylenevinylene ($1 \times 10^{-16} \text{ cm}^2$) [11] and to established laser dyes such as Rhodamine 6G and pyrromethene 650 ($\approx 3 \times 10^{-16} \text{ cm}^2$) [12]. It is slightly smaller than the value estimated from ASE measurements [13] on solid films ($7.1 \times 10^{-16} \text{ cm}^2$).

6.3 Saturated absorption in thin films of MEH-PPV

In the previous section, gain was demonstrated for a F8BT polymer amplifier along with the saturation characteristics, which are dependent upon the excited state density. An additional factor that should be considered is the impact of exciton annihilation in conjugated polymers, which acts to reduce the population of the excited state. In this section, the effect exciton-exciton (EE^*) annihilation has on the excited state density is explored using measurements of absorption saturation in thin films of MEH-PPV.

6.3.1 Experimental

The samples consisted of thin films of MEH-PPV (American Dye Source), which was spin-coated onto pre-cleaned silica substrates under cleanroom conditions. Solution concentration was 5 mg/ml in chlorobenzene. The spin speeds used were 1200 RPM, 2500 RPM and 5000 RPM giving three films of thickness 125, 80 and 60 nm respectively as calculated from the absorption spectra using an absorption coefficient for MEH-PPV of $1.86 \times 10^5 \text{ cm}^{-1}$ [14]. These films will subsequently be labelled a, b and c.

Absorption spectra were recorded for low excitation densities with a Cary 300 Bio UV-Vis spectrophotometer from Varian Incorporated. The saturated absorption experiment was performed using an open-aperture z-scan technique. The polymer film was scanned along the z-axis of the focussed pump beam in 250 μm intervals using the micrometer gauge on the translation stage. Samples were pumped using the focussed beam at $\lambda = 532 \text{ nm}$, of a frequency doubled passively Q-switched Nd:YVO₄ microchip

laser (Alphas GmbH). The laser provided 1 ns pulses at a frequency of 5 kHz. Calibrated neutral density filters were employed to attenuate the incident beam to an energy of 100 nJ/pulse. After passing through the MEH-PPV film, the beam was focussed to a spot size of less than 10 mm diameter (smaller than the collecting lens aperture of the fibre coupled CCD detector) to ensure all the transmitted light was collected by the CCD. A schematic of the experimental set-up is shown in figure 6.7. The radius of the pump laser at the beam waist had been previously measured to be 6 μm using a scanning knife-edge.

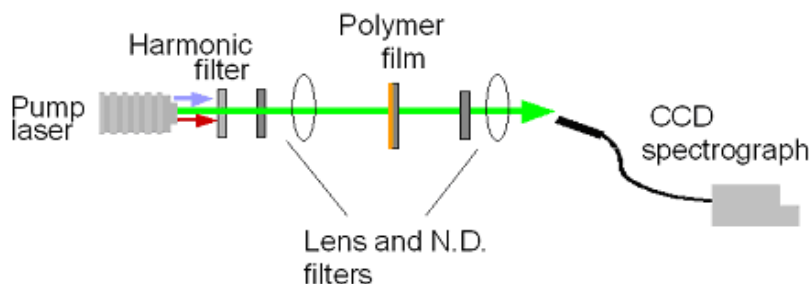


Figure 6.7: The experimental set-up for performing saturable absorption on films of MEH-PPV.

6.3.2 Results

The result of performing the z-scan experiment for the three polymer films is shown below in figure 6.8. The figure depicts the transmission intensity of the pump source through the sample as a function of the axial (z) position of the polymer film along the beam path. For each of the samples, the transmission through the film tends towards a background (unsaturated) level dependant upon the film thickness away from the high excitation density at the beam waist. As the sample moves through the beam waist, the excited state population becomes depleted due to the higher pump intensity

reducing the available gain. This gives a corresponding decrease in absorption by the film and manifests as a sharp increase in the transmission through the sample.

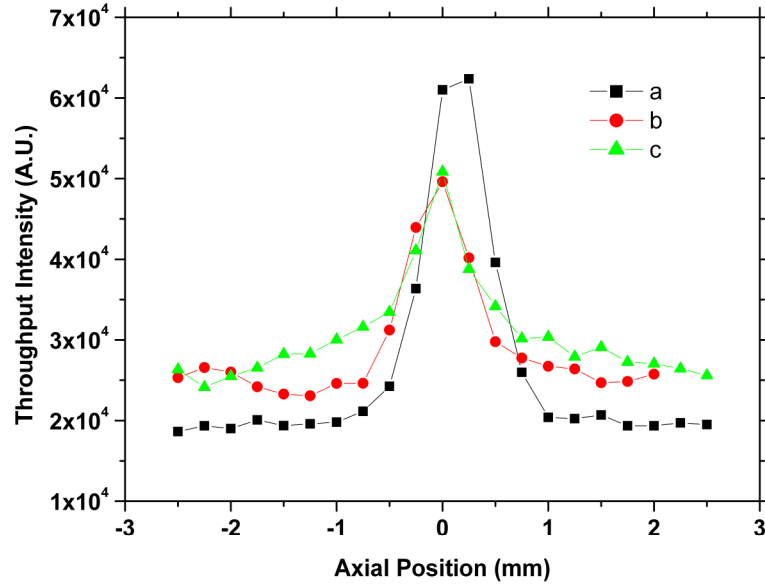


Figure 6.8: Transmission of the pump beam through films of MEH-PPV as a function of the axial position of the film along the beam path. The data presented is for films spin-coated at various speeds (1200, 2500 and 5000 RPM) in order to vary the thickness.

To develop the model for the saturated absorption incorporating EE^+ annihilation one must first consider the change in the intensity I of a beam as it passes through an absorbing medium of length L with ground state population N_l and absorption cross section σ .

$$\frac{1}{I} \frac{dI}{dz} = -\sigma N_l(I) \quad [6.4]$$

Upon grouping the variables prior to integration, we obtain equation 6.5.

$$\int_{I_{IN}}^{I_{OUT}} \frac{dI}{IN_l(I)} = \int_0^L \sigma dz \quad [6.5]$$

In order to evaluate the integral, we must first find an expression for N_1 , which is itself a function of the incident intensity. We start from the familiar rate equation for the change in population of the ground state N_1 with time, which is given in equation 6.6 below.

$$\frac{dN_1}{dt} = -\frac{N_1 I \sigma}{h\nu} + \frac{N_2}{\tau} + \gamma N_2^2 \quad [6.6]$$

The terms on the right hand side of the equation describe absorption of incoming photons promoting an atom from ground to excited state, spontaneous relaxation of an atom from the excited state back to the ground state (dependent on the excited state lifetime τ and the population N_2) and also a term describing the level of EE^\cdot annihilation in the polymer (γ). By substitution of expressions 6.7 and 6.8 for the saturation intensity I_{SAT} and for the degree of pumping above the saturation intensity X_{IN} , we can derive steady state equations for N_1 (6.9) and N_2 (6.10) for when $dN_1/dt = 0$.

$$I_{SAT} = \frac{h\nu}{\sigma\tau} \quad [6.7]$$

$$x_{IN} = \frac{I_{IN}}{I_{SAT}} \quad [6.8]$$

$$N_1 = N_T - \frac{1}{2\gamma\tau} \left[\sqrt{(x_{IN} + 1)^2 + 4\gamma\tau N_T x_{IN}} - (x_{IN} + 1) \right] \quad [6.9]$$

$$N_2 = \frac{1}{2\gamma\tau} \left[\sqrt{(x_{IN} + 1)^2 + 4\gamma\tau N_T x_{IN}} - (x_{IN} + 1) \right] \quad [6.10]$$

We can now substitute the expression for N_1 back into equation 6.5 and integrate (integration performed using the Mathematica package [15]). By taking the total population of the system (N_T) out of the integral as a factor, the integral is equated to the parameters $\sigma L N_T$ and is given in equation 6.11.

$$\sigma L N_T = \frac{-1}{2 \cdot (\gamma \cdot \tau \cdot N_T + 1)} \left[\left[\frac{I_{out} - I_{in}}{I_s} + \sqrt{\left(\frac{I_{out}}{I_s} + 1 \right)^2 + 4 \gamma \cdot \tau \cdot N_T \cdot \frac{I_{out}}{I_s}} - \sqrt{\left(\frac{I_{in}}{I_s} + 1 \right)^2 + 4 \gamma \cdot \tau \cdot N_T \cdot \frac{I_{in}}{I_s}} + \left[2 \cdot (\gamma \cdot \tau \cdot N_T + 1) \cdot \ln \left(\frac{I_{out}}{I_{in}} \right) \right] \right] \right. \\ \left. + (2 \gamma \cdot \tau \cdot N_T + 1) \cdot \ln \left[\frac{2 \gamma \cdot \tau \cdot N_T + 1 + \frac{I_{out}}{I_s} + \sqrt{\left(\frac{I_{out}}{I_s} + 1 \right)^2 + 4 \gamma \cdot \tau \cdot N_T \cdot \frac{I_{out}}{I_s}}}{2 \gamma \cdot \tau \cdot N_T + 1 + \frac{I_{in}}{I_s} + \sqrt{\left(\frac{I_{in}}{I_s} + 1 \right)^2 + 4 \gamma \cdot \tau \cdot N_T \cdot \frac{I_{in}}{I_s}}} \right] \right. \\ \left. - \ln \left[\frac{\left[(2 \gamma \cdot \tau \cdot N_T) + 1 \right] \cdot \frac{I_{out}}{I_s} + 1 + \sqrt{\left(\frac{I_{out}}{I_s} + 1 \right)^2 + 4 \gamma \cdot \tau \cdot N_T \cdot \frac{I_{out}}{I_s}}}{\left[(2 \gamma \cdot \tau \cdot N_T) + 1 \right] \cdot \frac{I_{in}}{I_s} + 1 + \sqrt{\left(\frac{I_{in}}{I_s} + 1 \right)^2 + 4 \gamma \cdot \tau \cdot N_T \cdot \frac{I_{in}}{I_s}}} \right] \right] \right]$$

Equation [6.11]

Finally, the equation for the transmission through the film T and hence the optical depth (O.D.) can be expressed in terms of these parameters (equation 6.12).

$$T = \exp(-\sigma L N_T) = 10^{-O.D.} \quad [6.12]$$

In order to fit the experimental data, absorption spectra were recorded for the three films at low excitation densities. These are shown in figure 6.9. Values for the unsaturated optical density at $\lambda = 532$ nm for each film were taken from the results. These were equated to the respective background counts recorded for each film during the z-scan experiment. The remaining values for the O.D. were calculated by normalising the data with respect to the background counts. The pump intensity I incident on the film at each position along the beam was calculated. For the experimental conditions, I_{SAT} was calculated to be 2 MW/cm^2 .

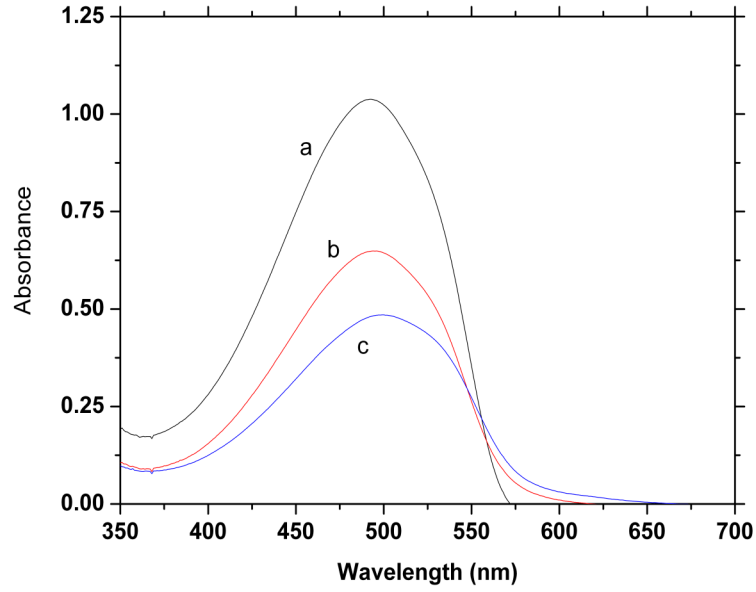


Figure 6.9: Absorption spectra for the three MEH-PPV films used in this experiment.

The model predicts how the optical density in the film changes as a function of the number of times one pumps above or below the saturation intensity. The degree of influence EE^- annihilation plays is controlled by the value of $\gamma\tau N_T$ where τ is the excited state lifetime, N_T is the total system population and γ is the EE^- annihilation rate in cm^3s^{-1} . The value of $\gamma\tau N_T$ can have a dramatic effect on the absorption saturation at higher pump intensities. This is illustrated below in figure 6.10 for values of $\gamma\tau N_T$ equal to 0 (no annihilation, panel a), 1 (panel b), 100 (c) and 750 (d). As one can see, as the rate of EE^- annihilation increases, the onset of absorption saturation moves to much higher intensities. A best fit of the model to the data was obtained when $\gamma\tau N_T = 25$. The result of which is shown below in figure 6.11.

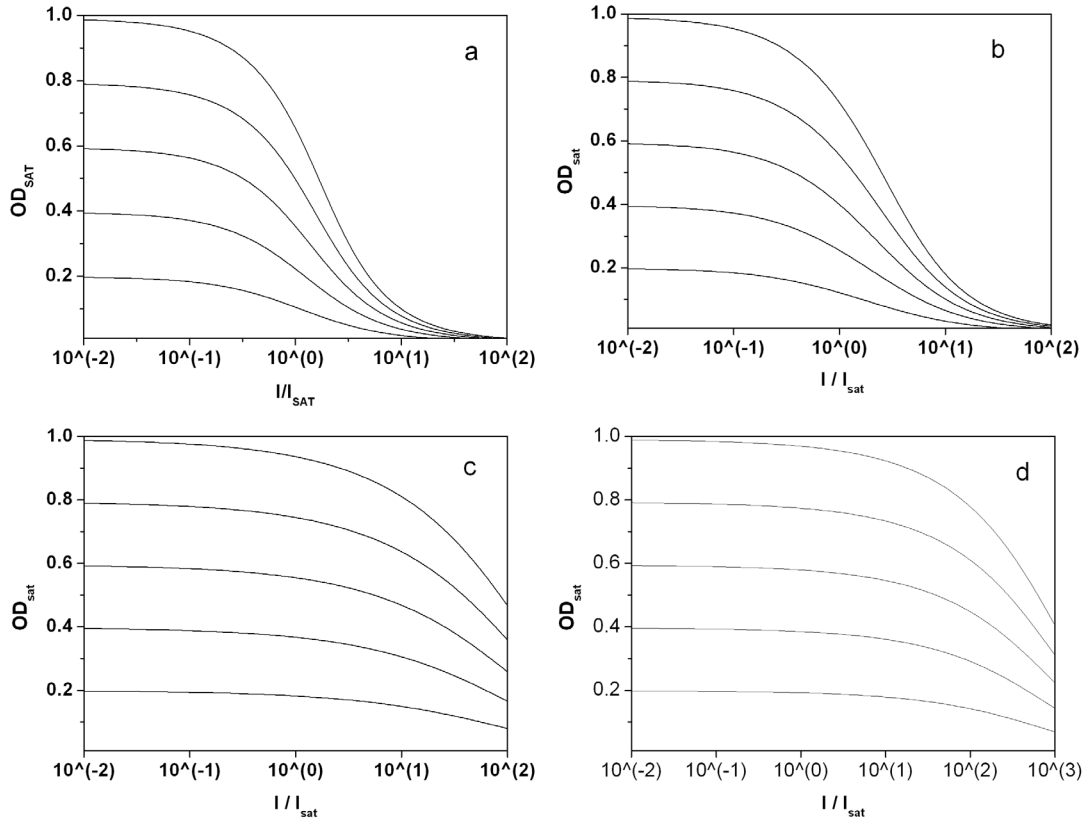


Figure 6.10: The effect EE^- annihilation has on optical density in thin films of MEH-PPV as the degree of pumping increases is shown for (a) $\gamma\tau N = 0$ (no EE^- annihilation), (b) $\gamma\tau N = 1$, (c) $\gamma\tau N = 100$ and (d) $\gamma\tau N = 750$.

From the value of $\gamma\tau N_T$ fitted to the experimental data, a value of the EE^- annihilation rate for MEH-PPV can be calculated. If we take values of $\tau = 250$ ps and $N_T = 10^{20}$ [16,17], this yields a value for $\gamma = 1 \times 10^{-9} \text{ cm}^3 \text{ s}^{-1}$. This is comparable to values calculated using ultrafast time-resolved luminescence measurements for F8BT ($1.5 \times 10^{-9} \text{ cm}^3 \text{ s}^{-1}$) [17] and P3HT ($3.4 \times 10^{-9} \text{ cm}^3 \text{ s}^{-1}$) [18]. It is however, a factor of 10 smaller than those calculated for MEH-PPV using this alternative approach which are typically of the order of $10^{-8} \text{ cm}^3 \text{ s}^{-1}$ [16-20]. This discrepancy may be due to the different excitation wavelengths used in the two experiments. For the time resolved approach, the excitation

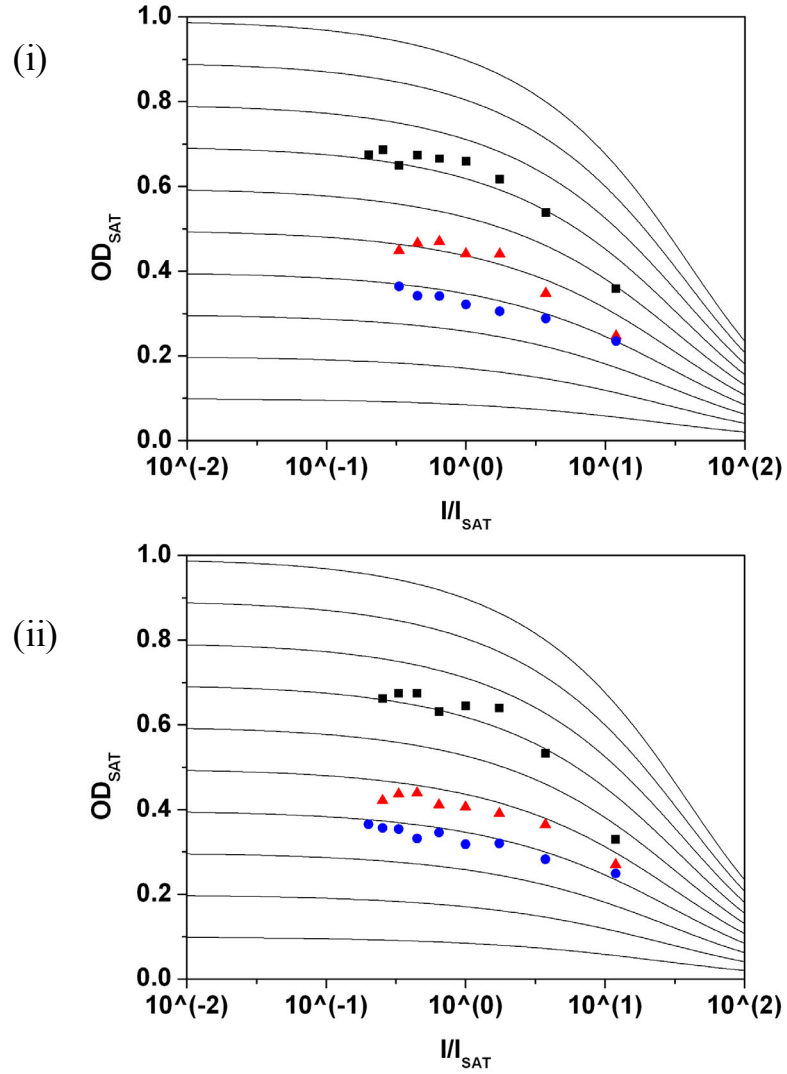


Figure 6.11: Fit of model (solid lines) when $\gamma\tau N_T = 25$ to the experimental data (points) obtained for films a (black squares), b (red triangles) and c (blue circles). The data in panels (i) and (ii) corresponds to scanning the sample towards the beam waist from the $+z$ and $-z$ directions respectively. As can be seen, there is a strong agreement between the experimental and modelled values.

wavelength is typically $\lambda = 400$ nm (where MEH-PPV absorption is weak) so that (in the case where films are not very thin) the exciton density is created uniformly across

the film. Here however, we are exciting at a lower energy ($\lambda = 532$ nm) and so the excitons may become trapped quicker on lower energy sites than for the case when exciting at 400 nm. This would impede the exciton diffusion, in turn leading to a reduced annihilation rate as the number of collisions between the excitons slows down. A similar behaviour was observed by Martini *et al.* [20] who found EE^- annihilation was more efficient for higher energy excitons which had not undergone energy transfer compared to thermalized excitons produced by energy migration.

Finally, we can calculate the excited state population N_2 at the front (pumped) interface as a function of number of times the pump intensity is above I_{SAT} for the parameters determined above. In a standard model, one would find that the population density increases linearly with increasing pump intensity until reaching a saturation point. In figure 6.12 below, we can see that the model incorporating the effect of EE^- annihilation follows the linear part of this curve at very low pump intensities ($I/I_{SAT} \approx 10^{-4} - 10^{-2}$). As the pump intensity increases however, we can clearly see the difference that EE^- annihilation makes in depleting the excited state population – and the potential impact this would have on exploiting the available gain. This study underpins the importance of this effect and the requirement for understanding the role exciton migration and annihilation plays in photophysical aspects of conjugated polymers.

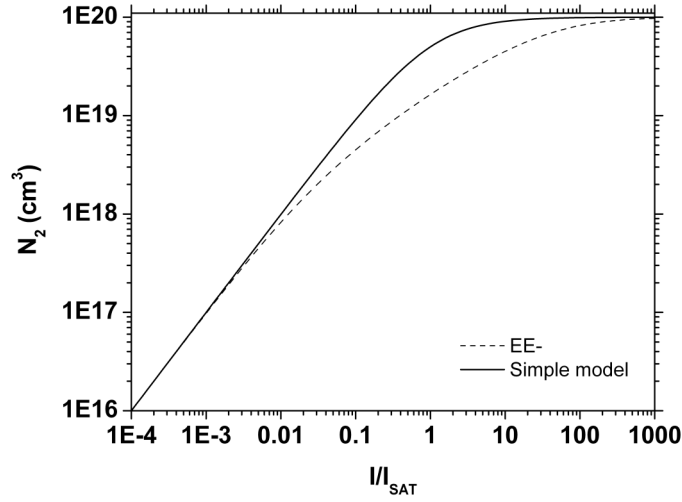


Figure 6.12: Variation in the excited state population as the pump intensity increases above saturation intensity with (dotted curve) and without (solid curve) the effect of EE^- annihilation. While at low intensities, the two models are virtually identical, EE^- annihilation plays an increasingly important role in the depletion of the N_2 population as we move to higher pump intensities.

6.4 Summary

In this chapter, transitions in conjugated polymer films while undergoing intense optical excitation were explored. These included the demonstration of gain from a solution based F8BT polymer amplifier and how absorption is saturated at high pump intensities in thin films of MEH-PPV by incorporating exciton-exciton annihilation effects into the model study.

For the F8BT solution amplifier, a range of concentrations were tested resulting in the demonstration of a large (≤ 40 dB/cm) amplification of a weak probe beam across a spectral range of almost 50 nm. At a wavelength of $\lambda = 543$ nm, the model fit to the data

yielded a small signal gain of 28.4 dB and a saturation energy of 636 nJ. The overlap of the gain bandwidth with the transmission window for polymer optical fibres such as PMMA shows great promise for establishing a suitable amplifying medium compatible with such materials. For a F8BT solution concentration of 3 mg/ml, the stimulated emission cross section was estimated to be $1.7 \pm 0.1 \times 10^{-16} \text{ cm}^2$ which is comparable with other conjugated polymers and established laser dyes.

A study of saturated absorption in thin films of MEH-PPV was also presented. Configured as an open-aperture z-scanning experiment, the MEH-PPV film was exposed to varying pump intensities. By modelling the transmission through the film incorporating terms describing the rate of exciton-exciton annihilation present (which reduces the available excited state population) a value of $1 \times 10^{-9} \text{ cm}^3 \text{ s}^{-1}$ for the annihilation rate was calculated. This value is similar to values calculated in F8BT and P3HT and slightly slower than the rate measured in MEH-PPV using time-resolved photoluminescence methods. This is attributed to the difference in excitation wavelength used ($\lambda = 532 \text{ nm}$ in this work compared to $\lambda = 400 \text{ nm}$ in the time-resolved work) which excites lower energy chromophores in the MEH-PPV film. The result is a reduced collision rate due to the excitons having lower energy.

6.5 References

- [1] O. Svelto, *Principles of Lasers (4th Edition)*, Plenum Press, New York (1998).
- [2] G.D. Khoe, *IEEE J. Sel. Top. Quantum Electron.*, **6**, 1265 (2000).
- [3] T.I. Monroy, H. Boom, A.M.J. Koonen, G.D. Khoe, Y. Watanbe, Y. Koike and T. Ishigure, *Opt.Fibre.Technol.*, **9**, 159 (2003).
- [4] M.D. McGehee and A.J. Heeger, *Advanced Materials*, **12**, 1655 (2000).
- [5] N. Tessler, *Advanced Materials*, **11**, 363 (1999).
- [6] J.R. Lawrence, G.A. Turnbull and I.D.W. Samuel, *Applied Physics Letters*, **80**, 3036 (2002).
- [7] R. Xia, G. Heliotis, Y.B. Hou and D.D.C. Bradley, *Organic Electronics*, **4**, 165 (2003).
- [8] G. Heliotis, D.D.C. Bradley, M. Goossens, S. Richardson, G.A. Turnbull and I.D.W.Samuel, *Applied Physics Letters*, **85**, 6122 (2004).
- [9] S. Scimada and H. Ishio, *Optical Amplifiers and their Applications*, Wiley, 1994.
- [10] T.L. Koch, L.C. Chin and A. Yariv, *Journal of Applied Physics*, **53**, 6047 (1982).
- [11] W. Holzer, A. Penzkofer, S.H. Gong, A. Bleyer and D.D.C. Bradley, *Advanced Materials*, **8**, 974 (1996).
- [12] W. Holzer, M. Pichlmaier, A. Penzkofer, D.D.C. Bradley and W.J. Blau, *Chemical Physics*, **246**, 445 (1999).
- [13] S.Y. Lam and M.J. Damzen, *Appl. Phys B: Lasers Opt.*, **77**, 577 (2003).
- [14] O. Gaudin, Private Communication.

- [15] Wolfram Research Inc., Mathematica, Version 4, Champaign, IL, (1999).
- [16] A. Ruseckas, Private Communication.
- [17] P.E. Shaw, Private Communication.
- [18] P.E. Shaw, A. Ruseckas and I.D.W. Samuel, *American Chemical Society Proceedings (Polymer Pre-prints)* (2007).
- [19] A.J. Lewis, A. Ruseckas, O.P.M. Gaudin, G.R. Webster, P.L. Burn and I.D.W. Samuel, *Organic Electronics*, **7**, 452 (2006).
- [20] I.B. Martini, A.D. Smith and B.J. Schwartz, *Physical Review B*, **69** (2004).

Chapter 7: Dendrimer Lasers

I would like to thank Dr. Paul Burn, Dr. Homar Barcena and the rest of the Advanced Organic Materials Group for the work conducted at the University of Oxford in synthesising the dendrimer materials used in this thesis. Without the supply of these innovative molecules, this work would not have been possible.

7.1 Introduction

The ability to solution process organic light-emitting polymers is highly desirable in order to provide the flexibility required for the cheap fabrication of devices. To this end, the potential of many derivatives of poly(phenylene-vinylene) (PPV) has been demonstrated in the literature [1-5]. Initially, the emission from PPV was in the green [6] and later, by synthesising the polymer with interrupted conjugation, in the blue-green part of the spectrum [7].

Development of blue emitting polymers followed shortly afterwards with studies initially looking at high-bandgap materials such as poly-(vinyl-carbazole) (PVK) [8,9] and poly-*para*-phenyl (PPP) [10,11]. Despite finding widespread use as charge transporting hosts [12-15] there are several drawbacks to these materials. Emission is intrinsically in the UV-blue and inefficient. PPP is also largely insoluble in many organic solvents and processing requires formation from the precursor method. It was the introduction of poly(fluorene) (PFO) [16] and its derivatives that helped pave the way for greater study into the realm of blue emitting polymers. In PFO, the addition of a carbon atom to fuse two adjacent PPP phenyl groups provides greater rigidity and allows the possible addition of solubilising groups without affecting the emission

properties. Many recent publications [17-21] have demonstrated stable, efficient devices fabricated from PFO.

A major issue with photoluminescence from polymer films is the tendency to form low energy aggregates or excimers [22] resulting in red-shifted spectra. As a result, what is often observed is blue-green emission, rather than blue. Grafting side chains onto the backbone can counteract this issue [23], but can also change the emission wavelength. A more elegant solution would be to disengage the chemical and emissive properties of the molecule from its solubility.

The scientific community has used organic semiconducting polymers and small molecular compounds for many years now. More recently however, a third class of materials with highly interesting properties have been introduced. Semiconducting dendrimers are branched, snowflake like molecules which can be specifically engineered to have properties such as colour control and solubility tailored to the task at hand. In the relatively short space of time since their introduction, dendrimer materials have given rise to a number of successful reports in the literature such as highly efficient solution processed light emitting diodes [24-26].

In this chapter, work conducted using solution processed dendrimer devices will be presented. Initially, the concept of dendrimer materials will be introduced with the building blocks essential to their function. I will then continue in presenting a comparison of different dendrimer molecules and blends with small molecules with the aim of investigating the potential of novel materials as laser sources. An application for one such dendrimer laser source will be discussed, the ability to conduct detection of nitro-benzene vapour, a forerunner to the realisation of a compact explosives detector. Finally, solvent assisted micromoulding is performed on dendrimer films and the results

compared to those recorded for polymers, highlighting the potential benefits of dendrimer materials when applying this soft lithographic technique.

7.2 The dendrimer concept

The ability to solution process organic materials is more attractive than the traditional method of depositing small organic compounds by evaporation due to the potential advantages of printing and patterning the active layer as well as obvious manufacturing benefits such as reduced cost. However, conjugated polymers are often harder to purify than small molecular compounds, due in part to the synthesis process giving a distribution of molecular weights (polydispersity). This, coupled with different processing conditions [27] and hence, polymer conformations, can instil a variety of optical and electronic properties in the material. The ability to incrementally control subtle changes to the structure of a conjugated material is therefore vitally important to the continued development of novel compounds.

An initial study of light-emitting dendrimers was successfully performed by Halim *et al.* [28] and bridges the gap between small molecules and polymers offering benefits from both classes of material. Dendrimers possess highly branched dendrons, connecting a central core to surface groups. A schematic of this geometry is depicted in figure 7.1.

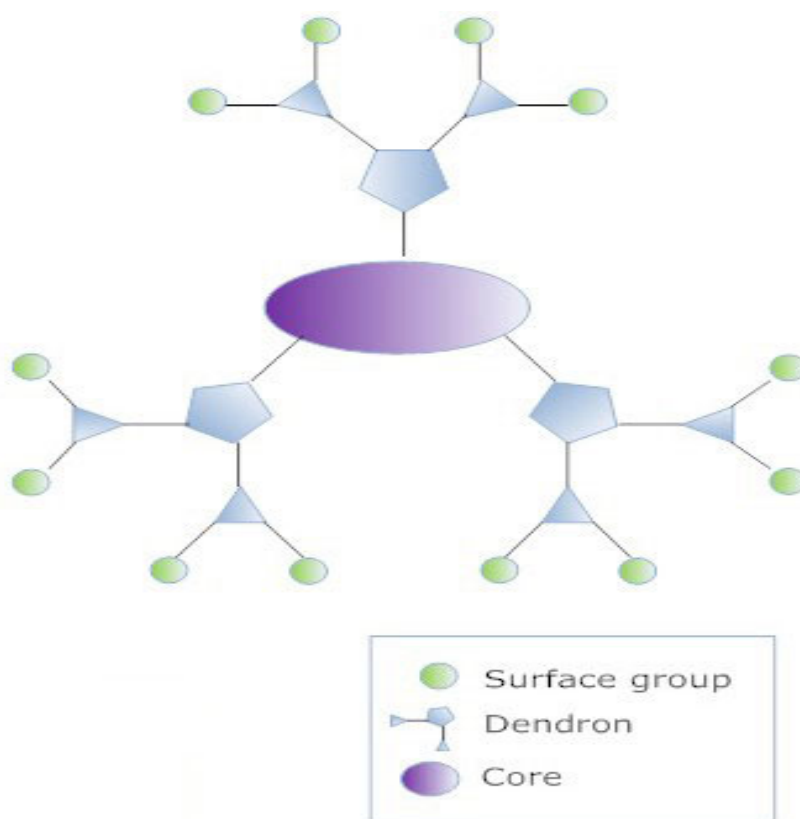


Figure 7.1: Schematic representation of a first generation dendrimer molecule displaying the core, dendron and surface groups.

The core resides at the centre of the molecule and is responsible for the electronic properties of the material such as the colour of the light emission. Dendrons are then attached to the core. This is done in such a way as not to alter the core electronic properties. Conjugation between the core and the dendrons can be maintained (redshifting the emission or the absorption) or can be broken as is the case with the iridium-based dendrimer IrG1. The generation of the dendrimer is defined as the number of branching levels extending from the core. By increasing the generation of the dendrimer or adding more dendrons, one can increase or decrease the separation between cores accurately on the nanometre scale. This can control the level of shielding

the core region receives from intermolecular interactions – leading to improved colour purity or emission efficiency and control over charge transport [29]. Finally, surface groups are attached to the ends of the dendrons on the outside of the molecule and define the solubility and processing properties.

The advantage of utilising this architecture is the ability to independently tune the electronic and processing properties of an individual molecule. Colour tuning has been demonstrated in the fabrication of OLEDs in the blue, green and red by changing the core chromophore under identical processing conditions [30]. This flexibility allows enormous scope for engineering molecules to cover the entire visible spectrum. Control of the processing properties through the surface groups lowers the risk of phase separation when blended with other materials and thus introduces the prospect of further tuning these materials to one's benefit. In the next section, a range of blue-emitting dendrimer materials along with dendrimer blends have been tested to establish their performance and potential for compact solid-state laser sources, compared to their polymer counterparts.

7.3 Materials for dendrimer lasers

The potential of dendrimers in their numerous guises in the past has usually been successfully demonstrated in the development of OLED devices [24,25]. Green electrophosphorescent materials such as the Iridium cored complex have shown exceptional performance in this configuration with external quantum efficiencies as high as 16% [28]. However, forbidden transitions make these materials particularly unsuitable for high-gain laser applications. Dendrimers do have the potential for amplifiers and semiconductor lasers [31-33] but require fluorescent-cored materials.

Previous work has shown gain in both solution and thin films of a bisfluorene dendrimer [34] whereas other recent work has demonstrated a DFB laser based on a second generation bisfluorene-cored dendrimer that had a threshold of 60 nJ/pulse as well as a high slope efficiency of 14% (for emission in both directions) [35]. Amplified spontaneous emission experiments performed on the various bisfluorene cored dendrimers [36] have shown that the biphenyl (see next section for the chemical structure of all the dendron types) dendron material exhibits the best performance in the solid state, compared to that of the biphenylcarbazole and E-stilbenyl materials (16 $\mu\text{J}/\text{cm}^2$ verses 50 $\mu\text{J}/\text{cm}^2$ and 25 $\mu\text{J}/\text{cm}^2$ respectively). For comparison, the ASE threshold of poly(9,9-dioctylfluorene) (PFO) is reported as 29 $\mu\text{J}/\text{cm}^2$ [20]. Thus, the biphenyl dendron material could be considered a better candidate for fabricating an efficient DFB device. Clearly, characterisation of new, innovative dendrimer materials utilising the fluorescent bisfluorene core are essential for the continued development of successful laser devices.

In this section, a number of neat and blended films using bisfluorene dendrimers are configured as 2D distributed feedback lasers to explore the effect variations in the dendron structure and film thickness has on the emission. The lasers are characterised for threshold and slope efficiency. The most promising of the compounds is then optimised with demonstration of tuning the emission wavelength over a range of 20 nm by varying the film thickness.

7.3.1 Experimental

In figure 7.2 shown below, the chemical structures of the four bisfluorene cored dendrimers used in this study are shown. The dendrons attached to the 7- position of the fluorenyl group in the bisfluorene cores are biphenyl (BP – structure 1), biphenylcarbazole (BPCz – structure 2), E-stilbenyl (ES – structure 3) and diphenylethane (DPE – structure 4).

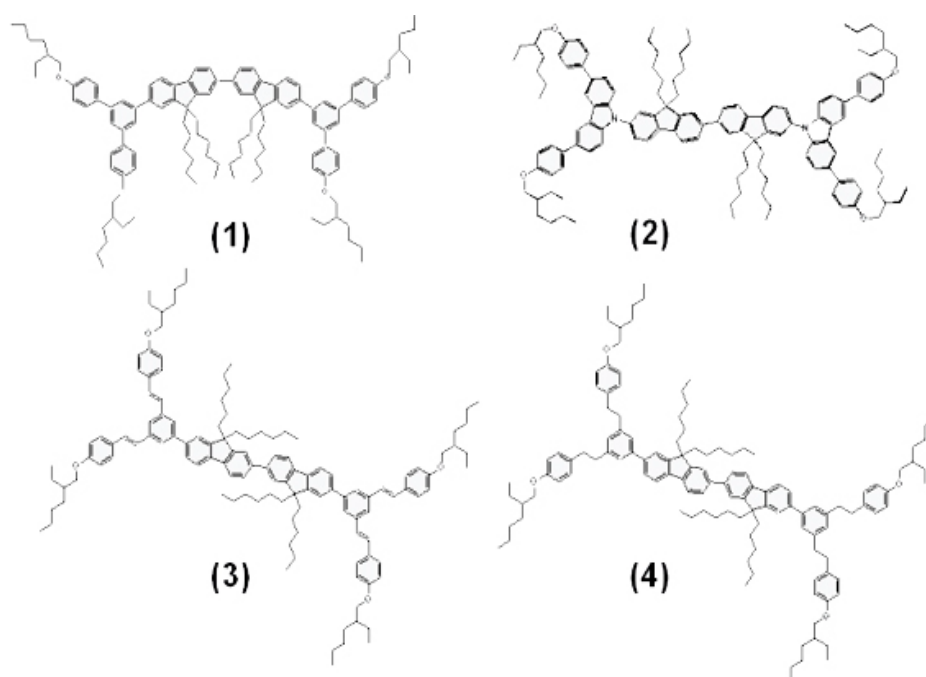


Figure 7.2: The chemical structures of bisfluorene cored dendrimers containing the following dendrons: (1) biphenyl (2) biphenylcarbazole (3) E-stilbenyl and (4) diphenylethane.

The dendrimer films was fabricated in clean room conditions from chloroform solutions (typical concentration 25 mg / ml) by spin-casting onto a pre-cleaned corrugated substrate of period $\Lambda = 260$ nm in both directions. The corrugation was formed by holography and reactive ion etching, and had a depth of approximately 30 nm. An AFM

image of the substrate is shown in figure 7.3. The spin-speed ranged between 1000 and 1500 RPM and gave dendrimer films of varying thickness in the range of $\sim 200 - 220$ nm (measured by ellipsometry).

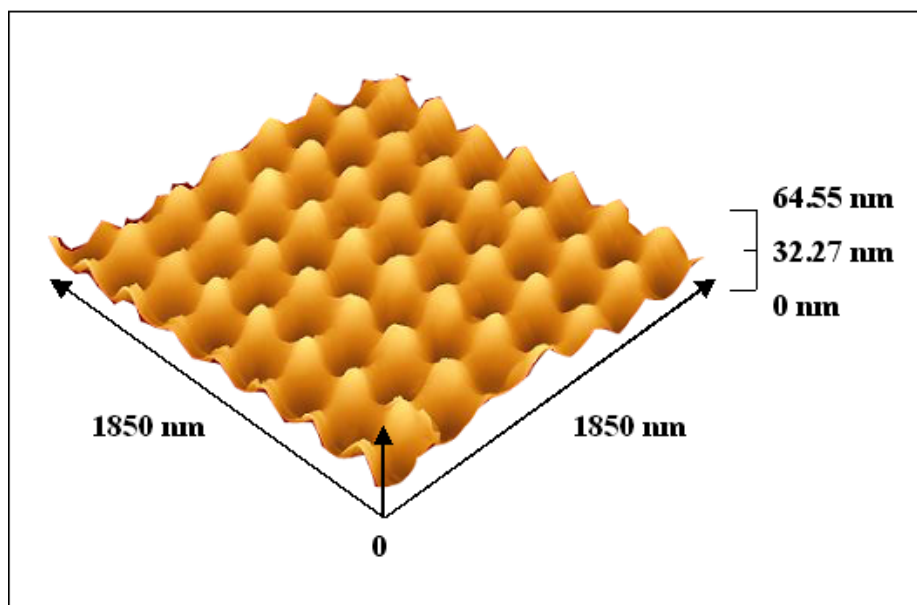


Figure 7.3: AFM image of corrugated silica grating used to fabricate 2-D DFB dendrimer lasers. Periodicity is approximately 260 nm in both directions and depth ≈ 30 nm.

Photoluminescence spectra were recorded using a Jobin Yvon Fluoromax 2 spectrometer, absorption measurements were performed with a Cary 300 Bio UV-Vis spectrophotometer from Varian Inc. PLQY measurements were made using an integrating sphere under a nitrogen atmosphere as described in chapter 3. Samples were excited using the output of a CW He-Cd laser from Kimmon ($\lambda = 325$ nm, excitation power = 0.15 mW).

Dendrimer lasers were characterised by optically pumping the films using the third harmonic of a passively Q-switched Nd:YVO₄ microchip laser ($\lambda = 355$ nm, 1 ns

pulses, 5 kHz). The pump beam was focussed to a stripe with dimensions of 650 μm x 200 μm and was incident on the device at a slight angle ($\approx 10^\circ$). Emission was detected close to the normal using a fibre-coupled CCD spectrometer of resolution = 0.6 nm. To reduce oxidation and photodegradation, films were characterised in a vacuum chamber with a pressure lower than 10^{-4} mbar. This section of work was performed in collaboration with Dr. Jean-Charles Ribierre from the University of St. Andrews who provided the dendrimer materials and fabricated the laser samples prior to characterisation.

7.3.2 Results

The absorption (black curve) and photoluminescence (red curve) spectra for the four different dendron types are given below in figure 7.4. The spectra have been normalised with reference to their maximum peak value. PLQY values and the location of the ASE peak for the materials are contained within table 7.1.

The absorption feature centred at 350 nm is due to the bisfluorene core present in all materials. The broader nature of the BPCz and ES absorption spectra is due to the strong absorption of the dendrons between 300 nm and 380 nm [37]. The emission properties of the BP, ES and DPE dendrimers are very similar, each showing 2 vibronic peaks and 1 shoulder. Photoluminescence from the BPCz dendrimer is slightly redshifted (~ 10 nm), with a less defined vibronic structure. This redshift is mirrored in the absorption spectrum of this material and is due to carbazole moieties in the conjugation structure.

The role of the 4,4'-N,N'-dicarbazole-biphenyl (CBP) host in the dendrimer blends studied here varied for the dendron type. For the BPCz and ES dendrimers, CBP

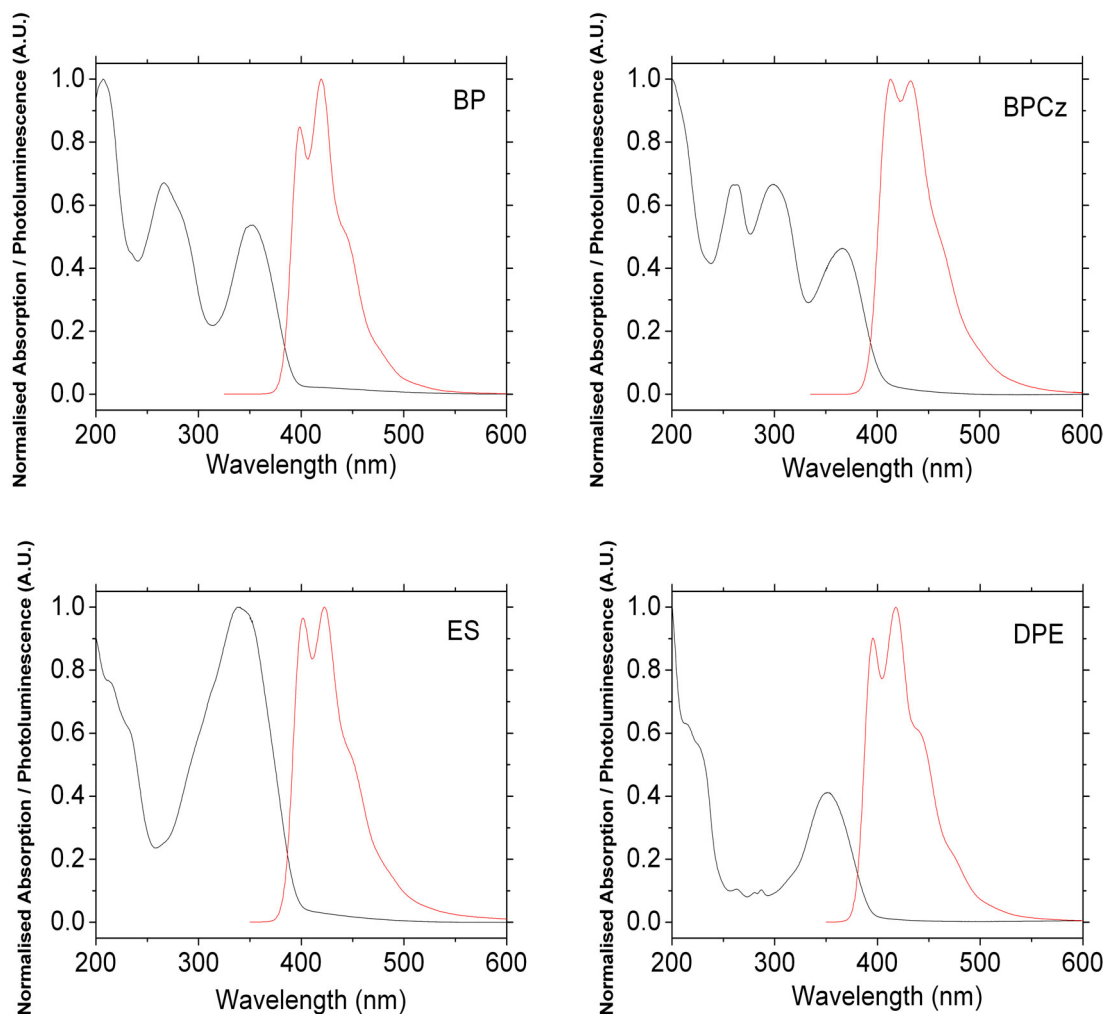


Figure 7.4: Normalised absorption and PL emission spectra for bisfluorene cored dendrimers with BP, BPCz, ES and DPE dendron units.

	BP dendron (1)	BPCz dendron (2)	ES dendron (3)	DPE dendron (4)
PLQY (%)	92	43	52	89
λ_{ASE} (nm)	421	431	422	-

Table 7.1: Photoluminescence quantum yield values for bisfluorene cored dendrimers with varying dendron types. The wavelength at which spectral narrowing (amplification) occurs in each of the materials is also displayed [36].

acts to reduce concentration quenching in the material by spacing the cores. For the DPE dendrimer, the neat solution forms very poor gel like films and so a CBP host is used to improve film quality from spin coating.

Lasing results for the bisfluorene dendrimers using the BPCz, ES and DPE dendrons are summarised below in table 7.2 along with the processing conditions. Solution concentrations for the BPCz and DPE dendrimer films were 25 mg / ml. The concentration of the solution containing the E-Stilbenyl dendron material was 20 mg / ml. The solutions containing the BPCz and ES dendrimer / CBP blends were mixed in a ratio of 1 part dendrimer to 4 parts CBP by weight. The ratio of the DPE / CBP blend was 1 part dendrimer to 1 part CBP.

Material	Spin Speed (RPM)	$\lambda_{\text{emission}}$ (nm)	Threshold (nJ)	Slope Efficiency
BPCz	800	421	125	0.4 %
BPCz : CBP	1500	431	48	0.3 %
ES	1000	417	39	0.1 %
ES : CBP	1500	414	28	1 %
DPE : CBP	1500	424	11	2.5 %

Table 7.2: Summary of lasing properties for bisfluorene cored dendrimers using the BPCz and ES dendron structures.

Devices containing the blend between the BPCz and ES dendrimers with the CBP host to reduce concentration quenching perform as expected compared to the respective neat films. Both show a reduction in the threshold value. The efficiency of the BPCz : CBP sample is largely unchanged (slight reduction from 0.4 % to 0.3 %) while the efficiency of the ES : CBP device increases by an order of magnitude.

The threshold and efficiency for the DPE device (11 nJ / pulse and 2.5% respectively) are significantly better than the results for the other samples. This is most likely due to the material having a much higher PLQY (89% compared to 43% for the BPCz dendron material and 52% for the ES material). The BPCz devices (both neat film and CBP blend) had emission wavelengths which were red-shifted compared to the ES and BP dendron devices for the same processing conditions. This is consistent with the red-shifted photoluminescence spectrum shown in figure 7.4, a result of the carbazole groups in the dendrimer structure. Emission spectra for these 5 devices operating above threshold can be seen below in figure 7.5, demonstrating the potential for tuning the wavelength through subtle variations in the choice of dendron and also by varying the film thickness. Efficiency curves for the same devices are given in figure 7.6.

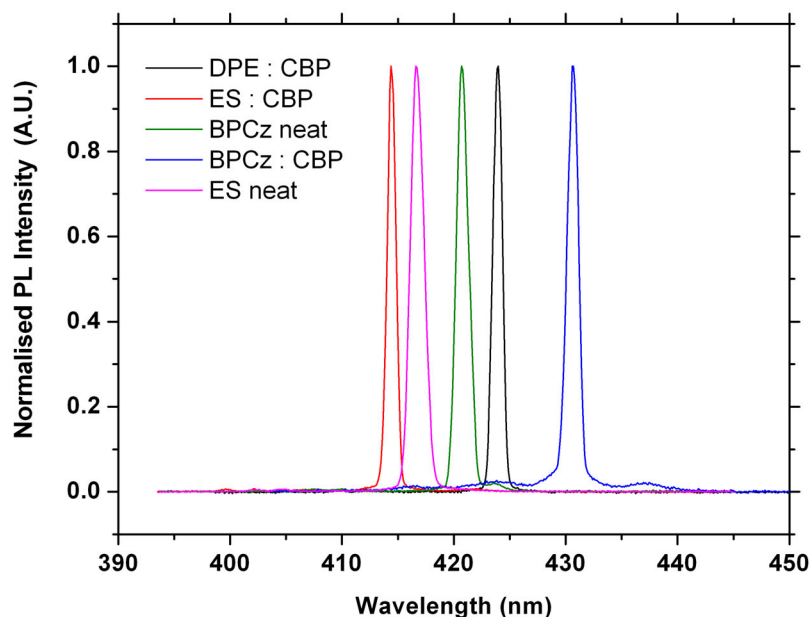


Figure 7.5: Emission spectra for the dendrimer lasers described in table 7.2 when operating above threshold.

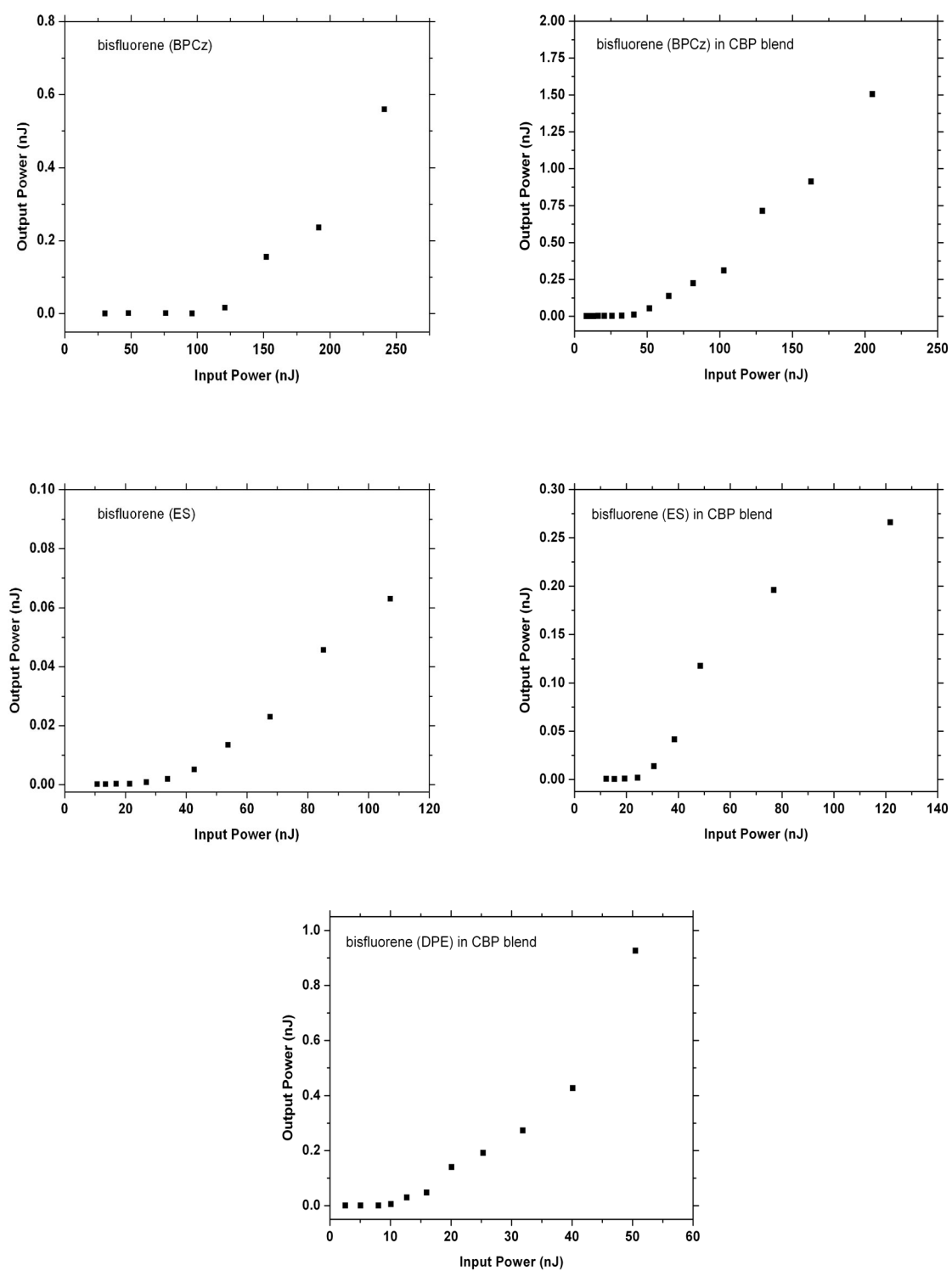


Figure 7.6: Laser power efficiency curves for bisfluorene dendrimers (BPCz, ES and DPE dendrons) and blends with CBP host.

Previous work by Otomo *et al.* [38] on a 2-D DFB structure using BP dendrimer as a gain medium reported a lasing threshold of 90 nJ/pulse and a slope efficiency of 0.3%. However, it should be noted that the emission wavelength of this device was 408 nm, well away from the ASE peak as reported by Ribierre *et al.* [36]. Thus, in order to improve the efficiency, three devices were fabricated with film thickness ranging from 200 to 220 nm. As a result, the emission wavelength was finely tuned from 412 to 427 nm as shown below in figure 7.8. A summary of lasing properties for device 1 (green curve), device 2 (red curve) and device 3 (black curve) can be found below in table 7.3. A photograph of lasing from a BP dendrimer device is shown below in figure 7.7. The 2-D nature of the feedback can be clearly seen in the emission pattern.

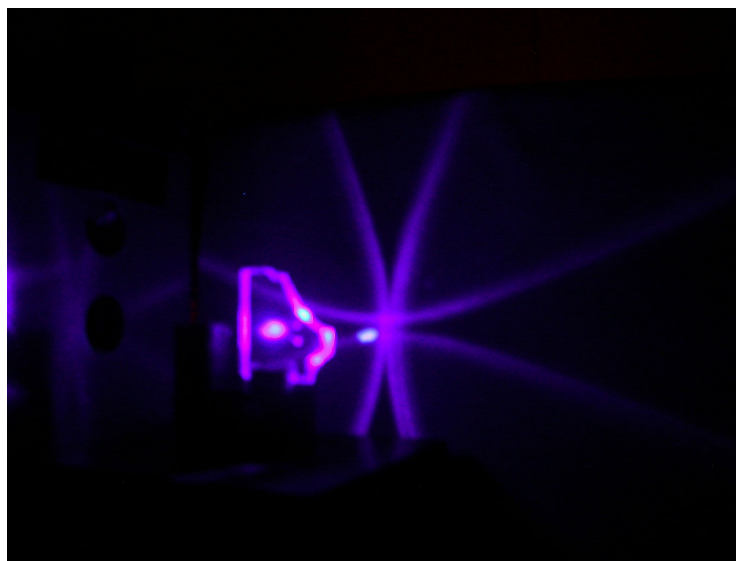


Figure 7.7: Photograph of lasing emission from a thin film of a bisfluorene cored dendrimer (biphenyl dendrons), spin-cast onto a corrugated fused silica substrate. The emission wavelength of this device is 407 nm.

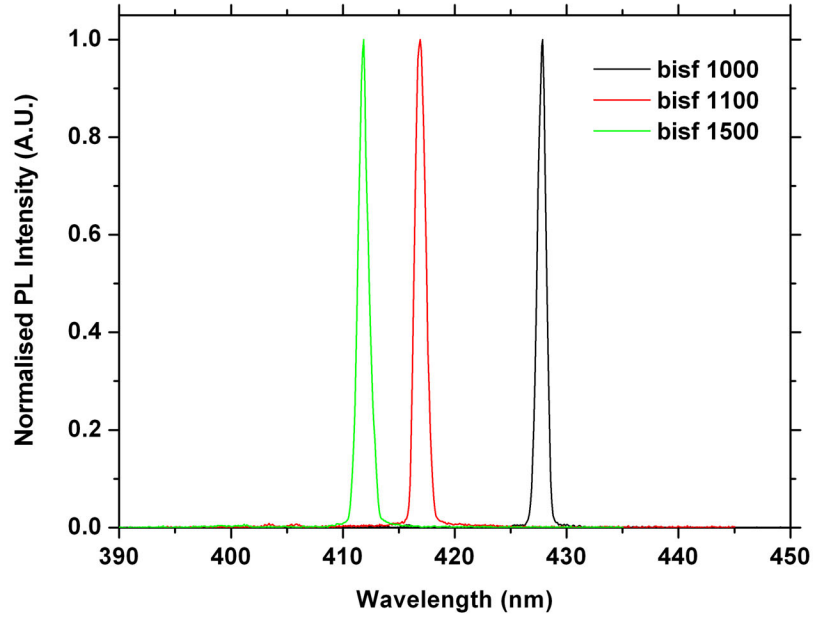


Figure 7.8: *Tuning the emission wavelength of BP dendrimer lasers by varying only the film thickness.*

	Spin Speed (RPM)	$\lambda_{\text{emission}}$ (nm)	Threshold (nJ)	Slope efficiency
Device 1	1500	412	240	0.05 %
Device 2	1100	418	6	8.3 %
Device 3	1000	427	11	4 %

Table 7.3: *Summary of lasing properties for films of bisfluorene dendrimers (BP dendrons) of varying thickness.*

Device 2 (emission wavelength $\lambda = 418$ nm) was found to have a threshold of 6 nJ/pulse. This equates to an excitation density of $4.5 \mu\text{J}/\text{cm}^2$. The slope efficiency of device 2 was 8.3 %, measured on one side through the substrate. These figures compare well to values reported for a PFO laser emitting at 454 nm [39] ($4 \mu\text{J}/\text{cm}^2$ and 7.8 %

efficiency, measured on both sides), demonstrating the quality of our bisfluorene laser. The increased efficiency of the BP dendron laser versus the other dendrimers is most likely a result of the high PLQY of the material. The net gain of the material in terms of the PLQY is expressed in equation 7.1. Here, σ is the stimulated emission cross-section ($3.4 \times 10^{-18} \text{ cm}^2$ [34]), P is the pumping rate, Φ is the PLQY value and k_R is the radiative decay rate ($1.28 \times 10^9 \text{ s}^{-1}$ [40]). The calculated values for the BP dendron material are in excellent agreement with the ASE experimental data reported in [36] which notes that an anti-correlation between the PLQY and the waveguide loss suggests dendrons that reduce the level of crystallinity in the material are most useful for designing efficient dendrimer lasers. The power efficiency curves for all three of the biphenyl dendron devices are shown below in figure 7.9.

$$g = \frac{\sigma P \Phi}{k_r} - \alpha \quad [7.1]$$

Laser devices 1 and 3 (dendrimer films deposited at spin speeds of 1500 RPM and 1000 RPM respectively) have higher thresholds of 240 and 11 nJ along with lower power efficiencies of 0.05% and 4%. The reason for this is that the energy required for lasing increases rapidly as the emission moves away from the centre of the gain spectrum. This is more pronounced on the short wavelength side due to the additional losses from self-absorption. Overall, the results demonstrate the excellent prospects for efficient DFB laser devices using dendrimer materials as the gain medium.

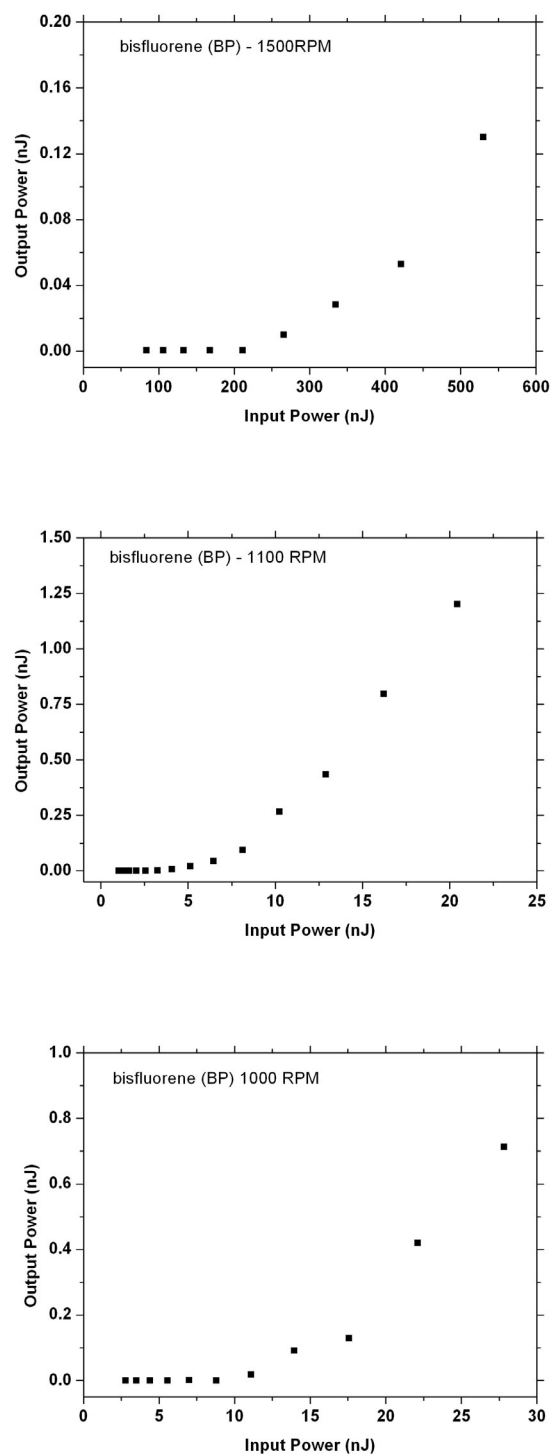


Figure 7.9: Laser power efficiency curves for devices fabricated from thin films of bisfluorene (BP dendron) of varying thickness.

7.4 Explosives detection through dendrimer lasers

Nature often provides us with the guidance needed for developing new technologies. Many species in the animal kingdom can detect chemical signals with astounding specificity and sensitivity. The understanding of the roles and interactions between components such as delivery and removal mechanisms will play an important part in the fabrication of artificial sensory devices.

Conjugated polymers are ideal materials to take advantage of the need for such chemical and biological sensors [41,42]. They exhibit changes in electrical conductivity in response to interactions with external materials [43,44], which can easily be magnified by doping the polymer [45]. An alternative method for fabricating a sensor is to use changes in chemical potential of the polymer. These potentiometric devices use variations to the work function of the material to affect the transport characteristics [46]. The ability of conjugated polymers to fluoresce and amplify light offer a number of sensing schemes based upon changes in intensity, emission wavelength and operational lifetime. This particular trait has been exploited with great success on several occasions [46,47].

While there are a great number of applications for conjugated polymer based sensors [41], one of the recent success stories for these materials is the ability of thin films to act as trace-detectors of explosive vapour signatures [47,49-50]. The electron rich structure of the polymer entices electron deficient, acidic nitroaromatics to bind to the polymer surface. Emission is quickly quenched as excitons, diffusing throughout the polymer encounter the nitro groups instead. These non-radiative deactivation pathways

compete with the stimulated emission from the organic semiconductor [47] and result in an observable drop in output from the device.

In this section, I demonstrate that a bisfluorene cored dendrimer with biphenyl dendrons can act as a trace detector for explosive vapour. When configured as a distributed feedback laser, dramatic increases in sensitivity can be obtained when compared to the photoluminescence output from the film.

7.4.1 Experimental

The bisfluorene dendrimer with BP dendrons was used to form the active layer of the devices. This was based on the previous results from section 7.3.2, where it had outperformed the other available dendrimers while undergoing laser operation. Under clean room conditions, thin films of bisfluorene were spun from solution (25 mg / ml concentration in chloroform) onto the pre-etched silica grating used in the previous section which had a period of 260 nm and a depth of approximately 30 nm (see figure 7.3). Devices were transferred for testing immediately after fabrication.

For the laser testing, a nitrogen laser pump source emitting at 337 nm was used. Frequency was 10 Hz and the pump power was attenuated as necessary using calibrated neutral density filters. The output from the dendrimer film was measured close to normal incidence using a fibre coupled CCD spectrometer (Triax 180, J.Y. Horiba).

After initial characterisation, the dendrimer film would be exposed to di-nitrobenzene (DNB) vapour. The film would be placed in close proximity, but not in contact with a small tray containing ~ 10 mg of DNB crystals. An inverted beaker was used to restrict the volume of the set-up while the atmosphere was allowed to saturate with the DNB vapour. Once a time period of one hour had passed, the film was

removed from the beaker and a second laser characterisation of the dendrimer film would begin.

7.4.2 Results

It is well known that conjugated polymers react poorly with air when operating in ambient conditions - leading to a decrease of performance. Such effects were demonstrated earlier (see chapter 5 for more details on encapsulated and unencapsulated lasers) in this work where conjugated polymers decayed upon exposure to oxygen resulting in a degradation of their ability to perform as lasers. As the detection of nitro-aromatic compounds using dendrimer films also manifests itself as a decrease in the PL output of the sample, it is important to distinguish between the effects of the surroundings and the effects of the explosive vapour, which we want to detect.

To characterise the effect the environment had on the sample, a control experiment was performed. A thin film of bisfluorene was spin-coated onto a fused silica substrate. Absorption and fluorescence scans were then recorded immediately after film deposition. The sample was allowed to stand for one hour in the dark but exposed to the atmosphere, before a second set of absorption and fluorescence measurements were performed. Figure 7.10 below shows the absorption and emission spectra from the control sample before and after the one-hour exposure to air. While there are small changes in the absorption profile, the emission spectra are virtually identical indicating the atmosphere has a negligible effect in causing degradation of the photophysical characteristics of the bisfluorene dendrimer over this timescale.

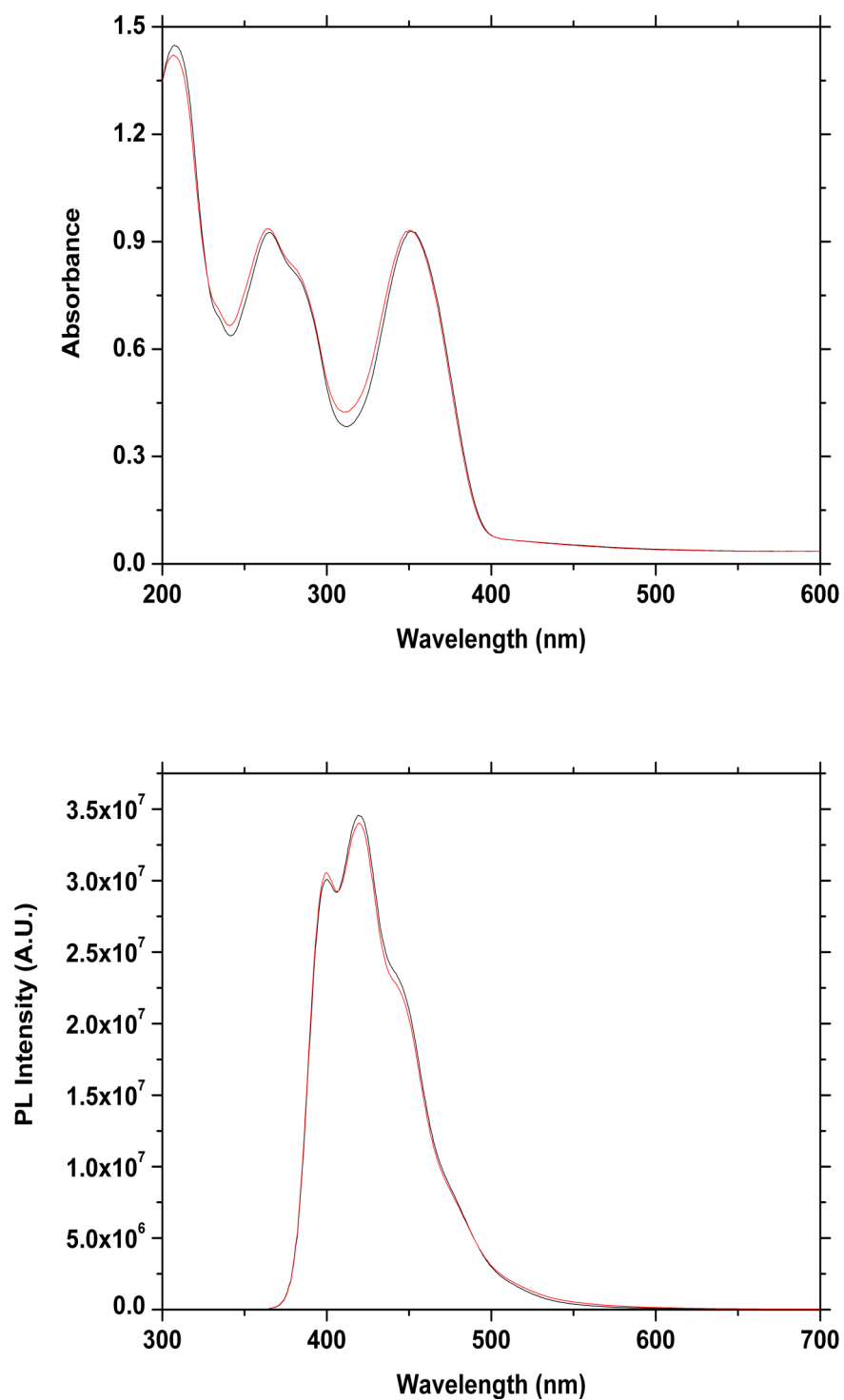


Figure 7.10: Absorption (top) and emission (bottom) spectra for a control sample tested before (black line) and after (red line) a one-hour exposure to atmospheric conditions.

The control experiment was extended to test the lasing response of the dendrimer film, again over a one-hour exposure period. A thin film of bisfluorene was spin-coated onto the corrugated silica substrate of period 260 nm, described earlier in section 7.3.1 (see figure 7.3). The film was transferred for testing immediately after deposition and was pumped using the 337 nm emission of the nitrogen laser using the same set-up as given previously in this chapter. The threshold of the dendrimer laser pumped under these conditions was 155 nJ. After the initial characterisation, the film was left for one hour in ambient conditions before testing again. In figure 7.11 below, the lasing performance of the device before and after the atmospheric exposure is shown.

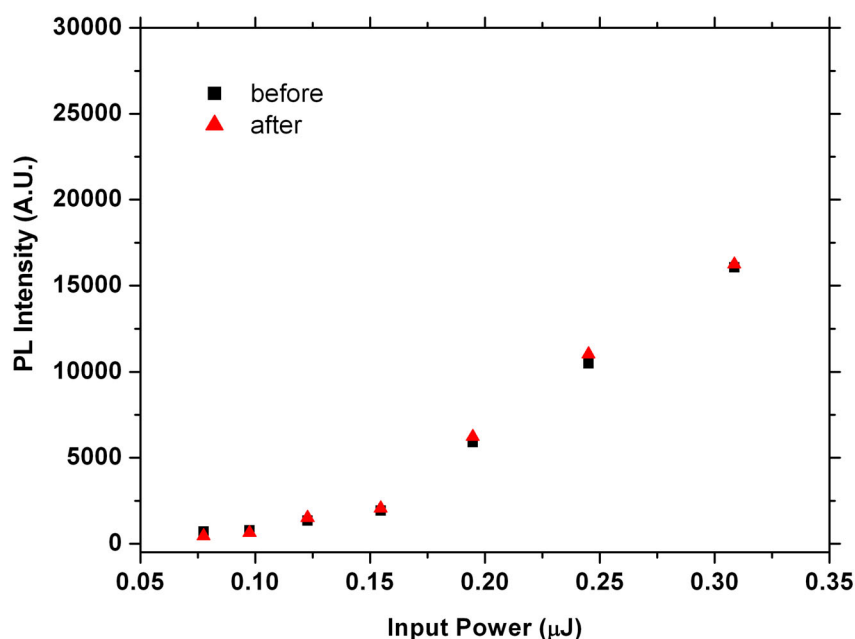


Figure 7.11: Lasing performance of a bisfluorene film on a microstructured silica grating before (black squares) and after (red triangles) a one-hour atmospheric exposure.

The result is that the output for both lasers is almost identical, with the threshold remaining at 155 nJ after one hour in oxygen. The slope efficiency of the device before and after exposure can be seen to remain constant, again demonstrating that over this time period, there is negligible degradation of the sample purely due to the atmosphere. Having performed the control, the experiment was repeated for a bisfluorene dendrimer laser, fabricated in the same way as above and exposed to the vapour from DNB crystals, before being allowed to recover in a nitrogen environment.

The two panels of figure 7.12, pictured below show the absorption (top) and emission (bottom) profiles for a thin film of bisfluorene, which has been spin-coated onto a fused silica substrate. The red line is the initial measurement, taken immediately after fabrication. The black line indicates the performance of the device after a one-hour exposure to the DNB crystals within an enclosed volume (400 cm³). The blue line shows the result of the absorption and fluorescence scans after the device had been allowed 16 hours recovery time while located within a nitrogen glove box. Again, the absorption profile of the device during the various states of testing remain virtually unchanged, emission however is heavily quenched by the DNB binding to the dendrimer surface, reducing the magnitude of the emission to 40% of its initial value across the spectrum. The above results establish that the bisfluorene dendrimer is an effective indicator for the presence of DNB vapour in atmospheric conditions. The blue curve in the lower panel of figure 7.12 shows a near full recovery of the spectrum to its original value highlighting the reversibility of the reaction between the DNB groups and the dendrimer surface. In a suitable experimental set-up this behaviour could be exploited for multiple exposures to DNB vapour, tracking the “on-off” pulses of vapour in real time.

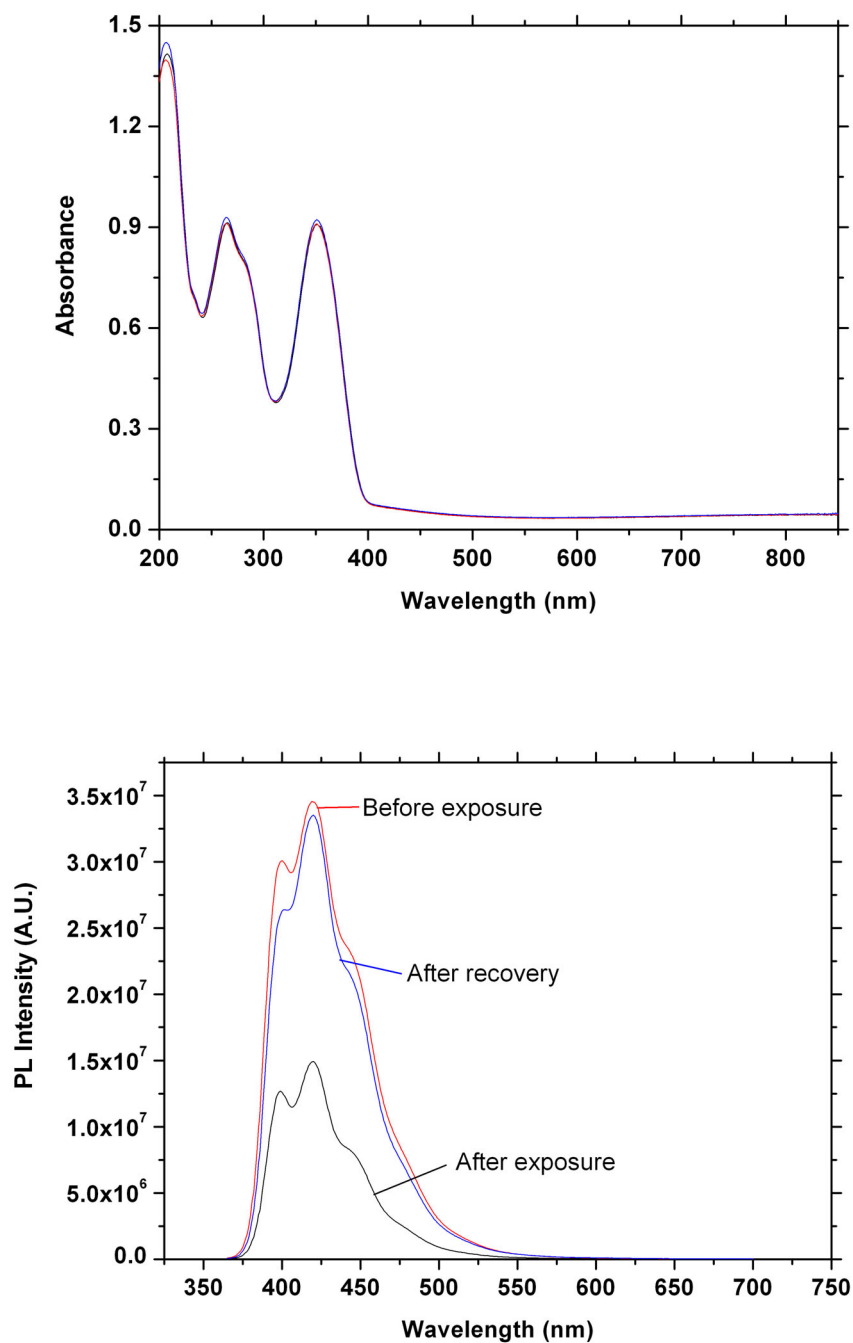


Figure 7.12: Absorption (top panel) and PL emission (bottom panel) for a bisfluorene film on fused silica before (red) and after (black curve) a 1 hour exposure to DNB vapour. The blue curve represents the same device after a 16-hour recovery period in a nitrogen atmosphere.

In order to validate the sensitivity of the detector in the presence of DNB vapour the PL output of a thin film of bisfluorene was compared to the output of the same dendrimer when undergoing laser operation. Figure 7.13 illustrates the performance of the film (25 mg/ml on fused silica substrate) when excited with the output of a nitrogen laser (10 Hz, $\lambda = 337$ nm). The filled squares show the PL output of the device with increasing pump power before the exposure. After exposure, the efficiency of the device drops by 30% (open squares) with output power at 54% of the initial value for a pump intensity of 0.1 μJ (summarised in table 7.4). We find that the relative performance of the device before and after exposure here is very similar to the results from the fluorescence spectra.

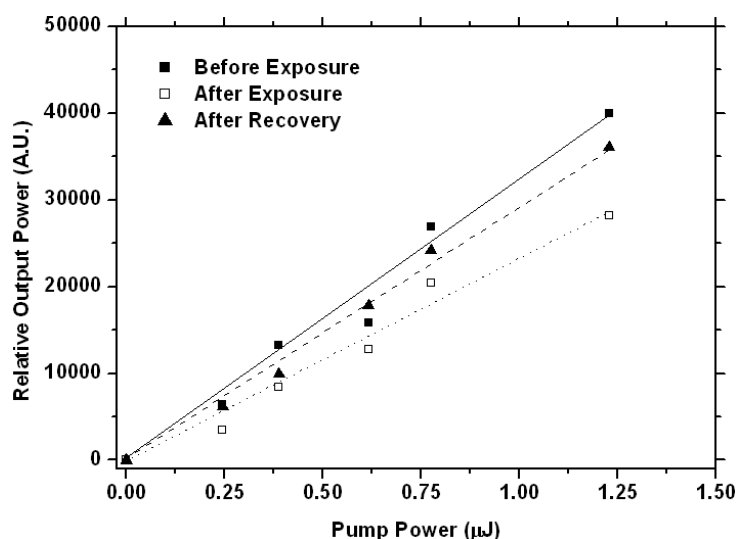


Figure 7.13: PL output of a bisfluorene dendrimer sensor before (filled squares) and after (open squares) DNB exposure. The filled triangles represent the output of the device after recovery in a nitrogen atmosphere.

Secondly, the dendrimer was configured as a surface emitting DFB laser (bisfluorene solution of 25 mg/ml spin-coated onto a pre-corrugated silica substrate, $\Lambda =$

260 nm). Threshold for the sample before exposure was 40 nJ with lasing established at a wavelength of $\lambda = 415$ nm. Data for the sample after exposure and after recovery were normalised with respect to the pre-exposed values, the results of which are shown in table 7.4.

After exposure to the DNB vapour, threshold for the device increased dramatically to 145 nJ with a slope efficiency ~ 50 times less than before the exposure. At a pump intensity of 0.1 μJ , whereas the film undergoing PL output was quenched to 0.54 of the original value, here the laser output after exposure is reduced by a factor of over 300 to 0.003 of the pre-exposed value. This is a 180-fold increase in sensitivity of the device when undergoing laser operation as opposed to PL emission.

The device was allowed to recover for 16 hours in a nitrogen atmosphere before further characterisation. After this period, threshold for the laser was 45 nJ. The slope efficiency and power output (for pump energy of 0.1 μJ) had recovered two orders of magnitude to 27% and 13% of the original values respectively. The results from the above experiment for both the photoluminescence output and the laser emission are summarised below in table 7.4.

The amount of quenching to the photoluminescence for the bisfluorene film is similar to results of Rose *et al.* [50] who reported a twofold reduction in intensity for spontaneous emission upon exposure to dinitrotoluene (DNT). When configured as a DFB resonator, they report a 10-fold increase in sensitivity measuring ASE compared to spontaneous emission, a factor of 30 times lower than the sensitivity reported in this work when detecting DNB vapour, close to laser threshold. Rose *et al.* show a reduction in output intensity $\Delta I/I_0$ of 80% (for laser output before and after exposure to TNT vapour) compared to a reduction of 99.7% for the bisfluorene laser here.

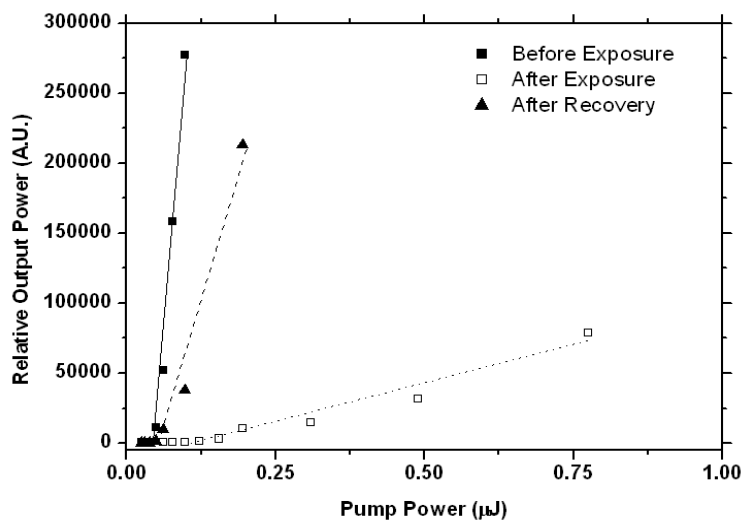


Figure 7.14: Laser efficiency curves for a film of bisfluorene before exposure (filled squares), after exposure (open squares) and after recovery (filled triangles). For a pump energy of $0.1 \mu\text{J}$ / pulse there is a 300 fold increase in sensitivity between the output before and after the DNB exposure.

Sample	PL Measurements		Laser Measurements		
	Relative Slope Efficiency	Normalised Output Power @ $0.1 \mu\text{J}$	Threshold (μJ)	Relative Slope Efficiency	Normalised Output Power @ $0.1 \mu\text{J}$
Before Exposure	1	1	0.04	1	1
After Exposure	0.7	0.54	0.14	0.022	0.003
After Recovery	0.9	0.97	0.045	0.27	0.13

Table 7.4: Results from the PL and laser measurements on the bisfluorene film for various states of exposure to DNB vapour. Values are normalised to the data obtained from the pre-exposed sample.

However, a direct comparison is difficult to quantify due to different resonator geometries being used (ring-mode versus DFB structures) and also due to the different behaviour of the vapour. TNT has a low, easily depleted vapour pressure and due to tight binding to the polymer surface, is inefficient at quenching excitons generated in the film at depths greater than 15 nm.

Also of note is the difference in exposure times between this work and that of Rose *et al.* who typically expose their device to the vapour for 2 minutes and report a 30-fold increase in sensitivity (ASE) afforded by a 1 second exposure. Exposure times in this work were 60 minutes, however there was no pre-saturation of the atmosphere with the explosive vapour before being introduced to the detector. Since this above work was completed, ongoing improvements to the experimental set-up [51] have shown that a bisfluorene film gives a measurable response to DNB (vapour pressure $\sim 10^{-5}$ mbar) within 250 seconds when mixed with a nitrogen stream. The recovery time of the device can also be varied and takes as little as 20 seconds when the sample chamber is vented using a vacuum pump. Recovery of the device when venting with a nitrogen stream is of the order of 300 seconds while a measurable recovery to the output emission occurs in air over a period of several hours. In this latter case however, recovery is incomplete due to degradation of the film in oxygen.

In conclusion, the use of a bisfluorene dendrimer as an explosives detector is extremely promising as demonstrated by the above results. It is expected that further performance gains will be had as exposure conditions continue to be optimised and also with more widespread testing of other novel dendrimer materials.

7.5 Soft lithography of dendrimer materials

The work involving the characterisation of dendrimer lasers contained within this chapter has involved a thin film of the emissive material spin-coated onto a pre-etched substrate. As has been shown elsewhere in this thesis, there are many advantages to the simplified processing afforded by using soft lithography to fabricate the periodic DFB structures required for lasing. In this section, a brief comparison between the quality of gratings imprinted in bisfluorene dendrimer and MEH-PPV films through solvent assisted micromoulding is presented, concluding with a discussion of the results and the potential impact on the fabrication process for DFB lasers using both materials.

7.5.1 Experimental

The thin films were prepared under clean room conditions from solutions of MEH-PPV (5 mg/ml in chlorobenzene) and bisfluorene (25 mg/ml in chloroform) spin-coated onto pre-cleaned silica substrates, which were of the dimensions 12 mm x 12 mm. Pattern transfer was by solvent assisted micromoulding using a co-polymer mould as described in chapter 3. Two moulds were used, one with a period of 400 nm and the other with a period of 266 nm. Processing time for all gratings (unless specified) was 180 seconds. The mould was wetted with one of the following solvents: chlorobenzene, chloroform or tetrahydrofuran (THF), depending on the experiment. Following the transfer of the microstructure, samples were transferred for characterisation which was performed with a Vista scanning probe AFM, supplied by Burleigh.

7.5.2 Results

Dendrimer films were patterned with gratings of two different periods (266 nm and 400 nm) using solvent assisted micromoulding. The same moulds were also used to pattern MEH-PPV polymer films as a comparison. The depth of the grating structure and quality of transfer were noted for each case.

Most of the soft lithography performed throughout this work has been concerned with imprinting MEH-PPV films with a 2-D 400 nm structure to fabricate DFB lasers. These parameters were therefore used as the starting point for a control experiment. In figure 7.15 below, a 400 nm period grating structure has been imprinted into two films of MEH-PPV, which were spin-coated under identical conditions. The top panel is for SAMiM performed using chlorobenzene as the inking solvent (as per previous chapters) and the lower panel is using chloroform. The figure contains a surface map of the topography with relevant cross sections taken for each sample.

The pattern transfer in the MEH-PPV film using chlorobenzene is well defined as expected. A grating depth of ~75 nm was observed, and is a similar value to many of the other deep gratings presented throughout this thesis. Chloroform was also used as the inking solvent for the micromoulding. This was to test the ability of a solvent to facilitate grating transfer when it was not used in the solution preparation (MEH-PPV solutions were prepared with chlorobenzene) and to provide direct comparisons with the lithography results from patterning dendrimer films (which were prepared using chloroform). The quality of the transfer using chloroform was similar to that using chlorobenzene, however the depth of the grating was reduced by around 15 nm (typically ~60 nm deep), this latter point is attributed to two reasons. Chloroform

evaporates more quickly than chlorobenzene at room temperature. This allows less time to bring the sample into contact the mould effectively after inking which will have an impact on the ability to achieve conformal contact. Secondly, it is likely that the polymer flows around the mould structure easier with a chlorobenzene ink due to that solvent being used in the material preparation.

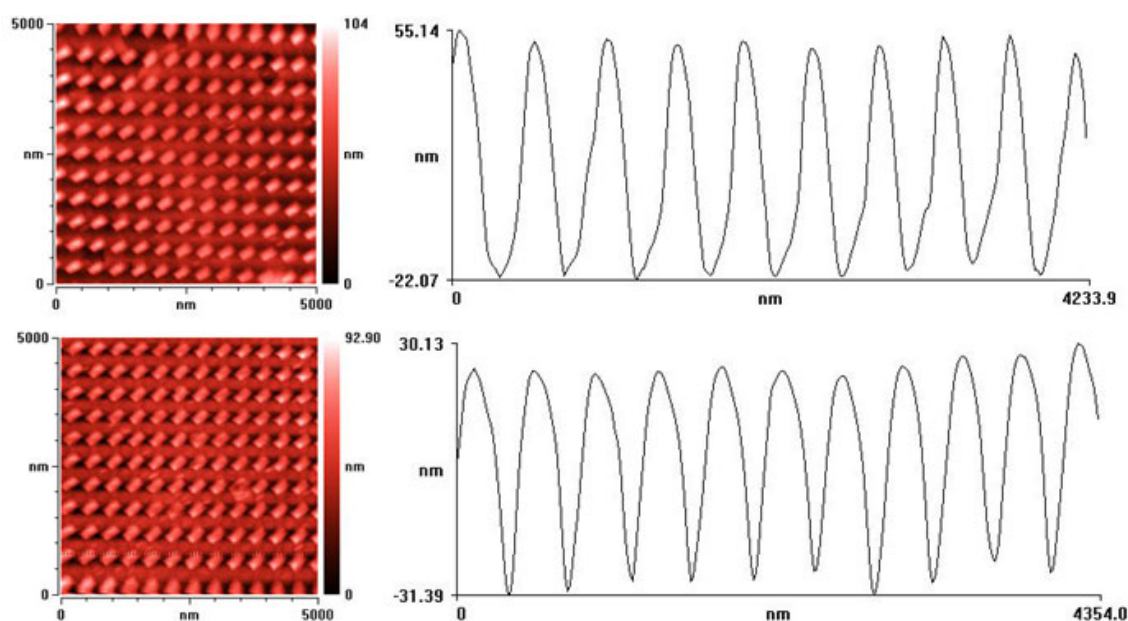


Figure 7.15: MEH-PPV polymer films microstructured with a 400 nm period grating using SAMiM. Grating depth was 75 nm when using a chlorobenzene ink (top). This was reduced to 60 nm when the mould was inked with chloroform (bottom).

For the dendrimer films, a similar case was observed. When the mould was inked with the solvent used in the preparation of the material (in this case chloroform), the grating transfer depth was equal to that observed for the polymer films (70 nm). After switching to chlorobenzene, the transfer depth was reduced more significantly (35 nm) for the dendrimer film than in the polymer case, suggesting that the choice of ink is

more critical to the dendrimer process than for the polymer. AFM surface images with associated cross-section profiles for the microstructured dendrimer films are shown below in figure 7.16. In general, for the 400 nm period grating, the properties of the polymer and dendrimer films after the micromoulding process (when using the preferred solvent for each case) were very similar.

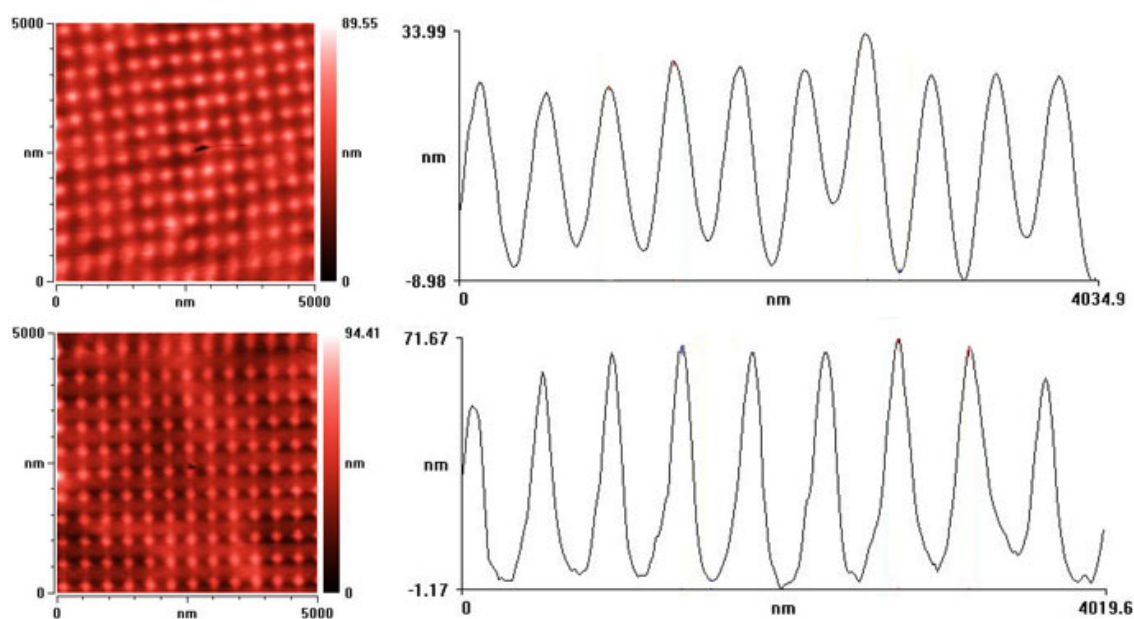


Figure 7.16: Bisfluorene dendrimer films microstructured with a 400 nm period grating using SAMiM. Grating depth was 35 nm when using a chlorobenzene ink (top). The transfer was more successful when the mould was inked with chloroform (bottom), giving a grating depth of 70 nm.

This was not the case when trying to imprint the films with the 266 nm grating however. The top panel of figure 7.17 shows the surface topography and cross-sectional profile for a typical microstructured MEH-PPV film using chlorobenzene as the wetting ink. Despite the reasonable quality of the reproduction, the transferred grating depth is

typically no greater than 15-20 nm. The lower panel shows the same grating period reproduced in a different MEH-PPV film. Of interest here is that the AFM scan shows the domain boundary between a microstructured and unmicrostructured region of film. The boundary forms a 90 nm high cliff-like barrier between the two regions where the polymer appears to have been pulled out of the plane of the film. The exact reason for this is unknown but it is expected that capillary action during the SAMiM process has contributed. The grating depth for this sample is again approximately 15 nm.

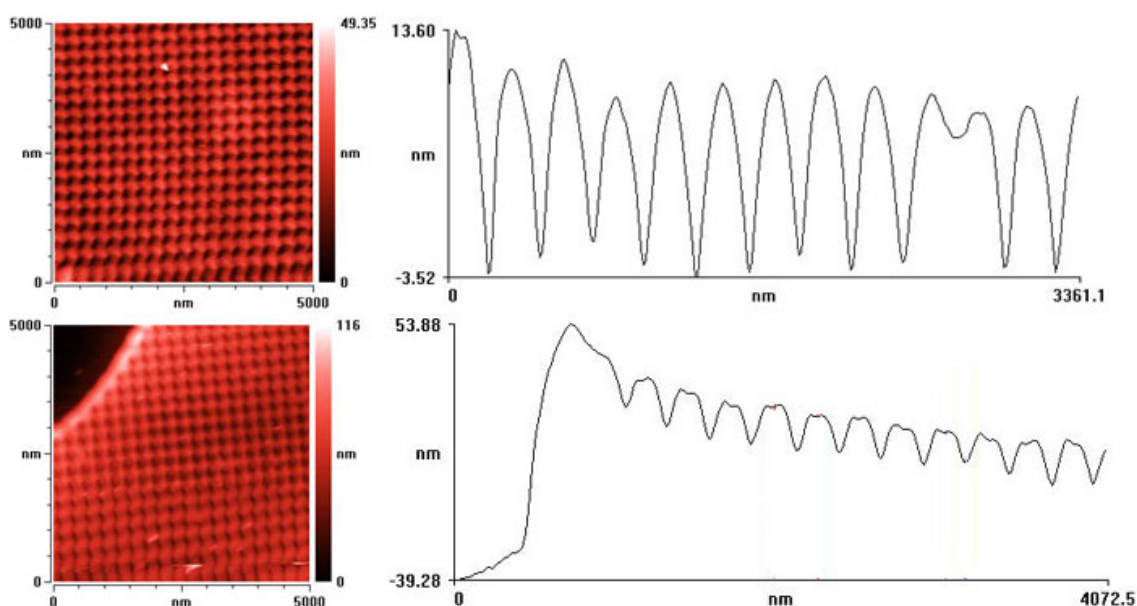


Figure 7.17: MEH-PPV polymer films microstructured with a 266 nm period grating using SAMiM. Grating depth for both samples was ~ 15 nm when using a chlorobenzene ink. The lower panel also shows a boundary in the MEH-PPV film between microstructured and unmicrostructured domains where a swelling of the polymer out of the plane of the film has occurred, possibly a result of capillary action.

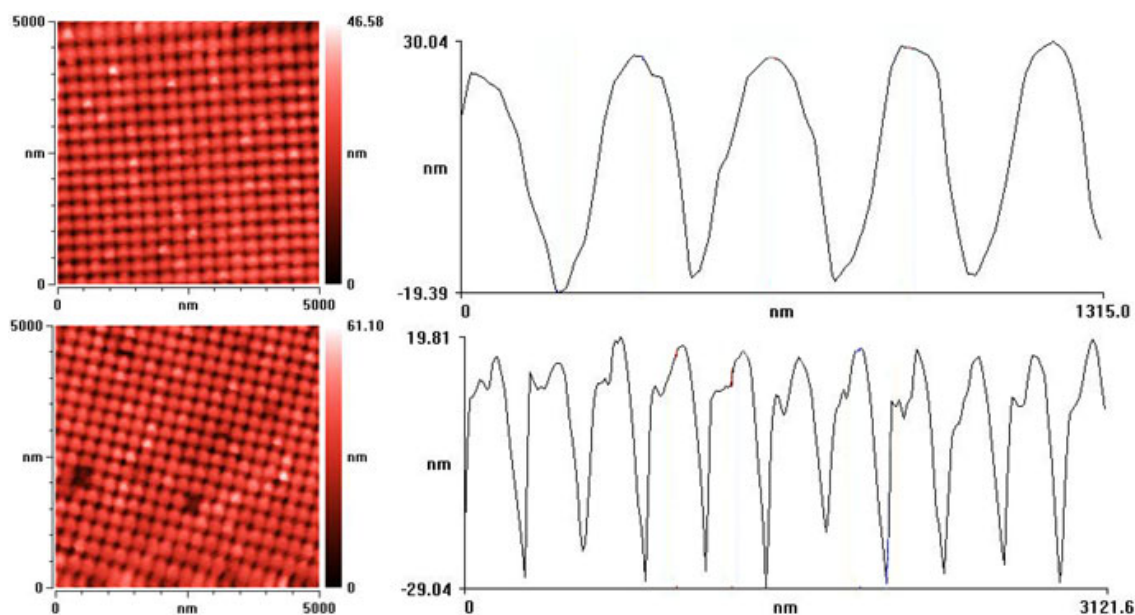


Figure 7.18: Dendrimer films microstructured with a 266 nm period grating using chloroform (top) and THF (bottom) as inking solvents. The transfer of depth is similar in both cases. It can be seen however, that damage has occurred to the shape of the grating when using THF. The likely cause of this is the polarity of the solvent causing swelling in the co-polymer mould.

The dendrimer film showed a marked improvement in the transfer of grating depth for the shorter period grating when compared to the polymer. The top panel of figure 7.18 above shows a 266 nm period grating in a film of bisfluorene using chloroform as the wetting ink. Here, the quality of the transfer is excellent with a grating depth of 50 nm. The reason the dendrimer performs so much better for the shorter grating period than the polymer is most likely due to the small dendritic molecules in the film being more receptive to the shorter grating period than the long, bulky polymer chains in MEH-PPV, allowing the dendrimer film to conform to the grating shape more easily. This work could be extended using even shorter grating

periods to explore any potential limits to the transfer of short-period microstructure to dendrimer films.

The lower panel of figure 7.18 shows a bisfluorene film patterned with a 266 nm grating using THF as a wetting solvent. While the grating depth is approximately the same as for chloroform (50 nm), the cross-section shows an incomplete transfer as mentioned previously in chapter 4 and there is also localised damage to the surface of the grating (which is possibly as expected due to the polar nature of THF, causing swelling to the co-polymer mould [52]). While this again reinforces the need for the correct choice in solvent to perform the micromoulding, of note is the precision (FWHM of the features ~ 133 nm) of which damage to two individual elements of the grating has occurred. This highlights the potential of SAMiM in future work to increase performance from conjugated films by incorporating ever more complex grating patterns and structures in their surface.

In conclusion to this section, by comparing the ability to pattern thin films of MEH-PPV to bisfluorene dendrimer using solvent assisted micromoulding, the small molecular nature of dendrimer material may offer significant advantages over its polymer counterparts as one moves to shorter grating periods.

7.6 Summary

In this chapter, the potential of a variety of novel dendrimer materials as laser materials and a direct application of such devices has been presented. By varying the dendron structure within the dendrimer molecule a range of emission wavelengths could be realised. Further scope for tuning within one specific material (biphenyl dendrons) was demonstrated by subtle changes to the film thickness. The effect of blending the different dendrimers with a CBP host was shown to increase the lasing performance further. This is attributed to reduced concentration quenching by increasing the spacing between the dendrimer cores. By fabricating a DFB laser from the high PLQY BP material (91%), an efficient blue-emitting laser was demonstrated with an efficiency of 8.3% on one side. The low threshold of the device (6 nJ/pulse, equivalent to an excitation density of $4.5 \mu\text{J}/\text{cm}^2$) compares well to devices fabricated using polymers such as PFO.

The potential for dendrimer lasers is further exploited by exploring the sensory ability of the bisfluorene material in detecting trace vapours of DNB. When configured as a DFB laser, there is a 300x factor decrease in the output energy for an excitation energy of $0.1 \mu\text{J}$ / pulse after the sample is exposed to DNB vapour. This is 180 times more sensitive than the equivalent measurements for photoluminescence from this material. The recovery of the material after exposure has been demonstrated. Future work exploring the response speed of the material to explosive vapour could result in the realisation of a portable chemical sensor responding swiftly to the presence of hazardous materials.

Finally, a short comparison between micromoulded bisfluorene and MEH-PPV films was presented. The best grating transfer was found when the solvent used for the material preparation was also used in the SAMiM procedure as the wetting ink. While transfer of grating depth is very similar at longer wavelengths for both materials when using their favoured solvent, depth of transfer is far improved in the dendrimer material as one moves to shorter periods. This is attributed to the small molecular make up of the dendrimer film being more receptive to the moulding process than the bulk chains of the polymer.

7.7 References

- [1] S.V. Frolov, M. Ozaki, W. Gellermann, Z.V. Vardeny and K. Yoshino, *Japanese Journal of Applied Physics Part-2 Letters*, **35**, L1371 (1996).
- [2] G.J. Denton, N. Tessler, M.A. Stevens and R.H. Friend, *Advanced Materials*, **9**, 547 (1997).
- [3] W. Holzer, A. Penzkofer, S.H. Gong, A.P. Davey and W.J. Blau, *Optical and Quantum Electronics*, **29**, 713 (1997).
- [4] R. Gupta, M. Stevenson, A. Dogariu, F.D. McGehee, J.Y. Park, V.I. Srdanov, A.J. Heeger and H. Wang, *Applied Physics Letters*, **73**, 3492 (1998).
- [5] G.A. Turnbull, P. Andrew, W.L. Barnes and I.D.W. Samuel, *Physical Review B*, **67**, (2003).
- [6] J. Burroughes, D.D.C. Bradley, A. Brown, R. Marks, K. Mackay, R.H. Friend, P.L. Burn and A. Holmes, *Nature*, **347**, 539 (1990).
- [7] T. Zyung, D. Hwang, I. Kang, H. Schim, W. Hwang and J. Kim, *Chemical Materials*, **7**, 1499 (1995).
- [8] R.H. Partridge, *Polymer*, **24**, 6 (1983).
- [9] J. Kido, K. Hongawa, K. Okuyama and K. Nagai, *Applied Physics Letters*, **63**, 19 (1993).
- [10] G. Grem, G. Leditzky and B. Ullrich, *Synthetic Metals*, **51**, 1 (1992).
- [11] G. Grem, G. Leditzky, B. Ullrich and G. Leising, *Advanced Materials*, **4**, 36 (1993).
- [12] J. Kido, K. Hongawa, K. Okuyama and K. Nagai, *Applied Physics Letters*, **64**, 815 (1994).

- [13] J. Kido, H. Shionoya and K. Nagai, *Applied Physics Letters*, **67**, 2281 (1995).
- [14] Y. Yang, Q. Pei and A.J. Heeger, *Journal of Applied Physics*, **79**, 934 (1996).
- [15] M.D. McGehee, T. Bergstedt, C. Zhang, A.P. Saab, M.B. O'Regan, G.C. Bazan, V.I. Srdanov and A.J. Heeger, *Advanced Materials*, **11**, 1349 (1999).
- [16] M. Fukada, K. Sawaka and K. Yoshino, *Japanese Journal of Applied Physics*, **28**, 1433 (1989).
- [17] M.N. Shkunov, R. Osterbacka, A. Fujii, K. Yoshino and Z.V. Vardeny, *Applied Physics Letters*, **74**, 1648 (1999).
- [18] M. Theander, T. Granlund, D.M. Johanson, A. Ruseckas, V. Sundstrom, M.R. Andersson and O. Inganäs, *Advanced Materials*, **13**, 323 (2001).
- [19] R.D. Xia, G. Heliotis and D.D.C. Bradley, *Applied Physics Letters*, **82**, 3599 (2003).
- [20] G. Heliotis, D.D.C. Bradley, G.A. Turnbull and I.D.W. Samuel, *Applied Physics Letters*, **81**, 415 (2002).
- [21] G. Heliotis, R.D. Xia, D.D.C. Bradley, G.A. Turnbull, I.D.W. Samuel, P. Andrew and W.L. Barnes, *Applied Physics Letters*, **83**, 2118 (2003).
- [22] M. Grell, D.D.C. Bradley, X. Long, T. Chamberlain, M. Inbasekaran, E.P. Woo and M. Soliman, *Acta Polym.*, **49**, 439 (1998).
- [23] S. Setayesh, A.C. Grimsdale, T. Weil, V. Enkelmann, K. Müllen, F. Meghdadi, E.J.W. List and G. Leising, *Journal of the American Chemical Society*, **123**(5), 946 (2001).
- [24] S.C. Lo, N.A.H. Male, J.P.J. Markham, S.W. Magennis, P.L. Burn, O.V. Salata and I.D.W. Samuel, *Advanced Materials*, **14**, 975 (2002).

- [25] J.P.J. Markham, S.C. Lo, S.W. Magennis, P.L. Burn and I.D.W. Samuel, *Applied Physics Letters*, **80**, 2645 (2002).
- [26] P.L. Burn, S.C. Lo and I.D.W. Samuel, *Advanced Materials*. In press.
- [27] T-Q. Nguyen, R.C. Kwong, M.E. Thompson and B.J. Schwartz, *Applied Physics Letters*, **76**, 2454 (2000).
- [28] M. Halim, J.N.G. Pillow, I.D.W. Samuel and P.L. Burn, *Advanced Materials*, **11**, 371 (1999).
- [29] M. Halim, J.N.G. Pillow, I.D.W. Samuel and P.L. Burn, *Synthetic Metals*, **102**, 922 (1999).
- [30] M. Halim, I.D.W. Samuel, J.N.G. Pillow and P.L. Burn, *Synthetic Metals*, **102**, 1113 (1999).
- [31] M.D. McGehee and A.J. Heeger, *Advanced Materials*, **12**, 1655 (2000)
- [32] J.R. Lawrence, G.A. Turnbull and I.D.W. Samuel, *Applied Physics Letters*, **80**, 3036 (2002).
- [33] I.D.W. Samuel and G.A. Turnbull, *Chemical Review*, **107**, 1272 (2007).
- [34] J.R. Lawrence, G.A. Turnbull, I.D.W. Samuel, G.J. Richards and P.L. Burn, *Optics Letters*, **29**, 869 (2004).
- [35] J.R. Lawrence, E.B. Namdas, I.D.W. Samuel, G.J. Richards and P.L. Burn, *Advanced Materials*. In press.
- [36] J.C. Ribierre, G. Tsiminis, S. Richardson, G.A. Turnbull, I.D.W. Samuel, H. Barcena and P.L. Burn, *Applied Physics Letters*. In press.
- [37] O. Varnavski, I.D.W. Samuel, L.-O. Palsson, R. Beavington, P.L. Burn and T. Goodson, *Journal of Chemical Physics*, **116**, 8892 (2002).

- [38] A. Otomo, S. Yokoyama, T. Nakahama and S. Mashiko, *Applied Physics Letters*, **77**, 3881 (2000).
- [39] G. Heliotis, R. Xia, G.A. Turnbull, P. Andrew, W.L. Barnes, I.D.W. Samuel and D.D.C. Bradley, *Advanced Fucntional Materials*, **14**, 91 (2004).
- [40] J.C. Ribierre, A. Ruseckas, I.D.W. Samuel, H. Barcena, P.L. Burn. In preparation.
- [41] D.T. McQuade, A.E. Pullen and T.M. Swager, *Chemical Reviews*, **100**, 2537 (2000).
- [42] J.J. Miasik, A. Hooper and B.C. Tofield, *J.Chem. Soc., Faraday Trans. I.*, **82**, 1117 (1986).
- [43] G.P. Kittlesen, H.S. White and M.S. Wrighton, *Journal of the American Chemical Society*, **106**, 7389 (1984).
- [44] E.W. Paul. A.J. Ricco and M.S. Wrighton, *Journal of Physical Chemistry*, **89**, 1441 (1985).
- [45] J.J. Andre, M. Bernard, B. Francois and C. Mathis, *Phys.*, **44** (1983).
- [46] J. Janata and M. Josowicz, *Acc. Chem. Res.*, **31**, 241 (1988).
- [47] J.-S. Yang and T.M. Swager, *Journal of the American Chemical Society*, **120**, 5321 (1998).
- [48] J.-S. Yang and T.M. Swager, *Journal of the American Chemical Society*, **120**, 11864 (1998).
- [49] C.J. Cumming, C. Aker, M. Fisher, M. Fox, M.J. la Grone, D. Reust, M.G. Rockley, T.M. Swager, E. Towers and V. Williams, *IEEE Transactions on Geoscience and Remote Sensing*, **39**, 1119 (2001).

- [50] A. Rose, Z. Zhu, C.F. Madigan, T.M. Swager and V. Bulovic, *Nature*, **434**, 876 (2005).
- [51] Ying Yang, Private Communication.
- [52] H. Schmid and B. Michel, *Macromolecules*, **33**, 3042, (2000).

Chapter 8: Conclusions

In the thirty years that have passed since conjugated semiconducting polymers were unleashed unto the world, we have witnessed the rapid development of an incredibly diverse and vibrant field of physics research. This is no doubt due to myriad applications that these fascinating materials have lent themselves. The simple fabrication of devices from solution allows them to be cheap and disposable. Couple this with the equally simple fabrication of wavelength-scale microstructure which can be incorporated into a polymeric device and we have a winning formula for the development of innovative laser sources.

The contributions contained in this thesis have concerned themselves with the amplification and lasing properties of conjugated polymer and dendrimer materials. This work seeks to address and provide insight into improving the techniques required for developing efficient devices that can also find practical uses out of the lab in the real world, while maintaining the simplicity of fabrication.

Soft lithography was used to apply wavelength scale microstructure to films of the conjugated polymer MEH-PPV creating distributed feedback lasers. The effect of the applied grating depth on the lasing characteristics was explored and found to be in good agreement with the values predicted from theory. The excellent transfer of deep gratings to the polymer films resulted in the demonstration of a low threshold polymer laser with comparable threshold and efficiency values to previous reports using silica gratings but with a much simpler fabrication process. Micromoulding was also used to apply novel

grating patterns to conventional and flexible substrates, the latter being highly promising for wide-scale production through technology such as applying thin films and coatings with ink-jet printing.

In chapter 5, the theme of developing practical polymer laser devices continued with the demonstration of vastly improved polymer laser operating lifetimes by using a simple encapsulation process. By protecting the emissive layer from hostile elements such as oxygen and water, an encapsulated polymer laser operates for over 2500 times longer than a non-encapsulated device running under the same conditions. The demonstration of continued laser operation more than a year after fabrication highlights the great potential for realising polymer lasers with a lifetime of thousands of hours. Through absorption measurements and spectroscopic ellipsometry, the understanding of photodegradation in the device emission during the laser operation is addressed, a field where comparatively little reported quantitative data exists.

Amplification and gain were explored with the demonstration of a solution based polymer amplifier using the polymer F8BT. Despite the strong interest in the realisation of such devices, prior to this work, there had only been a single demonstration of such an optical amplifier. Semiconducting polymers are known for showing high optical gain throughout the visible range and are relatively free from concentration quenching that affects the performance of organic dyes. The amplifier demonstrated optical gain (≤ 40 dB) across a wavelength range of almost 50 nm. The overlap of the gain in F8BT and the main transmission window of polymer optical fibre suggest likely applications for conjugated polymers in this area.

While being known for showing high gain over very short distances, a number of processes seek to deplete the population of the excited state in conjugated polymers when pumping at high intensities. By considering one of these processes in a model, the rate of exciton-exciton annihilation was calculated in thin films of MEH-PPV by measuring the effect on the absorption saturation for intense optical pumping.

Finally, novel branched dendrimers were configured as DFB lasers. These incredible materials possess modular architecture allowing independent tuning of the electronic properties such as the colour along with variations in the surface groups, which affect solubility. By carefully selecting the dendron or linking group, a highly efficient blue-emitting laser (8.3% on one side) was demonstrated – comparable to a blue-emitting DFB laser using PFO which had an efficiency of 7.8% (measured on both sides). In simply varying the film thickness, the emission wavelength was tuned through 20 nm. By taking one of these efficient lasers and exposing the film to a nitrobenzene derivative, chemosensing of explosive vapour was realised. The ability of the dendrimer to recover after an exposure, reversing the luminescence quenching by the nitro groups coupled with the incredible sensitivity of the device when operating close to threshold makes the dendrimer laser a realistic possibility for future sensory applications such as land-mine detection. The dendrimer work presented was rounded off by comparing films, microstructured with solvent assisted micromoulding to the gratings transferred to polymer films for different grating periods. The dendrimer films perform excellently when transferring shorter (266 nm) grating periods while the polymers films show poor transfer of grating depth. It is likely that the small molecule nature of the dendrimer

materials makes them more versatile than polymers when applying the micromoulding technique, a feature that could possibly be exploited in the future when transferring small feature sizes and increasingly complex patterns.

Research into conjugated polymers and dendrimers has now gathered a lot of momentum. The understanding of these unique materials continues to move forward at a staggering pace as each new discovery unlocks the doors between exploring the fundamental chemistry of the molecules and developing the applications of tomorrow that can surely only improve our quality of life.

Appendix A: Publications arising from this thesis

S. Richardson, O.P.G. Gaudin, G.A. Turnbull and I.D.W. Samuel, *Improved Operational Lifetime of Semiconducting Polymer Lasers through Encapsulation*. Submitted to Applied Physics Letters.

S. Richardson, Y. Yang, H. Barcena, P.L. Burn, G.A. Turnbull and I.D.W. Samuel, *Chemosensing of DiNitroBenzene using Dendrimer Distributed Feedback Lasers*. In preparation.

S. Richardson, G.A. Turnbull and I.D.W. Samuel, *Absorption Saturation in Thin Films of MEH-PPV*. In preparation.

S. Richardson, G.A. Turnbull and I.D.W. Samuel, *Effect of Grating Depth on Lasing Characteristics in Semiconducting Polymer Distributed Feedback Lasers*. In preparation.

G. Heliotis, D.D.C. Bradley, M. Goossens, S. Richardson, G.A. Turnbull and I.D.W. Samuel, *Operating Characteristics of a Travelling-wave Semiconducting Polymer Optical Amplifier*, *Applied Physics Letters*, **85**, 6122 (2004).

J-C. Ribierre, G. Tsiminis, S. Richardson, G.A. Turnbull, I.D.W. Samuel, H.S. Barcena and P.L. Burn. *Amplified Spontaneous Emission and Lasing Properties of Bisfluorene-Cored Dendrimers*. *Applied Physics Letters*, **91**, 081108 (2007).

